2D Conjugated Polymer Thin Films for Organic Electronics: Opportunities and Challenges

Guang-en Fu, Haoyong Yang, Wenkai Zhao, Paolo Samorì, Tao Zhang

Two-Dimensional Conjugated Polymer Thin Films for Organic Electronics: Opportunities and Challenges

Guang-en Fu[†]*, Haoyong Yang*[†]*, Wenkai Zhao*[†]*, Paolo Samorì, and Tao Zhang*[*]

Dedicated to the special issue for the 20th Anniversary of the Ningbo Institute of Materials Technology and Engineering.

G. Fu, H. Yang, W. Zhao, Prof. Dr. T. Zhang
Key Laboratory of Marine Materials and Related Technologies, Ningbo Institute of Materials Technology and Engineering, Chinese Academy of Sciences, Ningbo 315201, China
E-mail: tzhang@nimte.ac.cn
Prof. Dr. P. Samorì
University of Strasbourg, CNRS, ISIS UMR 7006, 8 Allée Gaspard Monge, 67000 Strasbourg, France
[†] These authors contributed equally to this work.

Two-dimensional conjugated polymers (2DCPs) possess extended in-plane π-conjugated lattice and out-of-plane π-π stacking, which results in enhanced electronic performance and potentially unique band structures. These properties, along with pre-designability, well-defined channels, easy post-modification, and order structure attract extensive attention from material science to organic electronics. In this review, we summarize the recent advance in the interfacial synthesis and conductivity tuning strategies of 2DCP thin films, as well as their application in organic electronics. Furthermore, we show that, by combining topology structure design and targeted conductivity adjustment, researchers have fabricated 2DCP thin films with pre-designed active groups, highly ordered structures and enhanced conductivity. These films exhibit great potential for various thin-film organic electronics, such as organic transistors, memristors, electrochromism, chemiresistors, and photodetectors. Finally, we discuss the future research directions and perspectives of 2DCPs in terms of the interfacial synthetic design and structure engineering for the fabrication of fully conjugated 2DCP thin films, as well as the functional manipulation of conductivity to advance their applications in future organic electronics.

Keywords: two-dimensional materials; two-dimensional polymers; conjugated polymers, interface polymerizations, organic electronics

1. Introduction

Linear one-dimensional π-conjugated polymers (1DCPs)[1,2] including polyacetylene[3,4], polypyrrole[5,6], polythiophene[7–9], and polyaniline[10–12] arouse widespread attention as semiconductor materials[13] in organic electronic devices such as organic transistors[14,15], electrochromism[16,17], chemical sensors[18,19] and photodetectors[20,21] due to their intrinsic optical and electronic activities, flexibility, and versatile doping/dedoping chemistry[22]. Although the extended π electron delocalization along the 1D polymer chain enables efficient charge conduction[23], the inter-chain charge transfer limits the further improvement of conductivity due to inefficient hopping (**Figure 1**).[24–26] Therefore, extending the dimensionality to two-dimensional conjugated polymers (2DCPs) is a feasible and charming route to address the above-mentioned issues, which can construct multiple charge transport pathways by bypassing defective sites, suppressing vibrational freedom degrees, and enhancing delocalized conjugation[27].

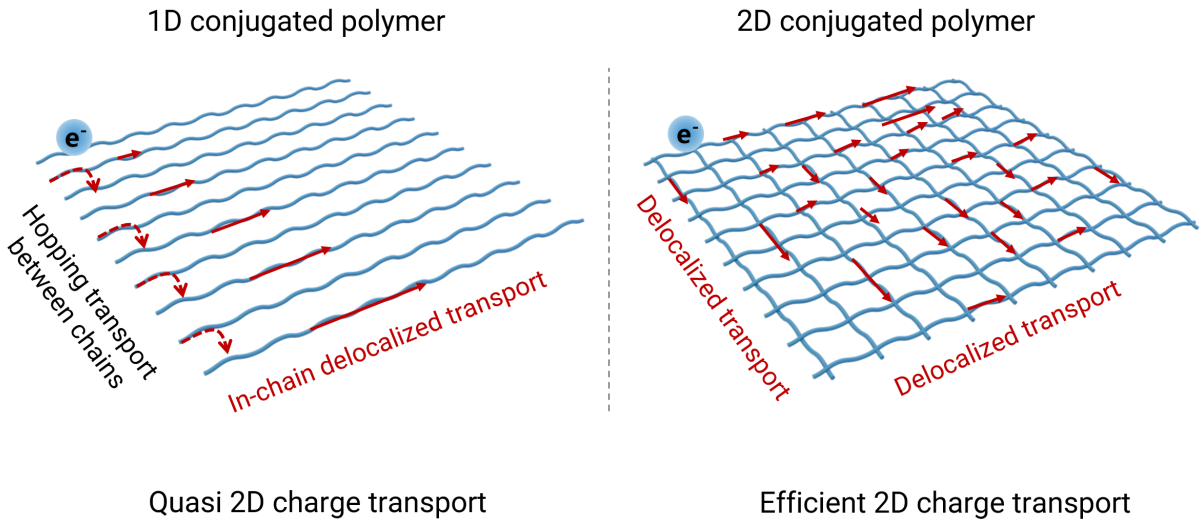

Figure 1. Schematic representation of comparison of charge transport within 1D and 2D conjugated polymers.

2DCPs as an emerging class of π-conjugated polymer thin films/nanosheets, usually include 2D covalent organic frameworks (2D COFs)[28] and 2D metal-organic frameworks (2D MOFs)[29], etc. This review mainly focuses on 2D COFs (**Figure 2a**), which share extended in-plane π-conjugated lattice formed *via* 2D covalent polymerization and out-of-plane π-π stacking, resulting in enhanced electronic performance and potentially unique band structures (such as Dirac cones)[30,31]. Especially in terms of organic electronics, numerous unique and charming advantages of 2DCPs make them stand out and spark considerable interest. Firstly, the pre-

designability of the 2DCPs endows the capability to exploit a variety of building units to achieve target architectures for desirable and tunable functionalities.[28,32] For example, the introduction of redox functional groups or building blocks that can generate free radicals is beneficial to improving conductivity or achieving electrochromism functionality[33]. Moreover, the permanent 1D pores with high surface area provide a high density of active sites and motivate mass transport. The densely arranged π columns act as a pre-organized route to promote the transport of charge carriers and extend the life of excited states, potentially leading to significant optical, electrical, and optoelectronic properties.[34] Furthermore, 2DCPs are composed of robust covalent bonds that enable excellent thermal and chemical stability to cope with various circumstances for broadening the applicable fields.

In recent years, tremendous efforts have been engaged in the design and synthesis of 2DCP thin films for high-performance organic electronics.[35–39] Following the topological concept of reticular chemistry, the multifunctional monomers (*i.e.*, build blocks) are abstracted into corresponding shapes and nodes, enabling the design of channels with different pore sizes and shapes (such as tetragonal, hexagonal, rhombus, and triangle) (**Figure 2b**).[28] The building blocks are linked by dynamic covalent chemistry bonds, *via* thermodynamically controlled reversible reaction, to enable continuous error correction during the synthesis process to form long-range ordered crystal skeletons (**Figure 2a**).[32,40] So far, 2DCPs with versatile linkages have been developed, including imine, pyrazine, azine, vinylene, *etc.* (**Figure 2c**).[28,41,42] Through rationalized structural design and multiple modifications, 2DCPs have achieved great progress and breakthroughs in the field of organic thin film electronics,[34,43,44] which reveals the necessity of a comprehensive review on this rapidly rising filed.

In this review, we present the recent advances in the interfacial synthesis and conductivity tuning strategies of 2DCP thin films, as well as their applications in organic electronics. Firstly, we introduce the interfacial synthesis strategies of 2DCP thin films, highlighting the fabrication of large-area 2DCP thin films with highly-ordered molecular structures (**Figure 2d**). Continuously, we discuss the unique advantage and conducting mechanism of 2DCPs, including the transport route of carriers and the effect of topology structure on the conductivity. We then present conductivity tuning strategies for 2DCPs to improve the conductivity, such as chemical doping, interlayer connection and heterostructure engineering. In addition, we summarize the applications of the 2DCPs in various organic electronics, including organic transistors, memristors, electrochromism, chemiresistors, and photodetectors (**Figure 2e**). Finally, we discuss the challenges and perspectives for 2DCPs in terms of synthetic approaches

and structural design for full conjugated 2DCP thin films, as well as the functional manipulation to advance their applications in organic electronics.

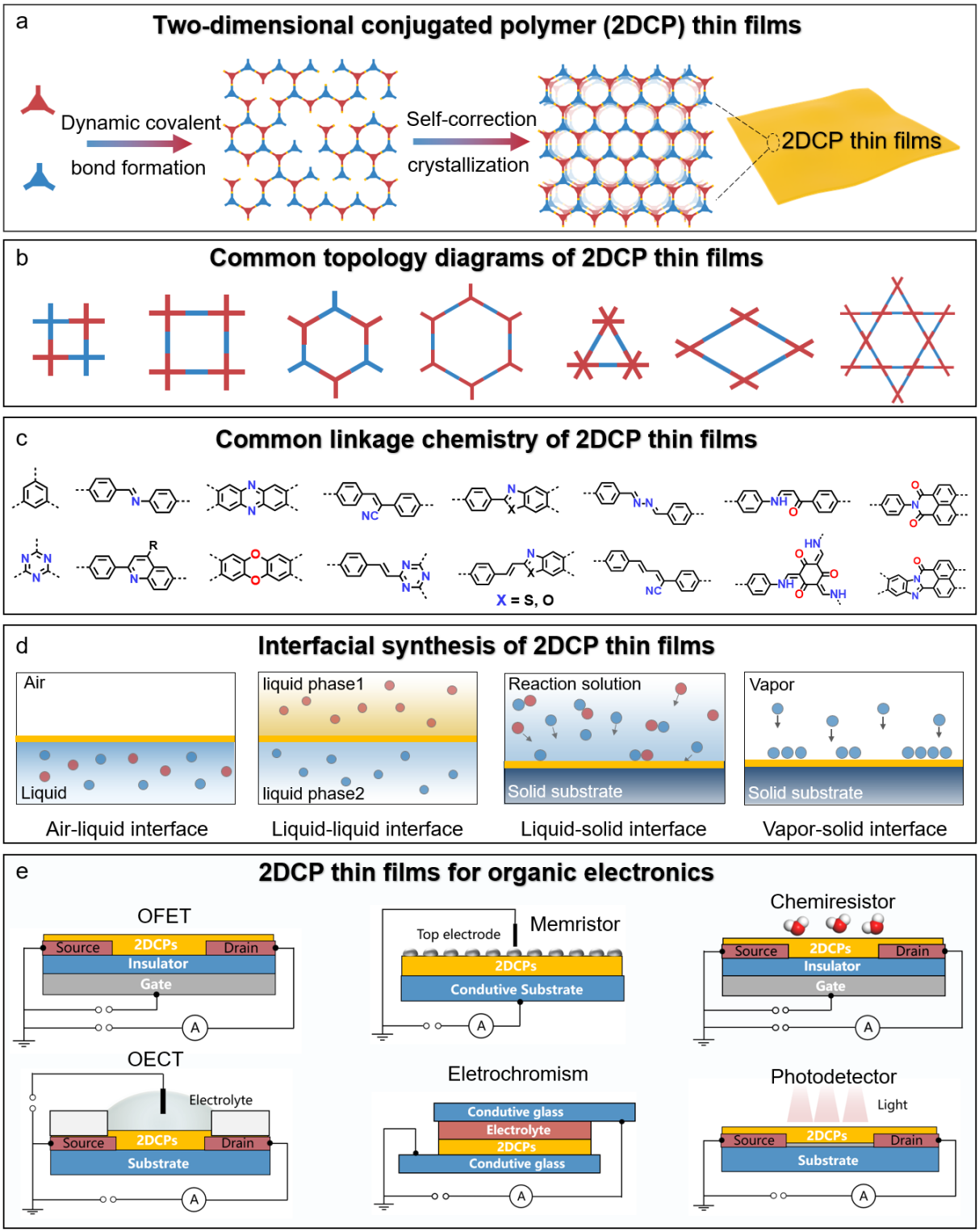

Figure 2. Schematic representation of a) dynamic covalent chemical bonding process, b) common topologies, c) common linkage chemistry, d) interfacial synthesis strategies and e) organic electronic applications of 2DCP thin films.

2. Synthesis Strategies of 2DCP Thin Films

2.1. Solid-liquid Interface Polymerization

The preparation techniques of 2DCP thin films are generally classified into top-down and bottom-up strategies.[45] The top-down strategies mainly exfoliate bulk crystals or powders into nanosheets through ultrasonic, mechanical, chemical exfoliation, etc.[46–48] However, exfoliation methods yield 2DCPs with limited lateral dimensions, typically ranging from nanometers to micrometers, ultimately determined by the crystal size.[49] Moreover, the resulting nanosheets often exhibit numerous structural and electronic defects, which hinder the transfer of charge carriers. Conversely, the bottom-up is an effective strategy for constructing well-ordered 2DCP thin films due to its merits in the regulation of the domain sizes and defects.[45] In particular, the interface polymerization method of the bottom-up strategies can enable the generated 2DCP thin films to be easily transferred. Direct growth of 2DCP thin films onto various substrates *via* liquid-solid interface polymerization can simplify the film transfer process, which is the preferred method for organic electronic device fabrication (**Figure 3a**).

In the liquid-solid interface polymerization, the modification of the substrate surface, *e.g.,* by grafting functional groups, can improve substrate compatibility and expand the types of polymerization reactions. Our group[50] reported a self-assembly monolayer-assisted surface-initiated Schiff-base-mediated aldol polycondensations (SI-SBMAP) to prepare sp^2c-COF films on arbitrary substrates (*e.g.,* fluorine-doped tin oxide, aluminum sheet, polyacrylonitrile membrane) of various shapes (*e.g.,* plane, sphere, ingot). In the SI-SBMAP, the -NH_2 in self-assembly monolayers (SAMs) on substrate surfaces can react with aldehydes (-CHO) by Schiff-base reaction to form an aldehyde-terminated monolayer, which allows further initiation of the aldol polycondensation to prepare sp^2c-COF films (**Figure 3b**). The resulting films exhibit large areas of up to 120 cm^2 and adjustable thicknesses ranging from tens of nanometers to a few micrometers. This strategy also shows great potential for preparing 2DCP thin films with other linkages.

During the interface reaction process, the crystallization reactions between different interfaces affect each other, and one crystallization process can be applied to enhance the other to synthesize thin films at the interface. Rahul Banerjee's group[51] proposed the “competing growth mechanism” coupled the liquid-liquid and solid-liquid interfacial crystallization to prepare 2DCP thin films on different substrates (**Figure 3c**). During the competing growth process, most of the crystallization occurs at the liquid-liquid interface while only the residue crystallizes at the solid-liquid interface called “residual crystallization (RC)”. The 2DCP thin films synthesized on substrates *via* the RC process share smooth surfaces with a 5-12 nm

average roughness. The film thickness on substrates is determined by the rate of liquid-liquid interfacial crystallization and ranges from 1.8 to 145 nm.

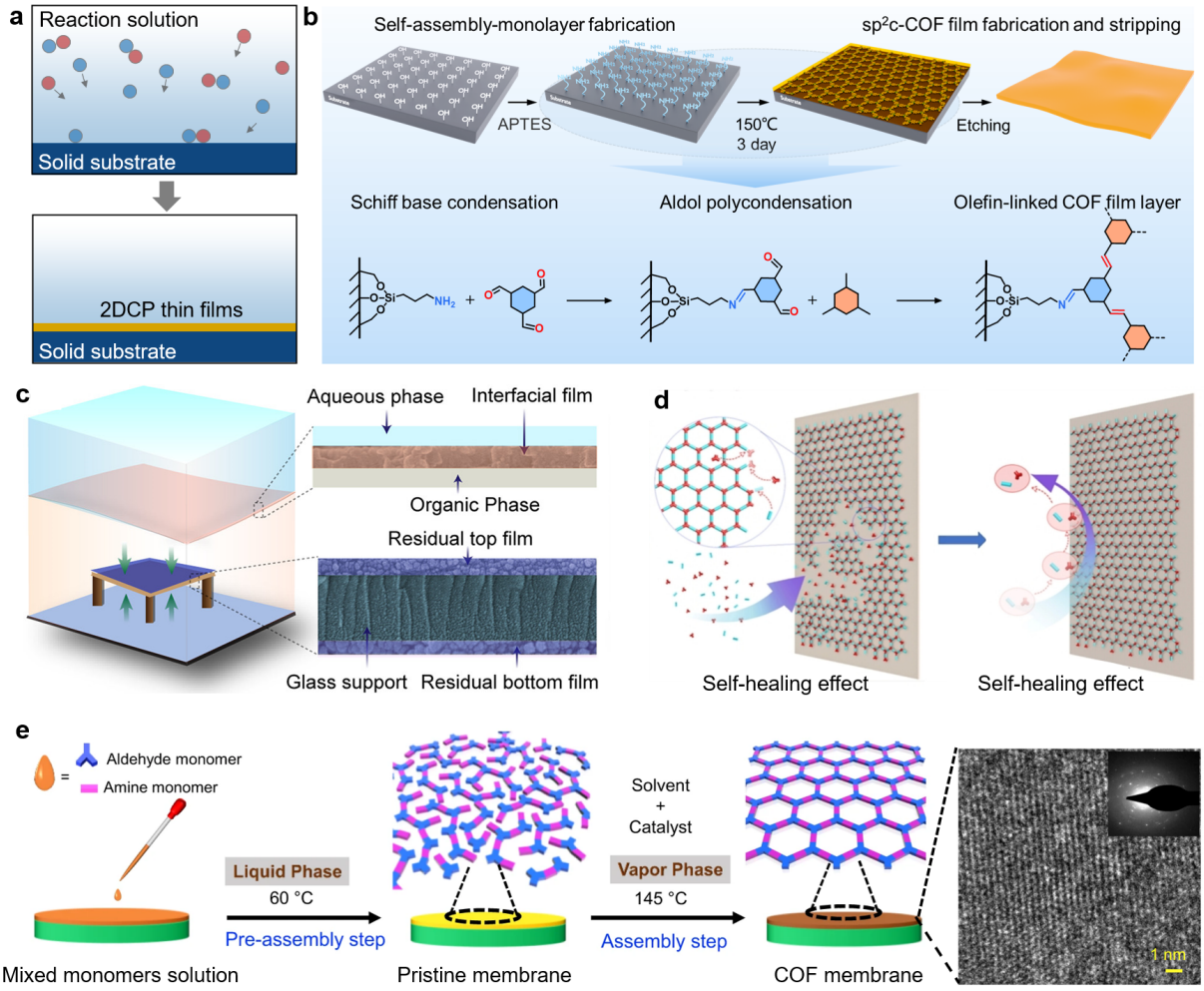

Figure 3. a) Schematic diagram of solid-liquid interface polymerization. b) Synthesis strategy of SI-SBMAP to synthesize continuous and independent sp^{2}c-COF films.[50] Copyright 2023, American Chemical Society. c) Schematic illustration of 2DCP thin films synthesized at liquid-liquid and solid-liquid interfaces *via* interfacial and residual crystallization. The zoomed-in images represent the interfacial and residual (top and bottom surface of the substrate) 2DCP thin films.[51] Copyright 2021, American Chemical Society. d) Illustration of the self-healing effect and the self-inhibiting effect.[52] Copyright 2023, Wiley-VCH. e) Schematic diagram of phase-switching strategy to synthesize 2DCP thin films. The mixed monomer solution was initially cast onto the substrate to fabricate pristine films during the pre-assembly step and further heated to obtain 2DCP thin films in the assembly step. Inset: the high-resolution transmission electron microscopy (HR-TEM) images and selected area electron diffraction (SAED) patterns of the synthesized film.[53] Copyright 2022, Nature Publishing Group.

The electrochemical solid-liquid interface polymerization is a facile and efficient strategy to prepare ultrathin 2DCP thin films, which share two intrinsic merits including the self-healing effect for macroscopic defect-free structure and the self-inhibiting effect for ultrathin morphology (**Figure 3d**).[52] Firstly, the uncovered areas exhibit a higher current density during the electrochemical process, where preferential polymerization of monomers forms films, which allows films with self-healing ability and macroscopic defect-free structure. Moreover, the deposited insulating films diminish the current density to suppress the electrochemical deprotonation process, which affords the self-inhibiting effect to obtain ultrathin morphology. The film thickness and defects can be precisely modulated by electrochemical time and voltage based on the self-healing effect and self-inhibiting effect. In addition, electrons are concentrated on the cathode, and deprotonation reactions are performed on the confined solid-liquid interface, which provides favorable kinetics and thermodynamics for interfacial polymerization. Zhongyi Jiang's group[52] applied this electrochemical interface polymerization strategy to successfully fabricate a class of imine-linked 2DCP thin films with similar reaction mechanisms, which further confirm its general applicability.

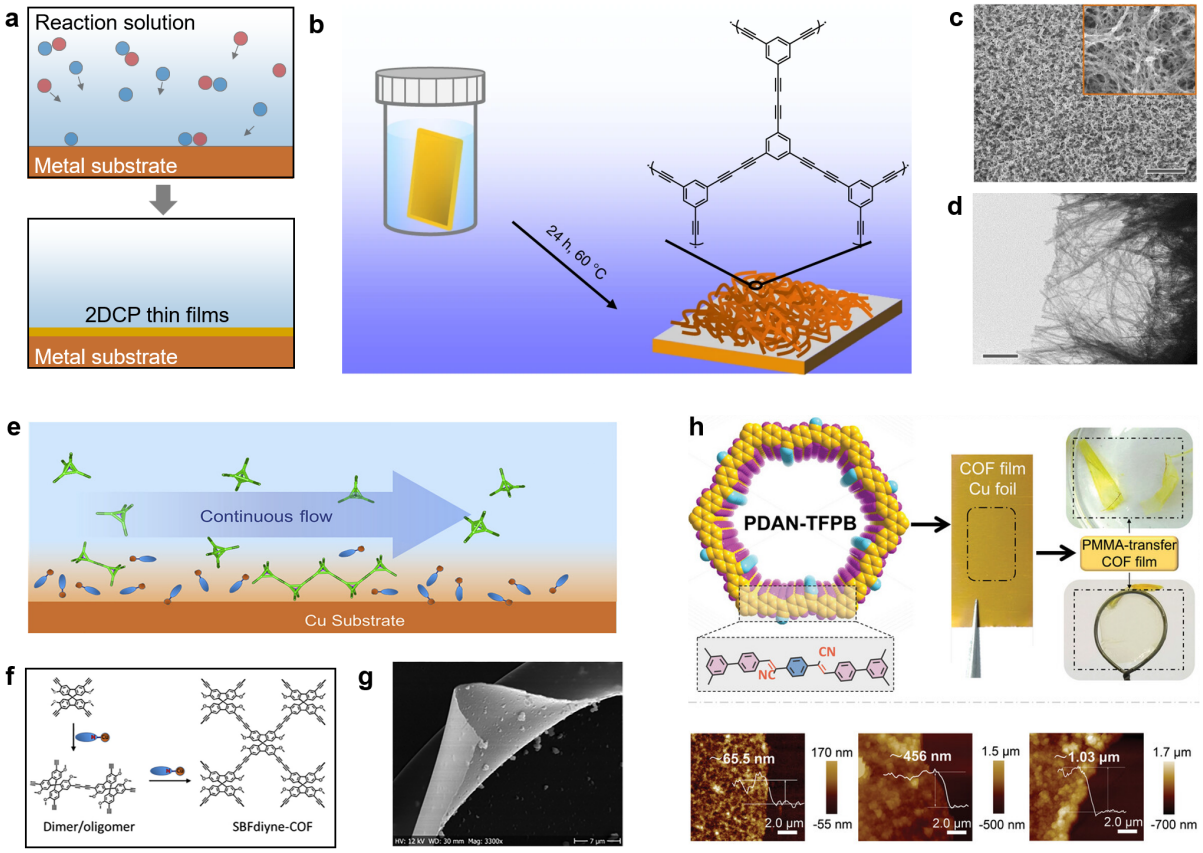

Figure 4. a) Schematic diagram of metal-substrate catalyzed 2D polymerization. b) Reaction scheme of synthesis acetylenic carbon-rich nanofibers. c) Scanning electron microscopy (SEM) images of PTEB nanofibers at Cu surface, scale bar: 10 μm. d) TEM image of PTEB grown on

a Cu grid, scale bar: 200 nm.[54] Copyright 2018, Nature Publishing Group. e-f) Illustration of the space-confined reaction at the vicinity of the Cu substrate. g) SEM image of a detached film.[55] Copyright 2022, Cell Press. h) Photograph of the PDAN-TFPB film grown on Cu foil, freestanding films in water after etching and films transferred to other substrates. AFM morphology and height profile analyses along the designated lines of PDAN-TFPB films prepared on the copper surface for 1, 3, and 72 hours, respectively.[56] Copyright 2023, Wiley-VCH.

Solid-liquid polymerization can also be divided into two steps, first preparing the assembly precursor, and then polymerizing at the interface to form films. Recently, Rahul Banerjee and co-workers[57] reported a solution-processable sphere transmutation technique to synthesize 2DCP thin films with two steps. In the first step, the crystallized nanospheres were synthesized in an environment with very dilute monomer concentration to prevent the precipitation of the amorphous phase and slow down the crystallization process. Subsequently, the nanospheres self-assemble on the substrate surface and initiate recrystallization, resulting in the oriented, crystalline, porous, crack-free 2DCP thin films. In a similar vein, the phase-switching strategy[53] requires a two-step procedure that decouples polymerization and crystallization by switching from the liquid to the gas phase (**Figure 3e**). The pristine films with reversible states were obtained in the liquid phase during the pre-assembly step, which were then transformed into highly crystalline and compact films through linkage rearrangement in the vapor phase of the catalyst and solvent.

Moreover, the metal surface-catalyzed reaction is also an ideal synthesis method for 2DCPs due to the confined surface reaction, where the substrate itself plays the role as catalyst source and provides a platform for the continuous fabrication of films (**Figure 4a**). For instance, the Glaser polycondensation is a typical substrate-catalyzed reaction for the synthesis of acetylenic polymers[58]. The copper atoms are extracted from the substrate (*e.g.*, copper foil) into the solution as Cu^{I} and Cu^{II} ion species under the impact of the organic base, thus forming a thin diffusion layer between the copper foil and solution. Finally, the polycondensation of the acetylenic monomer will occur in the confined space near the substrate, which provides the basic of 2D growth of the film with controlled thickness. Early in 2018, our group[54] reported a copper-surface-mediated strategy to synthesize poly(1,3,5-triethynylbenzene) (PTEB) nanofiber films (**Figure 4b**). The obtained PTEB films on Cu substrate exhibit nanofiber morphology (**Figure 4c**). The diameter of individual nanofibers ranges from 5 to 15 nm (**Figure 4d**). Recently, the copper-surface-mediated reaction has been applied into the fabrication of

films in a continuous flow method (**Figure 4e**)[55]. By controlling the interfacial reaction between the Cu substrate and a base flowing over the substrate, a detachable large area COF film with high continuity and surface smoothness was successfully prepared (**Figure 4f-g**). Furthermore, our group[56] demonstrated the copper-surface-mediated Knoevenagel polycondensation (Cu-SMKP) strategy to synthesize a series sp^2c-COF films. This approach provides a route for the fabrication of large-area and continuous sp^2c-COF films on various complicated Cu surfaces with thickness from tens to hundreds of nanometers (**Figure 4h**).

2.2. Air-liquid Interface Polymerization

Air-liquid interfaces can afford an ultra-flat reactor for monomer alignment prior to polycondensation, such as the air-water interface with a root-mean-square roughness of about 3Å,[59] which facilitates the 2D confinement growth at the interface (**Figure 5a**). The Langmuir-Blodgett (LB) technique can be performed on the air-water interface to confine water-insoluble monomers into a pre-organized monolayer. Subsequently, the monolayer is transformed into the targeted 2DCP thin films after triggering the polymerization by introducing the second monomer or catalyst (**Figure 5b**).[60,61] The obtained films can be further transferred to prepare organic electronic devices. Currently, the LB strategy has been broadly applied to construct single-layer and multilayer 2DCPs.[37,61] For instance, Xinliang Feng's group[49] employed this method to successfully prepare a series of porphyrin-based crystalline monolayer and multilayer 2DCP thin films through Schiff-base polycondensation at the air-water interface. The resulting monolayer 2DCP (2DP (4)) exhibits a large area of up to 4-inch wafers and excellent mechanical strength with Young's modulus of 267±30 GPa.

Besides the LB method, surfactant-monolayer-assisted interfacial synthesis (SMAIS) is also a general strategy to realize the controlled synthesis of few-layer 2DCP thin films with high crystallinity (**Figure 5c**). Surfactants, as typical amphiphilic molecules, closely stack to form highly ordered layers at the air-water interface while the hydrophobic tails toward the air and the hydrophilic heads face the water.[62,63] The surfactant monolayers guide the initial arrangement of the monomers to form the pre-organization layers, which facilitates the 2D polymerization on the water surface. For example, assisted by surfactant monolayers of sodium oleyl sulfate, the amine and anhydride monomers reacted on the water surface to synthesize few-layer 2D polyimide (2DPI) films.[64] The obtained films exhibit a thickness of ~2 nm and highly ordered structures with an average crystal domain size of ~3.5 μm^2 (**Figure 5d**). In addition to small-molecule surfactants, macromolecules also can mediate the interface polymerization. The ordered arrays of charged groups in macromolecules contribute to

stabilizing the oppositely charged molecular precursors and offer long-range ordering along the polymer chain.[65–67] For instance, negatively charged poly(sodium 4-styrenesulfonate) (PSS) diffusing at the air-water interface can induce the assembly of protonated monomers, facilitating polymerization and crystallization to form the films (**Figure 5e-f**). By using the PSS-mediated synthesis method, tetrakis(4-aminophenyl)-porphyrin (TAPP) condensate with dihydroxyterephthalaldehyde (2,5-Ph) to synthesize the wafer-sized thin film (COF-2,5-Ph). The resulting film is composed of single-crystalline domains with an average size of ~3.57 ± 2.57 μm^2.[68]

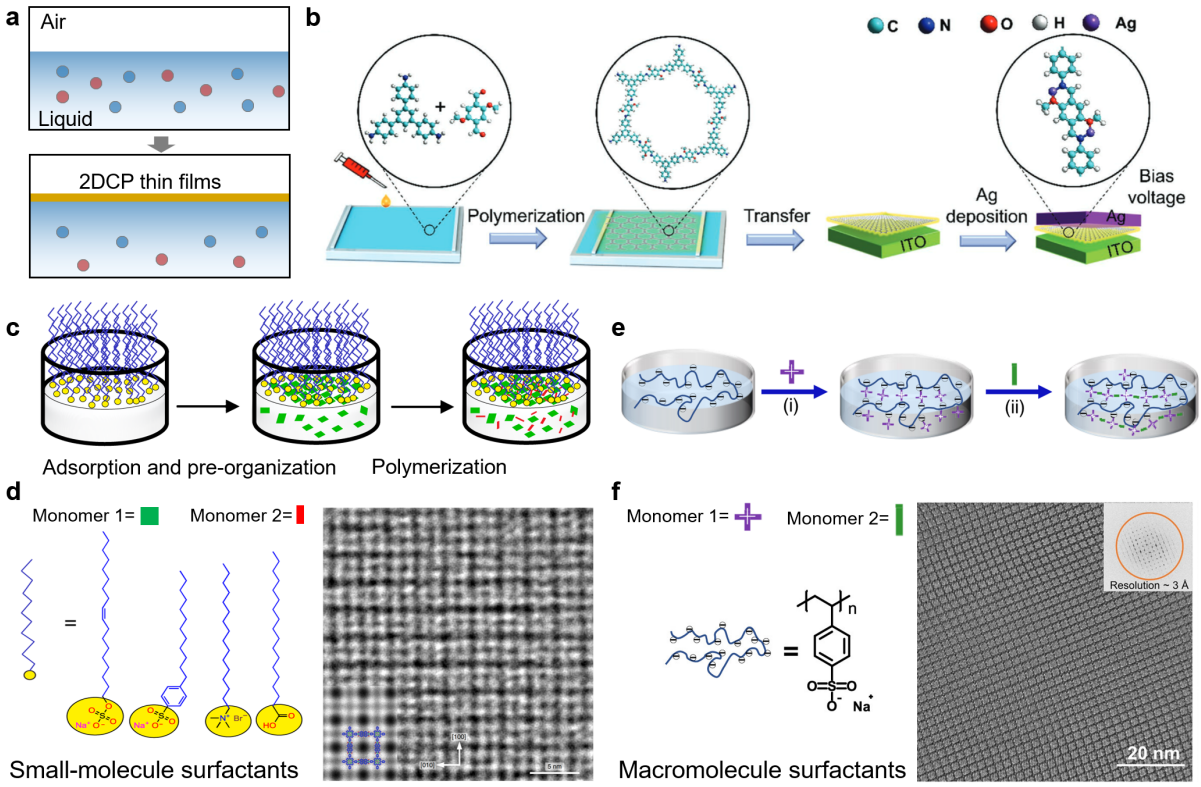

Figure 5. a) Schematic diagram of air-liquid interface polymerization. b) The LB technique to synthesize and transfer films.[61] Copyright 2022, Wiley-VCH. c) Schematic illustration of the synthetic procedure for the 2DCP thin films on a water surface assisted by the surfactant monolayer. d) The chemical structure of the surfactants applied and an HRTEM image and simulated image (inset) of 2DPI.[64] Copyright 2019, Nature Publishing Group. e) Overview of PSS-mediated synthesis strategy at the air-water interface. (f) The chemical structures of PSS and an HRTEM image and FFT pattern (inset) of COF-2,5-Ph.[68] Copyright 2022, American Chemical Society.

2.3. Liquid-liquid Interface Polymerization

The interface between two immiscible liquid layers (liquid-liquid interfaces) also provides a suitable 2D space to confine monomers for further 2D polymerization (**Figure 6a**). Like 2DCPs established at the air-water interface, the method also affords large-scale, free-standing, and high-crystalline films. One typical example is to synthesize crystalline 2DPC thin films *via* Schiff base reaction at the water-dichloromethane interface, as shown in **Figure 6b.**[69] In order to control the interfacial reaction rate for forming high-crystalline films, the salt-mediated technique [amine-p-toluene sulfonic acid (PTSA) salt] was introduced. The H bonding within the PTSA-amine salt suppresses the diffusion of the precursors through the interface, which promotes the reaction toward thermodynamically controlled crystallization. The approach allows for the construction of crystalline 2DCP thin films with controlled thickness ranging from ~50 to 200 nm, which are easily transferable to various substrates, including glass surfaces, metallic wires, and holey grids, while retaining their physical shape and crystalline structure. Besides the direct polymerization of monomers at the interface, the solution-processable 2DCP nanospheres can be mesoscale covalent self-assembly in the liquid-liquid interface to form self-standing 2DCP thin films.[70] The resulting 2DCP thin films show high crystallinity and a wide range of controllable thicknesses from 21 to 630 nm. In addition, discrete organic imine cages can also be transformed into 2DCP thin films at the liquid-liquid interface.[71]

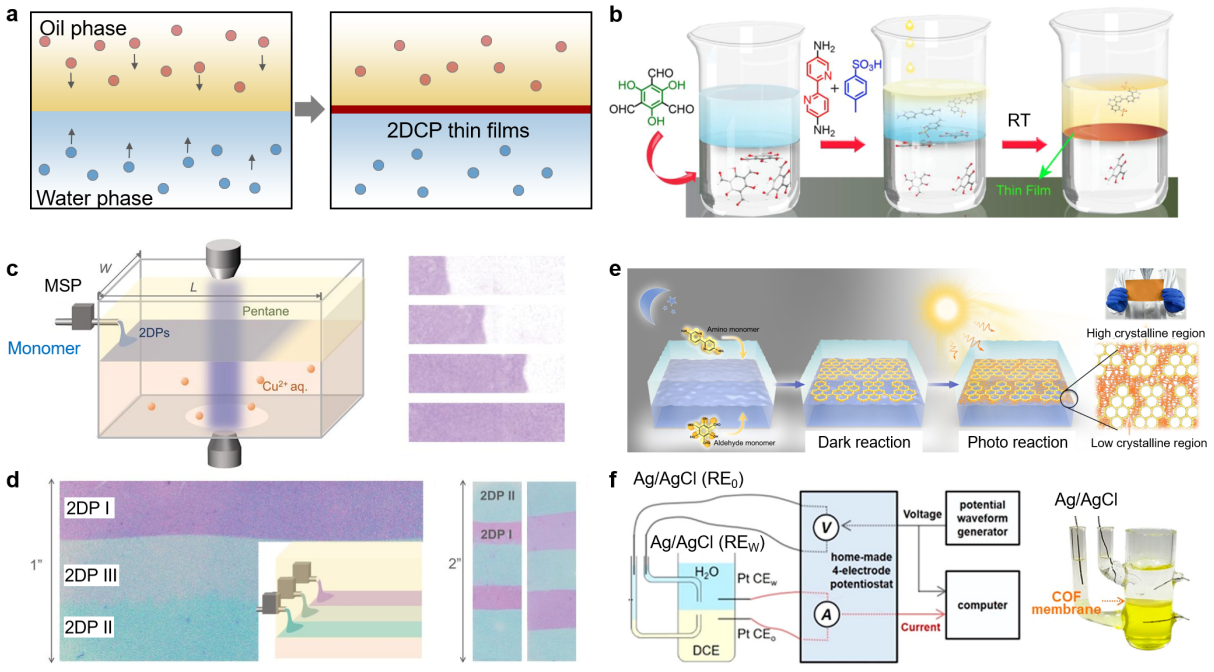

Figure 6. a) Schematic diagram of liquid-liquid interface polymerization. b) Schematic representation of the salt-mediated technique interfacial synthesis process for 2DCP thin films. The bottom layer contains methylene chloride and aldehyde monomers, while the top yellow layer corresponds to the amine-PTSA aqueous solution.[69] Copyright 2017, American

Chemical Society. c) Schematic of a LAP reactor and in situ optical characterization apparatus. MSP, micro-syringe pump. False-color images depict the 2DP I film at four distinct growth stages, with the film appearing purple. The field of view measures 6 mm by 24 mm. d) False-color image of 2DP I/2DP III/2DP II lateral junctions as well as the 2DP I/2DP II lateral junctions with tunable stripe widths.[72] Copyright 2019, Amer Assoc Advancement Science. e) Synthesis strategy of hetero-crystalline films through dark reaction and photo reaction based on interfacial polymerization, where the top light-blue layer is the aqueous phase and the bottom navy-blue layer corresponds to the organic phase.[73] Copyright 2019, Nature Publishing Group. f) Schematic diagram of electrochemistry applied for liquid-liquid interface synthesis and the corresponding glass cell.[74] Copyright 2017, American Chemical Society.

In the liquid-liquid interface polymerization process, the scalable synthesis of monolayer 2DCP thin films remains a significant challenge, primarily attributable to the difficulty of controlling reactions in the monolayer with large-scale uniformity. Jiwoong Park's group[72] developed a laminar assembly polymerization (LAP) technique that enables wafer-scale synthesis of monolayer 2DCPs. As shown in **Figure 6c-d**, the monomers were injected into the sharp pentane/water interface and then undergo self-assembly and polymerization. The pentane/water interface effectively confined the monomers within a monolayer, contributing to precise thickness control. Moreover, the pentane/water interface remains stable throughout the growth process, minimizing disturbances. The resulting 2DCP thin film exhibits a uniform and smooth surface with a thickness of 0.8 nm, which closely approximates the expected monolayer thickness. Furthermore, the 2DCP thin films share remarkable mechanical robustness and homogeneity, rendering them readily transferable onto diverse substrates as continuous films.
During interfacial polymerization, photoirradiation can interfere with the proton transfer of some chemical reactions, which show promising potential to regulate the films properties.[75] For example, photoinduced excited-state intramolecular proton transfer (ESIPT) can realize enolimine to ketoenamine tautomerization,[76,77] which provides the chemical basis to control the reactive-crystallization process by photoirradiation.[78] Therefore, modulation of photoirradiation, named photo-tailoring strategy, during liquid-liquid interfacial polymerization can synthesize thin films with different crystallinity (**Figure 6e**).[73] Under dark conditions, the reversible enol-imine linkage allows correcting the initial amorphous structure, providing high-crystalline films. Afterward, the introduced photoirradiation suppresses the "error-correcting" process through phototautomerization of enol-imine linkage to form low-

crystalline regions in the inter-crystalline defects. Subsequently, the low-crystalline regions tightly and flexibly link the high-crystalline regions to obtain the hetero-crystalline films.[73]

The electrochemical methodology is also suitable for the liquid/liquid interface to fabricate 2DCP thin films. As illustrated in **Figure 6f**, Bin Su's group[74] reported a potential difference-modulated biphasic strategy to synthesize large-area, self-standing 2DCP thin films at the polarized water/dichloroethane (water/DCE) interface, where HCl was dissolved in water as the catalyst and the monomers (both amine and aldehyde) were added to DCE. The external polarization of the water/DCE interface by the potential difference continuously pumps H^+ from water to organic solution to trigger the Schiff base reaction for growing 2DCP thin films. The film growth process can be real-time-monitored by conventional electrochemical methods applied to the liquid/liquid interface, like the interfacial double-layer capacitance measurement, while the permeability also can be in situ examined by heterogeneous ion transfer voltammetry. The facilely modulated potential difference across the water/DCE interface through electrolyte ions in two phases shows great potential for scalable synthesis of functional self-standing thin films. Three types of centimeter-scale, highly crystalline, and self-standing imine-linked 2DCP thin films with different pore sizes and surface functionalities were constructed, which prove the feasibility and versatility of this strategy.

2.4. Vapor-Solid Interface Polymerization

Chemical vapor deposition (CVD) enables the reaction between organic or inorganic films to be deposited and the other gases to fabricate organic films on substrates. (**Figure 7a)**.[79–81] The vapor-solid interface polymerization shares three distinct merits for the synthesis of 2DCP thin films. Firstly, the reaction rate can be facilely accelerated by raising the temperature without disturbing the interface, which facilitates the coordination of the polymerization and crystallization process.[82] Moreover, the polymerization process performed separately from the film-forming step is conductive to a higher-quality film with controllable thickness.[81] Yunqi Liu and Jianyi Chen's group[83] reported a vapor-induced process to synthesize a class of large-area imine-linked 2DCP thin films with controllable thicknesses in a CVD system (**Figure 7b-c)**. Firstly, the precursor 4,4′,4″,4‴-(1,3,6,8-Tetrakis(4-aminophenyl)pyrene (PyTTA)-film was deposited on substrates like SiO_2/Si, glass, Cu foil, and so on *via* thermal evaporation. The PyTTA film further reacted with volatile terephthalaldehyde (TPA) vapor through reversible Schiff base polycondensation to directly form uniform films on the substrates, which is driven by π-π stacking interactions with the aid of water and acetic acid. Wafer-scale 2DCP thin films

with diverse structures were synthesized by tailoring their building blocks, demonstrating the general applicability of this strategy.

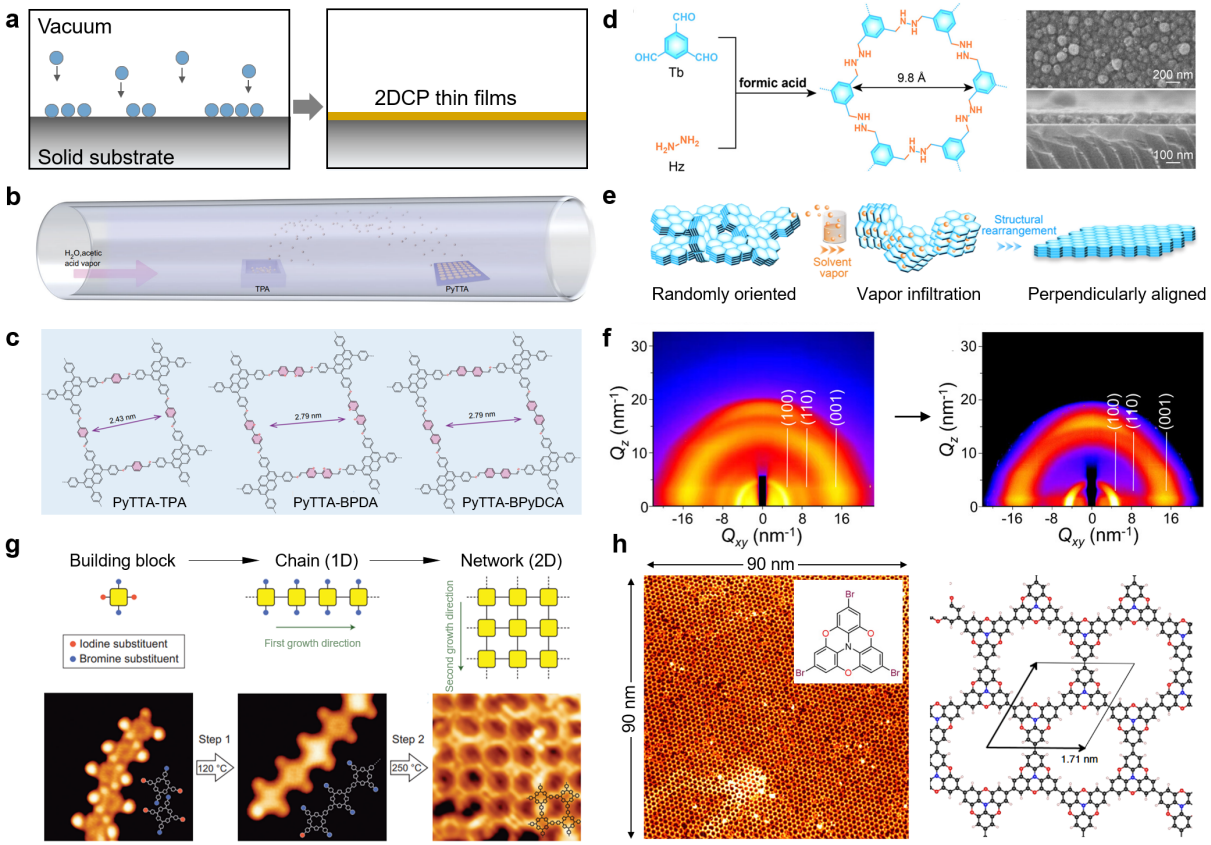

Figure 7. a) Schematic diagram of vapor-solid interface polymerization. b) Schematic illustration of the growth of 2DCP thin films through chemical vapor deposition with c) their chemical structures.[83] Copyright 2022, Nature Publishing Group. d) Synthesis scheme of amine-linked TbHz thin films. Surface (top) and cross-sectional (bottom) of SEM images. e) The o-DCB vapors penetration into TbHz films induces the crystal structure rearrangement from randomly oriented intergrown crystallites to perpendicularly aligned thin films. f) 2D grazing-incidence wide-angle x-ray scattering (GIWAXS) patterns of the TbHz film before and after annealing in o-DCB.[84] Copyright 2023, American Chemical Society. g) Schematic diagram of the sequential activation mechanism and corresponding STM images on Au (111) with scale bar of 8×8 nm^2, 10×10 nm^2, and 10×10 nm^2, respectively.[85] Copyright 2012, Nature Publishing Group. h) The STM image of P^2TANG on Au (111) with its DFT-simulated structure. Inset: the chemical structure of azatriangulene precursor.[30] Copyright 2020, Nature Publishing Group.

The solid-liquid interface synthesis easily constructs oriented 2DCP thin films due to the induced orientation effect of the substrate, such as the π-π stacking effect on graphene substrates.[86] In addition, vapor post-processing methods can also reorient 2DCP thin films. For instance, Yong Wang's group[84] proposed a solvent vapor annealing strategy to reorient pore channels from the anisotropic orientation to a perpendicular alignment **(Figure 7d-e)**. The solvent with low relative permittivity and conjugated structure, like o-DCB, is more suitable for the vapor annealing method, due to its strong affinity toward the 2DCPs and kinetically provided sufficient mobility for the crystallites to reorganize. The solvent vapor penetrates into the 2DCP interlayers to weaken the π-π interaction, further rendering the monolayers to dissociate and endowing the skeletons with structural mobility, which is instrumental to orienting 2DCPs in the favored direction.[84] The monolayers convert from random stacking into the face-on stacking fashion during the solvent vapor annealing reorientation process, in which the pores are perpendicularly aligned. The amine-linked 2DCP thin film by covalently linking triformylbenzene (Tb) and hydrazine hydrate (Hz) after o-DCB vapor annealing, realizes perpendicular alignment along the [001] direction **(Figure 7f)**.[84]

The development of scanning tunneling microscopy (STM) significantly advances the study of interface polymerization processes at the atomic level and in real space.[87] The STM tip-induced surface-assisted Ullmann reaction reported by Rieder's group[88] exhibited the promising potential to synthesize stable C-C linked conjugated polymers through dehalogenation aryl halide coupling.[89] However, the bottom-up construction of an ordered covalently bound network based on STM techniques is challenging due to the limitation of one-step connection processes. L. Grill's group[85] reported a step-by-step connection strategy through the selective and sequential activation of specific sites to fabricate 2DCPs with high quality. As shown in **Figure 7g**, the iodine substituent of porphyrin initially reacts with each other to form a 1D chain at 120 °C, followed by the bromine substituent reacting to establish a 2D network as the temperature rises to 250 °C. The irreversibility of such a covalent chemical reaction hinders the self-repair of defects, resulting in a small domain size and high defect density, which limits the application of the resulting 2DCPs. G. Contini's group[30] proposed a hot dosing approach coupled with rigid azatriangulene precursors allowing defect healing during the growth process, which enables the fabrication of mesoscale-ordered 2DCPs with domain dimensions exceeding 100×100 nm² on the Au (111) substrate (**Figure 7h)**.

2.5. Synthesis Essentials of 2DCP Thin Films

During the 2DCP thin films synthesis, the two common crystallization pathways: fiber-to-film and sphere-to-fil usually tend to form non-dense films (**Figure 8a**).[90,91] Therefore, the quality of film growth needs to be improved by regulating the reaction rate as well as the interfacial mass transfer process to enhance its device performance. In addition, due to the stochastic nature of the movement of monomers or oligomers in the solution phase, it is difficult to synthesize films with controllable orientation and their crystal structures are usually polycrystalline (**Figure 8b**).[35,92] Furthermore, controllable synthesis of highly crystalline or even monocrystalline 2DCP plays an important role in accurately characterizing their device performance and revealing their structure-property relationships (**Figure 8c**).[10,93] Moreover, many properties of 2DCP are determined by their thickness, and thus the synthesis of 2DCP with controllable thickness is important for their practical applications.

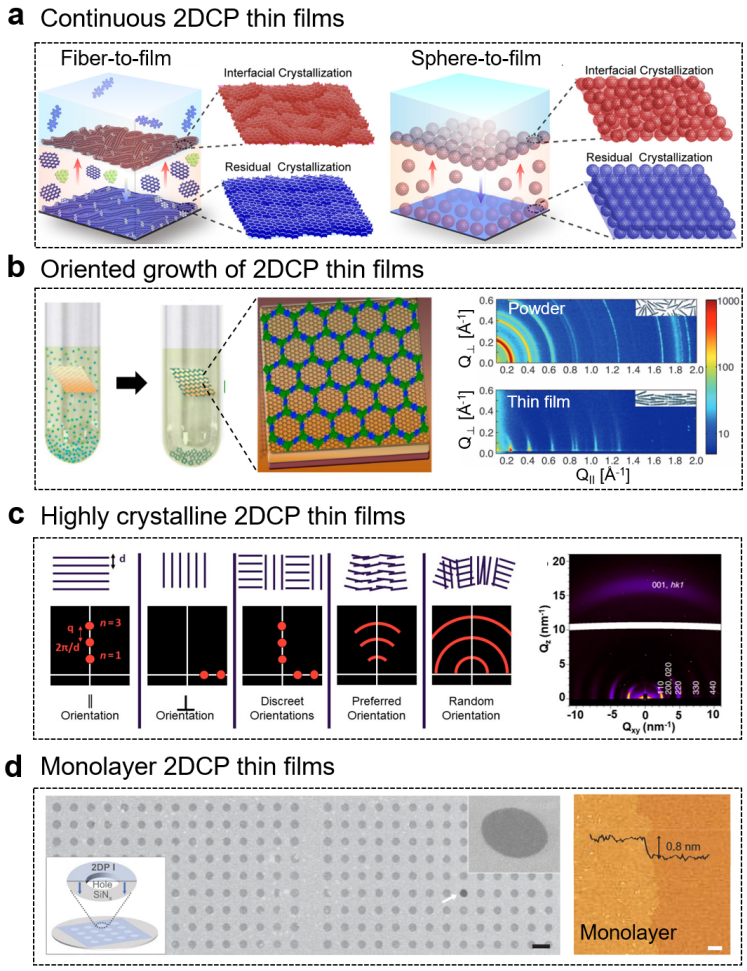

Figure 8. a) Interfacial and residual crystallization processes *via* self-assembly of nanofibers. Interfacial and residual processes *via* self-assembly of nanospheres.[51] Copyright 2021, the American Association for the Advancement of Science. b) Solvothermal synthesis of 2DCPs in the presence of a substrate-supported SLG surface.[94] Copyright 2011, the American

Association for the Advancement of Science. c) GIWAXS interpretation examples and representative GIWAXS pattern of a 2DCP thin film.[35] Copyright 2023 American Chemical Society. d) SEM image of monolayer 2DCP on a holey silicon nitride TEM grid with a thickness of 0.8nm.[72] Copyright 2019, the American Association for the Advancement of Science.

In particular, current works of novel interfacial synthetic protocol have facilitated the well-controllable synthesis of 2DCPs, but constructing large-area monolayer 2DCP under mild conditions remains challenging. So far, monolayer 2DCP nanostructures with tailored topology and functionalities on solid surface have been constructed under the STM control[30,87,95]. In addition, attempts to fabricate monolayer 2DCP under mild conditions have been reported, such as LAP technique for porphyrin-based 2DCP monolayer (**Figure 8d**),[72] which facilitate the nanotechnological devices and applications. Among the above approaches, the pre-assembly of precursors into monolayer at the sharp/ordered interface plays an essential role in the confined polymerization for producing monolayer 2DCPs. The monolayer or few-layer 2DCPs have been synthesized by the following methodologies: supramolecular surface assembly[96,97], surface tension-driven self-assembly[98–100] and spatially confined self-assembly[64,72]. In principle, the single-crystalline 2DCP monolayer will facilitate unlimited carrier transport and advanced device integration. Combined with the interfacial enhanced reactivity, the polymerization of highly self-assembled and confined monomers limited in the spatial resolution would favor single-layer growth of 2DCPs for high-performance electronics.

3. Conductive Properties of 2DCPs

3.1. Conductive Mechanisms

The diversity of structures and post-processing of 2DCPs complicate their conductive mechanism, which may include fundamental physical processes such as electronic transport and ionic transport. Most 2DCPs, as a branch of π-conjugated organic materials, share considerable in-plane conjugation and out-of-plane π-π stacking (**Figure 9a-c**).[101,102] The high degree of π conjugation of 2DCPs leads to weakly bound electrons and photo- or thermally excited free carriers, which migrate along the backbone through delocalized π orbitals and between molecules with sufficient π-π overlap. The electrical conductivity (σ) can be described by the carrier density (n) including electrons (e) and holes (h) as well as the corresponding mobility (μ).[103,104]

$$\sigma = e(n_e\mu_e + n_h\mu_h)$$

Therefore, higher carrier density and mobility are beneficial to enhance the electrical conductivity. The carrier density is determined by the activation energy (E_a), which is positively related to the energy band gap[103].

$$n = n_0 \exp\left(-\frac{E_a}{kT}\right)$$

where n_0, k and T denote the pre-factor, Boltzmann constant, and absolute temperature, respectively. Consequently, a narrow bandgap is typically favored. Strategies such as constructing donor-acceptor (D-A) structures to promote intermolecular charge transfer, as well as introducing conjugated linkage and large π-conjugated building blocks to facilitate charge delocalization, contribute to narrowing the band gap of 2DCPs.[105] In addition, doping also serves as a crucial strategy to enhance charge carrier density. The redox dopants not only act as electron-accepting or donating moieties but also play a role in diminishing the activation energy.[102] Mobility reflects the carrier transport efficiency. The summary of the carrier mobility of reported 2DCPs is listed in **Table 1**. In organic electronic materials, two principal carrier transport mechanisms, namely hopping and band-like transport (**Figure 9d-e**). In the hopping transport regime, the charge carriers are localized, and transfer between discrete and neighboring sites after activated. Mobility varies with hopping probability (P), which is influenced by spatial distance (R) and energy difference (ΔE) between neighboring hopping sites.[106]

$$P = \exp\left(-\alpha R - \frac{\Delta E}{kT}\right)$$

where α represents a constant related to the properties of the hopping site. Additionally, this mechanism tends to be positively correlated with thermal, which means increased temperature resulting in enhanced conductivity.[103] The hopping transport is commonly observed in disordered, conjugation-deficient, and defect-rich organic materials.[107] In the band-like transport mechanism, the robust interactions among the ordered neighboring sites enable the construction of continuous energy bands, allowing efficient transfer of delocalized charge carriers. The charge mobility is impacted by the effective mass (m^*) and scattering times (τ) of carriers.[27,103]

$$\mu = \frac{e\tau}{m^*}$$

where e denotes the elemental charge. The reduced effective mass coupled with longer scattering time contributes to enhanced mobility.

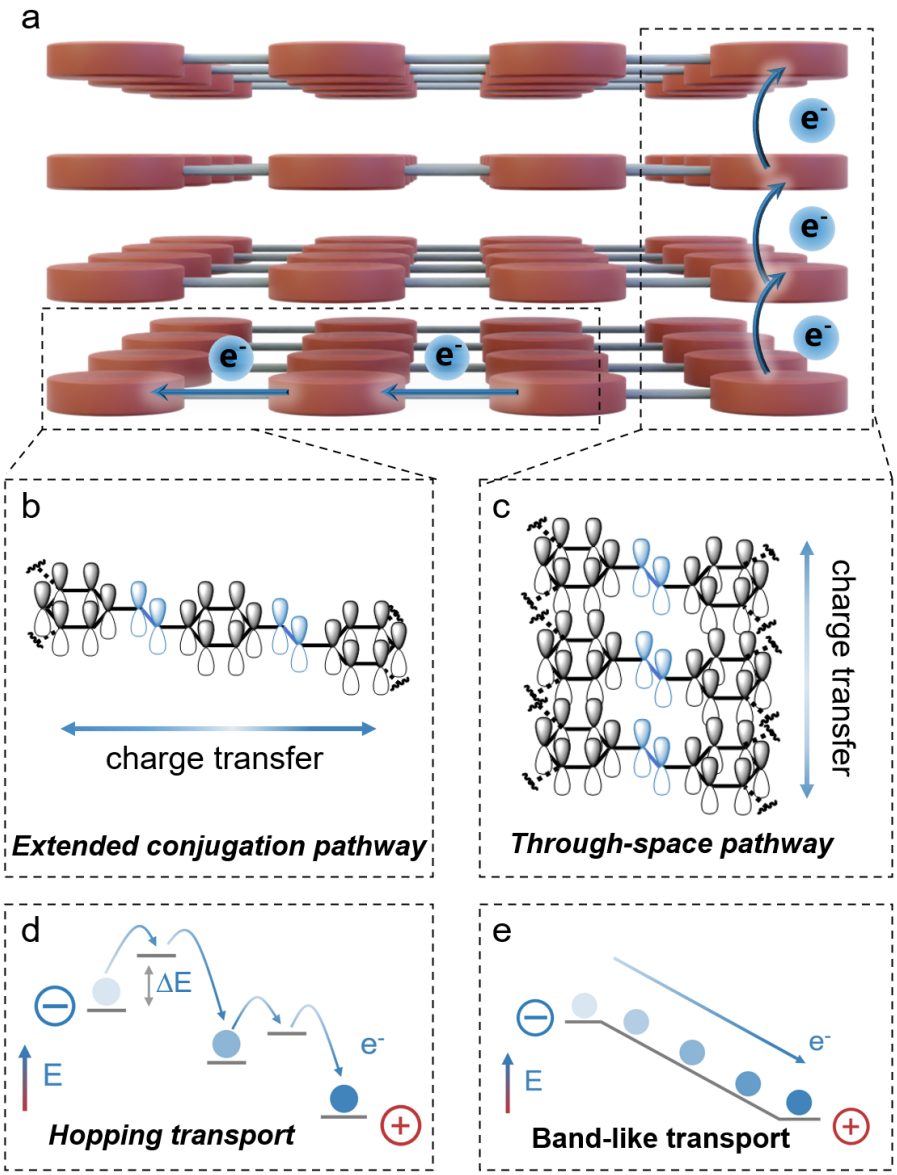

Figure 9. a) Orbital depictions of potential charge transport pathways within 2DCPs. b) The extended conjugation pathway of in-plane π-π conjugation c) The through-space pathway of out-of-plane π-π stacking. Schematic diagram of d) hopping charge transport and e) band-like charge transport in which electrons traverse from high to lower electric potential energy (represented as E). In hopping transport, electron motion is regulated by activation barriers (ΔE), whereas in band-like transport, electrons traverse a continuous energy landscape.

Table 1. Summary of the selected semiconducting properties of reported 2DCPs.

Material	Band Gap (eV)	Mobility ($cm^2 V^{-1} s^{-1}$)	Method	Refs
2DCP-NiPc film	1.33	971±44	THz	[27]
2DCP-CuPc film	1.28	460±31	THz	
sp^2-COF	-	22.1±2.7	THz	
sp^2-COF-6	1.31	2.3±0.5	THz	[108]
sp^2-COF-8	1.33	<0.1	THz	

sp^2-COF-9	1.07	5.8±0.9	THz	
I_2-sp^2-COF	-	51.1±3.1	THz	
I_2-sp^2-COF-6	-	5.7±0.3	THz	
c-HBC-COF	2.18	44	THz	[109]
DBOV-COF	1.74	0.6±0.1	THz	[110]
V-2D-COF-W1	2.18	1.4	THz	
V-2D-COF-W3	2.21	10.3	THz	
V-2D-COF-W4	2.26	0.6	THz	[111]
I_2-V-2D-COF-W1	-	3.1	THz	
I_2-V-2D-COF-W4	-	1.2	THz	
PI-2DP 1	1.4	0.01	THz	[112]
TPB-TFB COF	2.6	165±10	THz	[113]
HHTP-MIDA-COF	-	3.4	THz	[114]
CuPc-MIDA-COF	-	13.3	THz	
CuPc-pz COF	1.18	0.7 (h)	THz	[115]
ZuPc-pz COF	1.20	2.0 (h)	THz	
2DPAV-BDT-BT	1.62	~64.6	THz	[116]
2DPAV-BDT-BP	1.90	~16.8	THz	
CuPc-pz COF	1.18	0.9±0.2 (h)	Hall	[115]
ZuPc-pz COF	1.20	4.8±0.7 (h)	Hall	[115]
CuPc-MIDA-COF	-	8.2 (e)	Hall	[114]
COF-366	-	8.1 (h)	TRMC	[117]
COF-66	-	3.0 (h)	TRMC	
CS-COF	-	4.2 (h)	TRMC	[118]
H_2P-COF	-	3.5 (h)	TRMC	
CuP-COF	-	0.19 (e)	TRMC	[119]
ZnP-COF	-	0.032 (h)/0.016 (e)	TRMC	
NiPc COF	-	1.3 (h)	TRMC	[120]
HBC-COF	-	0.7 (h)	TRMC	[121]
TTF-Ph-COF	-	0.2 (h)	TRMC	[122]
TTF-Py-COF	-	0.08 (h)	TRMC	
2D D-A COF	-	0.01 (h)/0.04 (e)	TRMC	[123]
2DP (4)	1.4	1.3×10^{-6}	FET	[49]
I_2-2DP (4)	-	1.6×10^{-4}	FET	
2DPTTI	2.64	1.37×10^{-3}	FET	[124]
polyTB	~2.0	3.0×10^{-6}	FET	[125]

Note: the charge carrier mobility test methods: Terahertz (THz) spectroscopy, time-resolved microwave conductivity (TRMC), field-effect transistor (FET) and Hall effect measurements; e and h represent electron and hole carrier transport, respectively.

As an extended conjugated polymer, the optimized interlayer π orbital overlap and extended in-plane conjugation facilitate stronger energy band dispersion, which in turn diminishes the effective mass of carriers for better mobility. In terms of chemical structure, the incorporation of fully conjugated linkage (vinylene, imidazole of perinone, piperazine bonds, etc.) and redox active building blocks with planar π-planes is beneficial to regulate interlayer interactions and

improve energy band dispersion.[27,102,113] Additionally, the disorders or defects in structures hamper delocalization and π orbital overlap as well as cause a small τ, thus an ordered structure with high crystallinity is preferable.[26,126]

Apart from electronic currents, 2DCPs also show the potential for ionic conduction. The negative anions and positive cations are analogous to electrons and holes, respectively. For example, 2DCP thin films are often applied for proton transport.[127,128] Under humid condition, the entrapped water molecules and active protonic species, such as doped phosphoric acid or sulfonate and carboxylate groups on the skeleton, in the well-defined channels constructed a proton transport pathway *via* hydrogen bonding interactions.[129,129] On the other hand, under anhydrous conditions, proton transport ability relies entirely on active protic species.[130]

3.2. Impact of Linkage Chemistry on Conductivity

Linkage chemistry, assembling building blocks into 2D conjugated skeletons, is crucial for the intrinsic properties of 2DCPs (**Figure 10**). Firstly, the optimal synthesis conditions and achieved order structures of 2DCPs are highly dependent on the reactivity and reversibility of linkage chemistry. For example, Schiff-base reaction can readily synthesize high crystalline and oriented 2DCP thin films, but aldol condensation with higher reaction energy barrier requires harsher conditions while irreversible C-C coupling reactions (*e.g.,* Suzuki coupling, Stille reaction, direct arylation) cannot lead to the formation of highly crystalline 2DCPs when using common methods.[78,102] The ordered structure promotes charge transport while minimizing carrier trapping at defect sites.[131] Moreover, the bonding strength of linkages directly determines the chemical and thermal stability, for example, vinylene and pyrazine-linked 2DCPs with higher bond energy show better stability than the boronate ester or imine-linked 2DCPs.[41,132,133] Furthermore, the polarity and planarity of the linkages are significant for π-electron delocalization and conjugation extension over the 2DCPs. Owning to high polarization, imine linkages synthesized by Schiff base reactions feature moderate electron delocalization.[102,134] In contrast, fully conjugated and planar vinylene linkages obtained *via* Knoevenagel condensation,[132,135,136] aldol-type[50,129,137,138] or Horner-Wadsworth-Emmons (HWE) polycondensations,[139] exhibit enhanced π-electron delocalization for superior charge carrier transfer. In addition, the redox properties of the linkages also need to be taken into account. The open-shell species (*i.e.,* radical cations or anions) serve as mobile charge carriers, which may generate at the linkages after doping. For instance, the piperazine linkage, based on Buchwald-Hartwig cross-coupling reaction, is readily oxidized to cationic radicals,[140]

endowing the resulting 2DCP (NiPc-NH-CuPcF$_8$) after doping with high electrical conductivity (1.1×10^{-3} S cm^{-1}).[141]

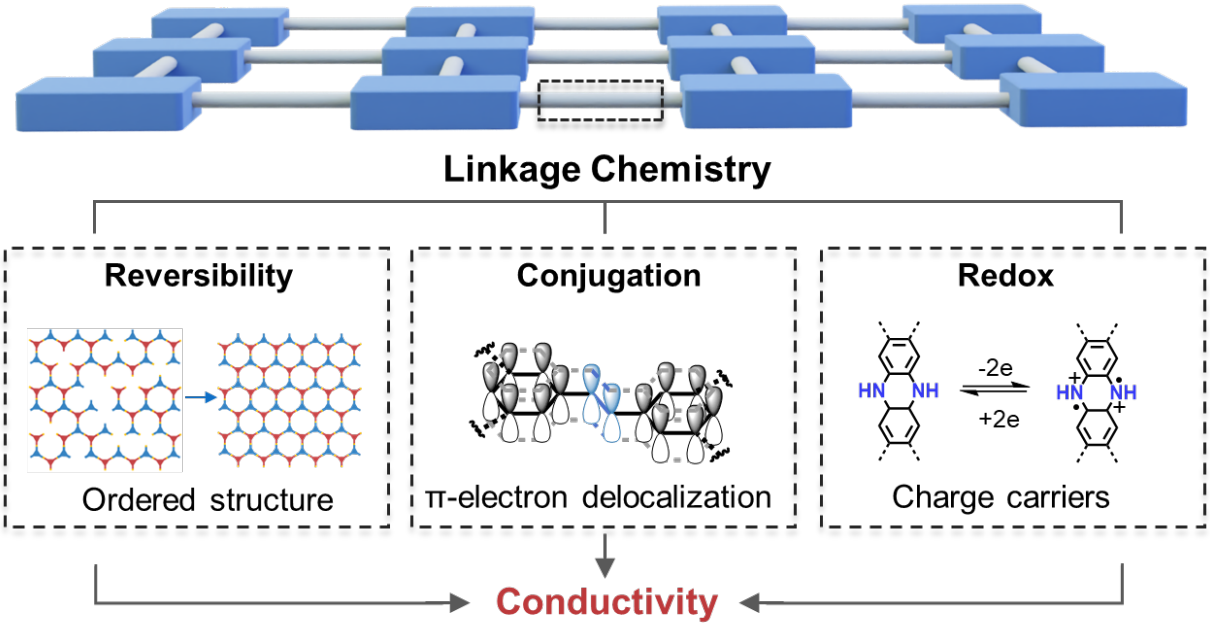

Figure 10. Schematic illustration of the impact of linkage chemistry on conductivity.

3.3. Impact of Building Blocks on Conductivity

The intelligent design and selection of building blocks are key to maximize the conductivity of 2DCPs, as the generation and migration of charge carriers are highly impacted by the intrinsic electronic properties of building blocks.[32] Highly electroactive blocks usually feature planar π-conjugation, which not only exhibits a better π-orbital overlap for efficient charge transport through and between the layers.[32] Moreover, the electroactive blocks also can be easily oxidized or reduced to form stable radical cations or anions as the source of charge carriers.[32,44] Electron-rich conjugated blocks, stabilizing cationic radicals easily, are suitable for constructing p-type organic semiconductors (**Figure 11a**).[44,102] For example, phthalocyanines and porphyrins featuring cyclic conjugated structures with delocalized 18 π-electrons participating in redox reactions and charge transport, are widely applied to construct high-electroactive 2DCPs.[142–146] The phthalocyanine nickel (II) based 2DCP (COF-DC-8) exhibits a room temperature intrinsic conductivity up to 2.51×10^{-5} S cm^{-1}, which can be further improved by 3 orders of magnitude after I_2 doping.[147] Interestingly, the charge-carrier type of phthalocyanine/porphyrin-based 2DCPs can be regulated by the coordinated central metal.[119,148] Heterotriangulenes with theoretically Dirac-cone-like electronic structures similar to that of graphene are expected to afford high charge-carrier mobilities and

conductivities.[31,149] Moreover, the electron-rich central amine of some azatriangulenes is readily oxidized to stable radical cations, thus enabling charge carrier injection after chemical doping. Perepichka and coworkers[150] firstly bulk synthesize azatriangulene 2DCPs (TANG-COF) as polycrystalline powders, which exhibits a conductivity of 1×10^{-2} S cm^{-1} after p-type doping with iodine. Seth R. Marder and William R. Dichtel's group[151] further applied benzophenone-imine-protected azatriangulenes (OTPA) and benzodithiophene dialdehydes (BDT) to synthesize OTPA-BDA thin films with controlled crystallite orientation. The conductivity of OTPA-BDT films were improved from 8.3×10^{-5} S cm^{-1} to 1.2×10^{-1} S cm^{-1} after orienting and hole-doping with tris(4-bromophenyl)ammoniumyl hexachloroantimonate. Tetrathiafulvalene (TTF), well known for its strong π-electron-donating abilities and two reversible oxidation processes, is a promising high-electroactive block.[152] The aligned TTF π columns within 2DCPs enable high-rate carrier transport and enhanced electric conduction upon oxidation.[122] The TTF-based 2DCPs, like TTF-COF[153], show doped conductivities up to 2.8×10^{-3} S cm^{-1}. There are also other strong electron-donating blocks reported, such as triphenylene and pyrene, introduced to construct p-type semiconductors with high conductivity.[154,155] In contrast, electron-withdrawing blocks, like naphthalene diimide,[107] triazines[156] and benzothiadiazole[123,157] are promising candidates for n-type or ambipolar semiconductors (**Figure 11b**). For instance, the naphthalene diimide (NDI)-based 2DCPs (TAPB-NDI and TAPPy-NDI) after doping with cobaltocene ($CoCp_2$) results in paramagnetic n-type semiconductors, in which NDI species are individually reduced to NDI radical anions.[107] The doped NDI-based 2DCPs achieve the maximum electronic conductivity of $>10^{-4}$ S cm^{-1}.

Besides the intelligent selections, the combination way of building blocks, such as constructing D-A structures, also significantly influences the conductivity of 2DCPs.[105] The 2DCPs exhibit huge potential to achieve numerous forms of D-A structures due to diverse topologies, various building blocks, modifiable pores, and layered stacking architectures (**Figure 11 c**). Initially, appropriate electron-deficient and electron-rich building blocks to construct an in-plane D-A structure can effectively promote the separation and transport of in-plane charge carriers.[158–161] The formed periodic and vertically aligned donor and acceptor columnar arrays facilitate ambipolar conduction, enabling efficient transport of both electrons and holes.[123,161] For example, the 2D D-A COF constructed from triphenylene donor units and benzothiadiazole acceptor units exhibited the hole and electron mobilities of 0.01 and 0.04 cm^2 V^{-1} s^{-1}, respectively, as well as considerable photoconductivity.[123] In contrast, structurally analogous COF-5, which only has D units without A units, exhibits negligible photocurrent under light irradiation.[123] The thiophene-bridged 2D CCP-Th with D-A structure demonstrated better

carrier separation efficiency (~ 0.7%) compared with biphenyl-bridged 2D CCP-BD (~ 0.2%).[162]

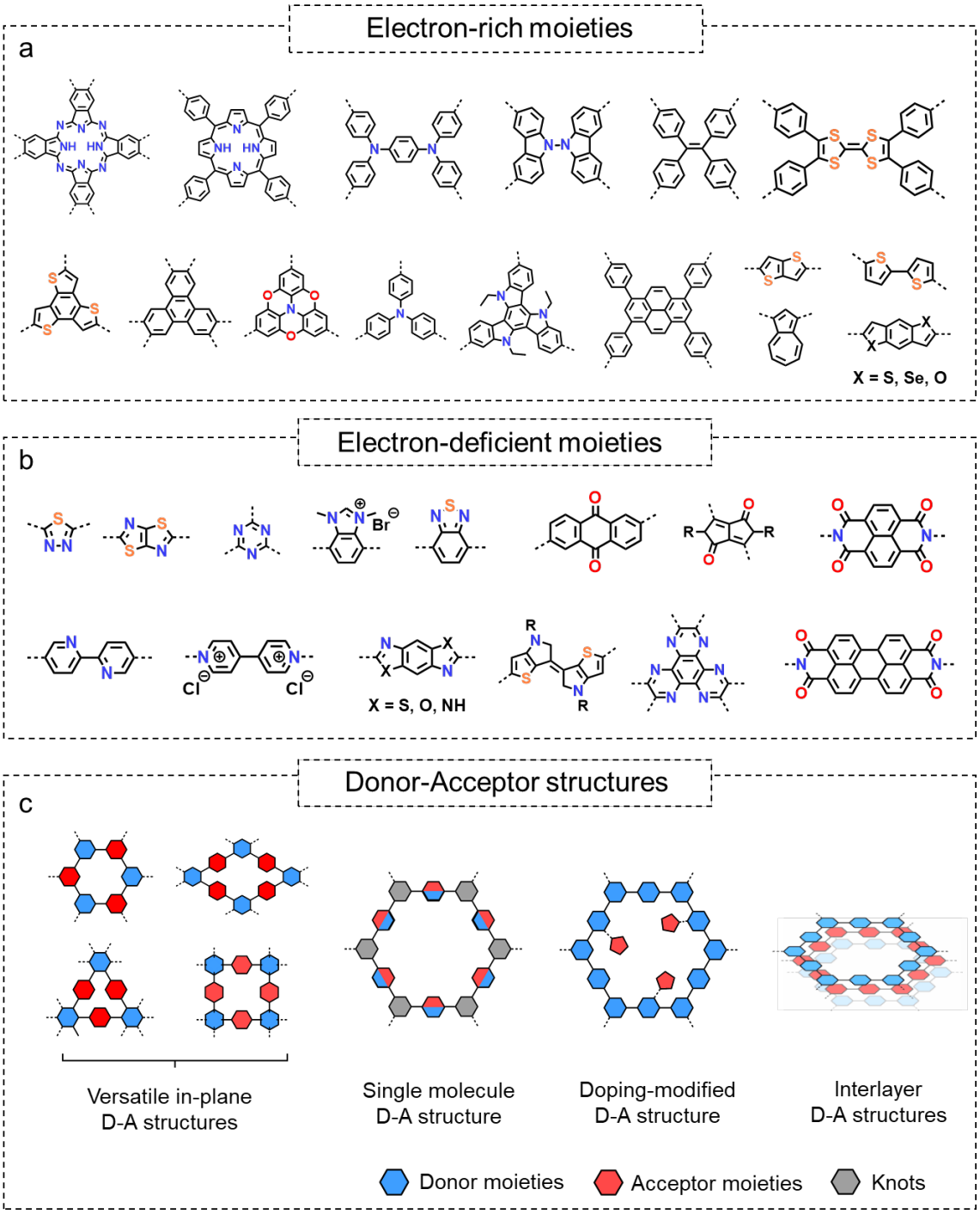

Figure 11. Common a) electron-rich and b) electron-deficient electroactive moieties as well as c) various D-A structures of 2DCPs.

Beyond the versatile in-plane D-A structures derived from the abundance of 2D topologies, the modification of channel walls represents an additional promising strategy. Thanks to the additional spatial confinement, the segregated D-A alignments, which are engineered by

covalently grafting suitable molecules or clusters onto the channel walls, such as buckyballs and tetracyanoquinodimethane (TCNQ), can effectively promote charge carrier separation and improve conductivity.[163–166] For instance, the electron-accepting buckyballs covalently anchored on the channel walls of electron-donating intermediate ZnPc-COFs could initiate photoinduced electron transfer and facilitate charge separation with radical species delocalized in the π-arrays.[163] After modifying buckyballs and TCNQ, the conductivity of the parent COF increased from 2.32×10^{-12} S cm^{-1} to 1.97×10^{-6} and 2.12×10^{-6} S cm^{-1}, respectively.[165] Moreover, D-A structures are also integrated into the single building block of 2DCPs. For instance, azulene, constituted by electron-rich five-membered and electron-deficient seven-membered sp^2 carbon rings, exhibits effective intramolecular electron pull-push effect and intrinsic redox activity, which promote charge transport by diminishing aromatic delocalization energy.[167] The as-synthesized azulene-derived 2DCP (COF-Az) exhibits an impressively narrow band gap (1.37 eV) due to its large dipole moment, significantly lower than that of the naphthalene-based 2DCP (COF-Nap: 2.28 eV).[168] Density functional theory calculations reveal that COF-Az possesses a stronger energy band dispersion than COF-Nap, which indicates a smaller effective carrier mass and better potential for carrier migration.[168] In addition, layer stacking enables 2DCPs to construct interlayer D-A structures by combining with polymer layers sharing various electronic properties[169] or other 2D materials (such as graphene[170] and MoS_2[171]). Owing to the proximity effect, the alternating D-A columnar arrays or van der Waals interfaces can effectively tune carrier density, boost electron-hole separation, and expedite charge transfer.[172–176] For example, the D-A intercalated 2DCPs, featuring alternating perylene imide-based covalent 2D layers as the D units and perylene layers as the A units, demonstrates efficient charge transfer capabilities.[176] Our group[169] constructed the layer-blocked 2DCP (LB-COF) heterogeneous film, featuring imine- and vinyl-linked layers, through two successive surface-initiated polycondensations. The S-scheme heterojunction, formed by two different polymer layers, effectively facilitates the separation of photogenerated electrons and holes.

3.4. Impact of Topology on Electronic Structures

The assembly of various-shaped building blocks with suitable symmetry results in 2DCPs potentially possessing multiple lattice topologies, theoretically exceeding 200 distinct configurations.[177,178] Notably, the lattice topology fundamentally influences the electronic properties of 2DCPs, including Dirac cones, topological flat bands, and topological insulators.[177] For instance, the honeycomb lattice (*e.g.,* graphene) gives rise to the famous

Dirac cones within the electronic band structure, where massless electrons reside at the Fermi level[179] (**Figure 12a-b**). Moreover, the 2DCPs featuring the Kagome lattice were theoretically predicted to share both Dirac cones and flat bands[31] (**Figure 12c-d**), where the flat bands quench the kinetic energy of charge carriers, which could offer the potential for intriguing phenomena such as the anomalous Hall effect[180], surface superconductivity[181], or superfluid transport[182]. However, such electronic structure of 2DCPs is still a theoretical assumption and has not been confirmed. Until 2020, Galeotti and co-workers[30] successfully synthesized the highly crystalline 2DCPs of P^{2}TANG with a Kagome lattice on Au(111) using rigid azatriangene precursors (**Figure 12e**). The predicted electronic band structure of Dirac cone structures and flat bands and experimentally observed by angle-resolved photoelectron spectroscopy (ARPES) (**Figure 12f**). Their work confirmed that lattice topology defining the electronic structures is feasible for 2DCPs. Furthermore, the bridging functionality of the triangulene (ether *vs* carbonyl) can effectively control the energetic positioning of the band and modulate the extension of conjugation without significantly perturbing the band structure, thereby further adjusting the effective mass of the 2DCPs.[95] These bridging groups can be tailored to engineer the electronic band structure and alter the ionization potential. Therefore, the rational design of electronic structures, *i.e.,* band structure engineering, necessitates the consideration of not only the properties of linkages and building blocks but also a particular focus on topology.

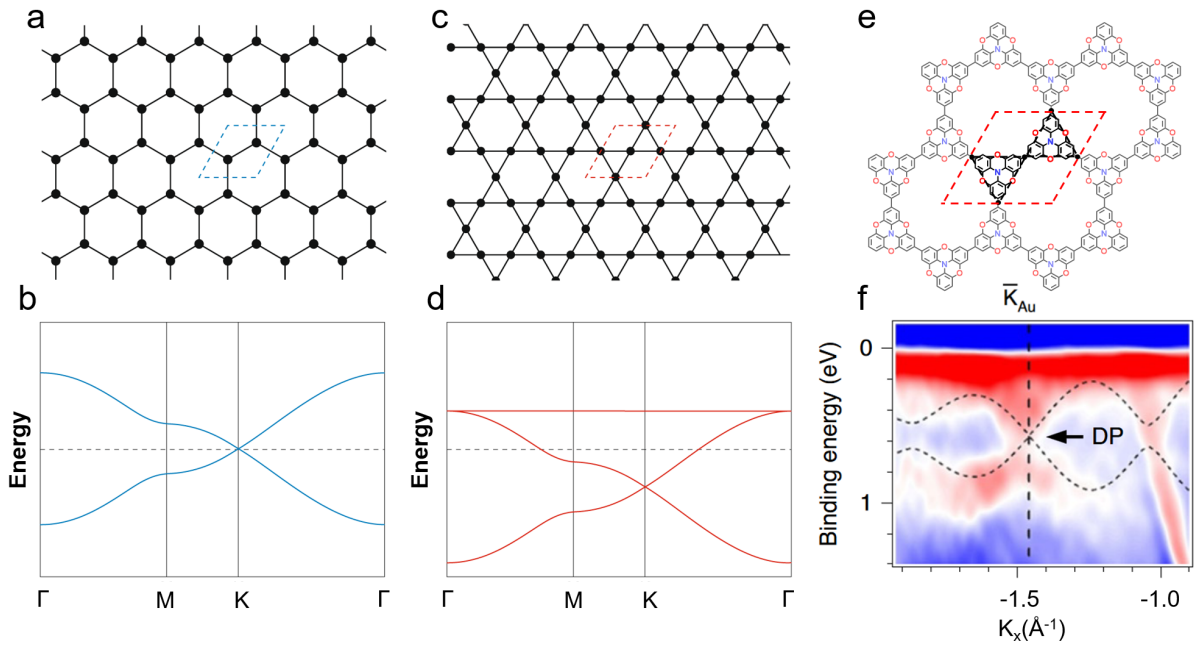

Figure 12. a) The honeycomb lattice topology and b) corresponding tight-binding band structure. c) The Kagome lattice topology and d) corresponding tight-binding band structure.[178] Copyright 2022, Nature Publishing Group. e) The chemical structure of P^{2}TANG.

f) The second-derivative maps of the ARPES signal from P^2TANG/Au(111), where the dashed lines represent calculated bands for P^2TANG and the label DP and black arrow emphasize the location of the Dirac point.[30] Copyright 2020, Nature Publishing Group.

3.5. Methodology for Improving Conductivity

3.5.1. Chemical Doping

2DCPs are often isolated as closed-shell organic species with limited charge carriers, which weaken the conductivity.[44] Chemical doping is a significant and general approach to increasing the conductivity of 2DCPs *via* introducing additional charge carriers (**Figure 13a**).[44] The comparison of conductivities of reported 2DCPs and their doping state is summarized in **Table 2**. The electronic structure of 2DCPs determines the optimal doping strategy. For instance, electron-rich 2DCPs with elevated Highest Occupied Molecular Orbital (HOMO) energy levels are commonly suitable for oxidant doping.[102,108] In contrast, electron-deficient 2DCPs with reduced Lowest Occupied Molecular Orbital (LUMO) energy levels can be effectively doped with reducing agents. Currently, experimental 2DCPs doping efforts are classified as p-type and n-type doping, primarily using iodine vapor, antimony pentachloride,[183] tetracyanoquinodimethane (TCNQ),[153] and 2,3,5,6-tetrafluoro-tetracyanoquinodimethane (F_4TCNQ)[183] as oxidants for holes as well as cobaltocene[107] as reductants for electrons. Iodine vapor doping has proven to be an efficient strategy to enhance the conductivity of different electron-rich 2DCPs. For example, after doping with iodine vapor, the conductivity of phthalocyanine-based 2DCPs (ZnPc-pz and CuPc-pz) increase from 7.0×10^{-7} to 3.1×10^{-4} S cm^{-1} and 3.3×10^{-7} to 1×10^{-4} S cm^{-1},[184] the pyrene-based 2DCP (Py-sp^2-COF) improves from 6.1×10^{-14} to 7.1×10^{-4} S cm^{-1},[132] the azatriangulene-based 2DCP (TANG-COF) enhances from 6.1×10^{-5} to 1.0×10^{-2} S cm^{-1},[150] and tetrathiafulvalene-based 2DCP (TTF-COF) heightens from 1.2×10^{-6} to 2.8×10^{-3} S cm^{-1}.[153] The fundamental study of the iodine doping interactions within the lattice in phthalocyanine-based 2DCP (ZnPc-pz) revealed that iodine molecules are preferentially located in the pores and near the skeleton.[184] The improved conductivity after doping is likely attributed to the ordered carrier migration path formed by the electron donor (ZnPc-pz) and acceptor (iodine).[184] Notably, due to weak oxidant strength and high volatility, the high vapor pressure demanded for doping triggers excess iodine accumulated within 2DCPs which disperses over time, thus impairing the stability of device performance.[153] Moreover, uncontrolled p-type doping with iodine vapor provides little control over the number of free carriers introduced into these materials.[185] Recently, the study concerning the effect of various dopants, including iodine, antimony pentachloride, and F_4TCNQ, on the conductivities of

doped 2DCPs indicate that strong acceptor F_4TCNQ greatly boosts the radical cation density (up to 0.5 radicals per unit cell) and the resulting 2DCPs achieve a long-term stable conductivity as high as 3.67×10^{-2} S cm^{-1}.[183] Cobaltocene ($CoCp_2$) as a controlled n-type dopant can be introduced in well-defined stoichiometric amounts. When applying $CoCp_2$ dopes naphthalene diimide (NDI) based 2DCPs, NDI-species can be reduced to NDI-radical anions, thus producing paramagnetic n-doped 2DCPs with a maximum conductivity of 6.0×10^{-4} S cm^{-1}.[107]

Table 2. Comparison of conductivities of reported 2DCPs and their doping state.

Material	Sample type	Conductivity (S cm^{-1})		Refs
		Before doping	After doping	
OTPA-BDT COF / Magic Blue	Film	8.3×10^{-5}	1.2×10^{-5}	[151]
TANG-COF / I_2	Pellet	1.6×10^{-5}	1.0×10^{-5}	[150]
NiPc-NH-$CoPcF_8$ /I_2	Film	1.27×10^{-1}	1.29×10^{-1}	[141]
NiPc-NH-$CuPcF_8$ /I_2	Film	1.15×10^{-1}	1.12×10^{-1}	
TTF-COF / I_2	Film	1.2×10^{-6}	2.8×10^{-3}	[153]
ZuPc-pz-I_2	Pellet	7.0×10^{-7}	3.1×10^{-4}	[184]
CuPc-pz-I_2	Pellet	3.3×10^{-7}	1×10^{-4}	
Py-sp^2-COF / I_2	Pellet	6.1×10^{-14}	7.1×10^{-4}	[132]
WTA / F_4TCNQ	Film	3.78×10^{-8}	7.35×10^{-7}	[183]
WBDT / F_4TCNQ	Pellet	2.70×10^{-6}	3.67×10^{-2}	[183]
	Film	1.64×10^{-5}	2.18×10^{-2}	
WBDT / I_2	Film	1.64×10^{-5}	1.33×10^{-4}	[183]
TTF-Ph-COF / I_2	Film	1.2×10^{-6}	2.8×10^{-2}	[153]
TAPFY-COF	Film	2.8×10^{-4}	-	[186]
COF-DC-8 / I_2	Pellet	2.5×10^{-5}	10^{-2}	[147]
TTF-DMTA	Film	1.3×10^{-6}	-	[187]
PyVg-COF	Film	4.0×10^{-3}	-	[188]
NiPc-CoTAA / I_2	Film	8.16×10^{-5}	5.2×10^{-3}	[143]
$TpAzo_{F\text{-}F}COF$	Film	2.6×10^{-5}		[51]
$TpAzo_{S\text{-}F}COF$		3.7×10^{-5}		
TAPPy-NDI / $CoCp_2$	Pellet	$<10^{-9}$	6×10^{-4}	[107]
TAPB-NDI / $CoCp_2$			7×10^{-5}	

3.5.2. Interlayer Polymerization

Solid-state topological interlayer polymerization (SSTP), constructing conjugated connections between adjacent layers, provides an intelligent strategy to improve the conductivity of 2DCPs (**Figure 13b**). Owing to the unique stacking of 2DCPs, Xiao Feng and Bo Wang's group[186] successfully transformed the well-organized diacetylene columnar arrays into conjugated enyne chains as the extra charge carrier pathways. After interlayer polymerization, the resulting TAPFY-COF-P exists a significantly narrowed bandgap (from 2.25 to 1.54 eV) and enhanced conductivity without doping (from 2.2×10^{-5} to 2.8×10^{-4} S cm^{-1}). The enhanced conductivity realized by the SSTP method also can address the problems caused by doping with iodine or

other redox-active molecules, such as pore occupation and irreversible structural destruction.[186]

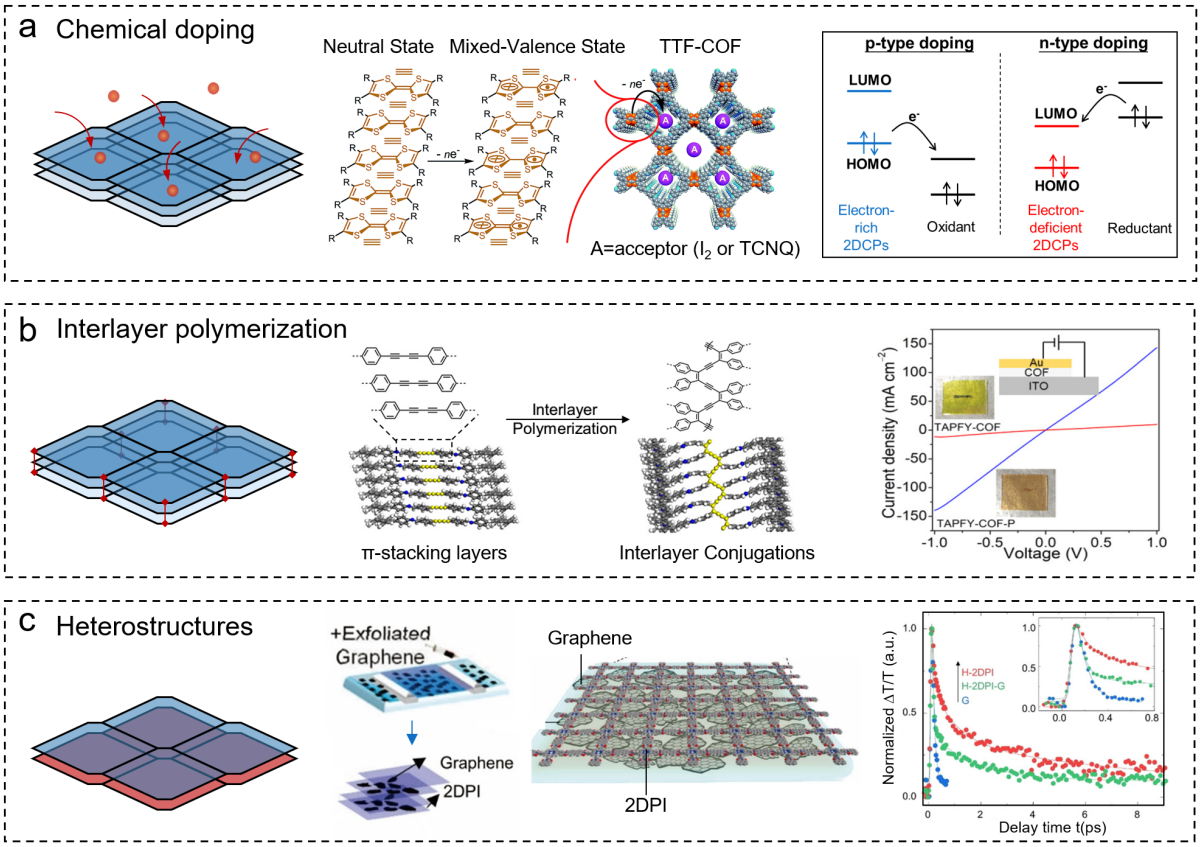

Figure 13. a) Schematic diagram of chemical doping strategy, and the neutral state and mixed-valence state of TTF-COF as well as the energy level diagram for p-type and n-type doping.[153] Copyright 2014, Royal Soc Chemistry. b) Schematic representation of the interlayer topological polymerization strategy and the I-V curves of original TAPFY-COF film and after interlayer polymerization.[186] Copyright 2021, American Chemical Society. c) Schematic diagram of the constructing van der Waals heterostructures strategy and a diagram of 2D polyimide-graphene heterostructures with its femtosecond transient absorption spectroscopy upon protonation.[170] Copyright 2021, Wiley-VCH.

3.5.3. Constructing van der Waals Heterostructures

Coupling 2DCP films with other 2D materials to construct van der Waals heterostructures (vdWHs) can facilitate the interfacial electron transfer process and enhance the carrier density, thereby improving their electronic properties. For instance, 2D MoS_2 as a typical semiconducting, single-layer-thick versatile platform, shares high mechanical robustness, and strong spin-orbit as well as favorable electronic and optical properties, which show great

potential to generate hybrid vdWHs with tunable charge transport properties.[189] Our group[171] fabricated the hybrid MoS_2/2D-COF vdWHs by transferring the imine-based 2D-COF films onto the monolayer CVD MoS_2. The resulting vdWHs induce efficient charge transfer from 2D-COF film to MoS_2 and suppress phonon-electron scattering effects in the MoS_2 lattice, which caused an enlargement of the free charge carrier density up to 10^{12} e^-/cm^2. The MoS_2 combined with 2D-COF TAPB-TFPB film achieved increased carrier mobility of 21.1 $cm^2V^{-1}s^{-1}$, fourfold higher than the pristine (5.2 $cm^2V^{-1}s^{-1}$). Xinliang Feng's group[190] utilized few-layer MoS_2 and 2D polyimide (2DPI) films to fabricate electronically coupled 2DPI-MoS_2 vdWHs featuring a face-to-face stacking arrangement through the wet transfer method. Thanks to the robust interlayer coupling at the vdWHs interface, the prepared 2DPI-MoS_2 vdWHs device exhibited an impressive electron mobility of up to 50 $cm^2V^{-1}s^{-1}$. In addition, they[170] also constructed 2D polyimide-graphene (2DPI-G) vdWHs *via* the on-water synthesis and assembly strategy. As revealed in femtosecond transient absorption spectroscopy, the resulting 2DPI-G vdWHs after protonation exhibited a strong acceleration of interlayer charge transfer (ca. 60 fs) from 2DPI to graphene (**Figure 13c**). Apart from MoS_2 and graphene, other 2D materials such as hexagonal boron nitride (h-BN), phosphorene, and MXene also possess the hybridization potential. In addition to constructing the vdWHs through transfer methods, such 2D materials can also serve as substrates to promote the oriented growth of 2DCP thin films.[86,94] Orientation and order are important factors affecting the conductivity of 2DCPs thin films. Long-range ordered crystal architecture contributes to suppressing the carrier trapping at defects and weakening adverse effects induced by boundary effect, thereby facilitating efficient charge transfer along the conjugated path.[191,192] For example, the well-oriented 2DCPs (AntTTH) films exhibit a maximum intrinsic photoconductivity of 7.2×10^{-5} cm^2 V^{-1} s^{-1} upon 355 nm laser excitation whereas the randomly oriented powder sample with smaller crystalline region only show negligible photoconductivity.[191] Orientation also facilitates charge storage, such as the oriented crystalline DAAQ-TFP COF thin films share improved charge storage capacity from 0.4 to 3 mF cm^{-2} in comparison with the same COF with randomly oriented microcrystalline. [193]

4. Applications of 2DCPs in Organic Electronics

4.1. Organic Field-Effect Transistors

Field-effect transistors (FETs) are a class of three-terminal microelectronic devices consisting of a source, drain, and gate electrodes, which control source-to-drain current according to the gate voltage.[194] The gate voltage modulates the charge distribution in the channel through the

electric field to govern the current state. Therefore, the channel material, as one of the key parts of FETs, directly affects the performance and characteristics of the FETs, such as threshold voltage, charge carrier mobility, and on-off current ratio.[195] Besides common metal oxides, organic materials share great potential in active layers of the channel due to their low power consumption, flexibility, and diverse functionality, especially 2DCP thin films with expanded conjugated systems, tunable electronic structures, robust stability, and high carrier mobility.[196]

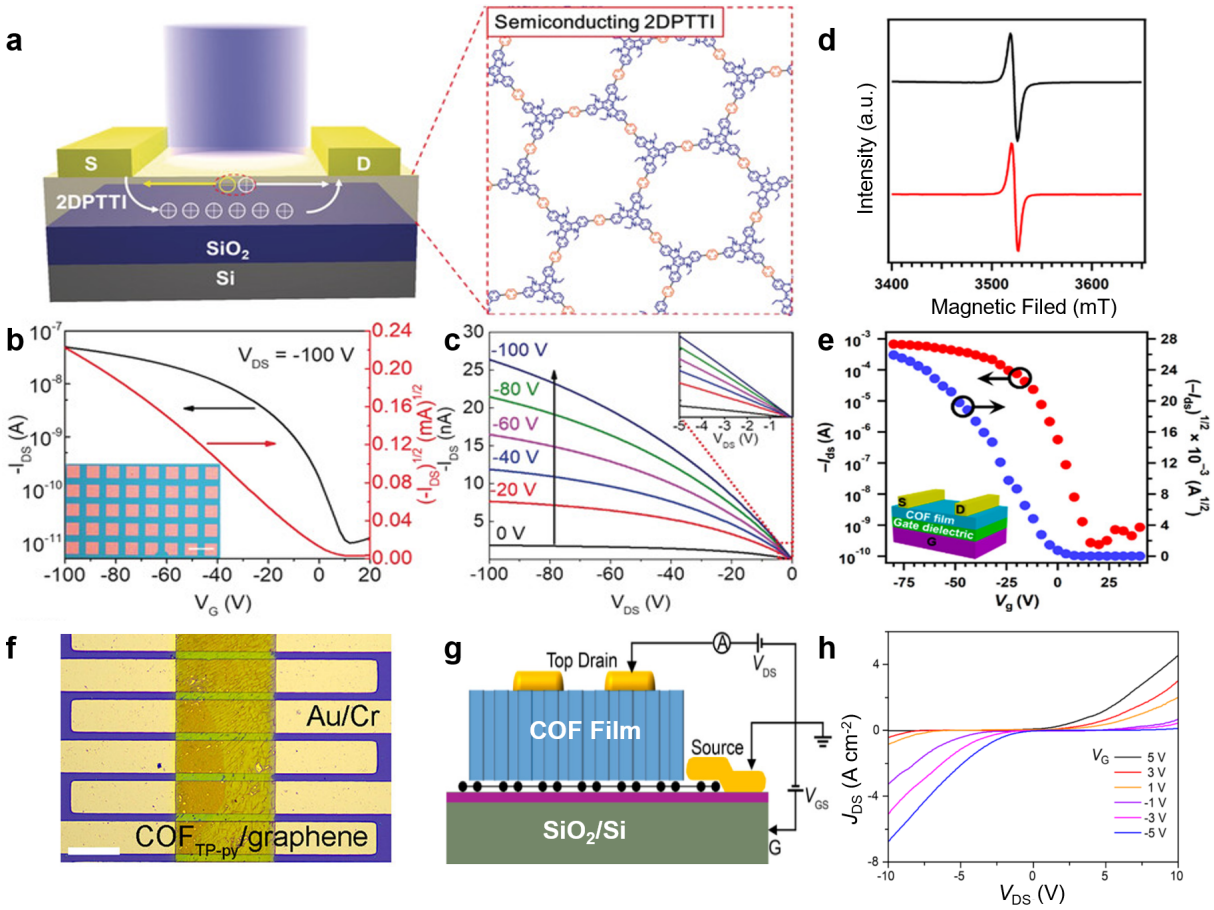

Figure 14. a) Schematic diagram of 2DPPTI-based OFET device and chemical structure of 2DPPTI. b) The representative transfer and output curves of 2DPTTI-based transistors. Inset: the optical microscopy image of 2DPTTI transistor arrays. c) The output curves of 2DPTTI-based transistors, the inset is enlarged output curves at low voltage.[124] Copyright 2020, Wiley-VCH. d) The EPR spectrum of pristine NiPc-NH-CoPcF$_8$ (black curve) and iodine-doped NiPc-NH-CoPcF$_8$ (red curve). e) The transfer curves of NiPc-NH-CoPcF$_8$-based transistor device (Vds = -80 V; inset, device structure).[141] Copyright 2022, American Chemical Society. f) The Optical microscope image of the COFTP-py/graphene channel.[197] Copyright 2022, American Chemical Society. g) Schematic diagrams of the constructed COF/SLG-VOFET device. h) The output curves of the ambipolar SLG/COF$_{TFPy-PPDA}$-VOFET under various gate voltages.[192] Copyright 2017, American Chemical Society.

Schiff base condensation is widely explored to synthesize imine-linked 2DCP thin films due to its high reactivity and reversibility.[78,198] In particular, intramolecular hydrogen bonds formed by the imine and surrounding functional groups (such as hydroxyl groups) are beneficial to improving the structural rigidity, crystallinity, and stability of the synthesized monolayer and multilayer 2DCPs.[49] The robust thin film also facilitates further transfer and integration into devices. The fabricated transistor device, employing imine-linked polymer films containing hydroxyl functional groups as an active semiconducting layer, obtained the mobility of 1.3×10^{-6} $cm^2\ V^{-1}\ S^{-1}$ and an on/off ratio of 10^2 as well as an enhanced mobility of 1.6×10^{-4} $cm^2\ V^{-1}\ S^{-1}$ after doping with I_2.

Apart from imine linked, C-C bonded 2DCP thin films attracted extensive attention due to their robust stability against acid-base and thermal erosion and extending π conjugation for charge carrier migration. Recently, Wenping Hu and Huanli Dong's group[124] reported a wafer scale free-standing 2DPTTI film synthesized by a modified interfacial Suzuki reaction from 2,7,12-tribromo-5,10,15-triethyltriindole (2-BrTTI) and 1,4-benzenediboronic acid dipinacol ester (BADE) precursors at room temperature. To explore the organic electronic properties of 2DPTTI films, the OFETs were constructed utilizing a bottom-gate top-contact device geometry on Si/SiO_2 (300 nm) substrate and a top light illumination mode for phototransistors (**Figure 14a**). As indicated in the representative transfer curves of **Figure 14b,** the resulting 2DPTTI films shared the typical p-type semiconducting properties. The linear character in output curves reveals the efficient charge injection between the 2DPTTI film and the source/drain electrode (**Figure 14c**). The resulting 2DPTTI-based devices exhibit a low threshold voltage (lower than 10 V) and a high current on/off ratio of 5.0×10^3 with the saturation charge carrier mobility of up to 1.37×10^{-3} $cm^2\ V^{-1}\ s^{-1}$. Excellent π-delocalized conjugation for efficient charge transport and fast photoelectronic conversion also endow 2DPTTI films, as photodetectors, with a high photosensitivity of 3.7×10^3 and an excellent photoresponsivity of 1.4×10^3 $A\ W^{-1}$ under gate voltage = 10 V with an illumination intensity of 0.4 $\mu W\ cm^{-2}$. Furthermore, the photocurrent enhanced nearly 100-fold upon exposure to HCl vapor (ca. 30 s), which may be attributed to the protonation effect of the indole ring nitrogen atom Lewis-basic site of 2DPTTI facilitating extended conjugation. The efficient delocalized conjugation of π electrons in two dimensions ensures isotropic charge transport properties, which are non-negligible for large-area device applications. The piperazine linkage is easily oxidized to cationic radicals, resulting in the prepared 2DCPs sharing high electrical conductivity after doping oxidant, which shows great potential to serve as the active layer in FET devices.[141] For

instance, the piperazine-linked phthalocyanine-based 2DCP thin film (NiPc-NH-$CoPcF_8$) already contains open-shell species under oxidation by atmospheric oxygen, which also exhibits the same electron paramagnetic resonance (EPR) signal detected in the iodine-doped sample (**Figure 14d**) [141]. The NiPc-NH-$CoPcF_8$ COF based OFET device exhibits a prominent gate modulation in the transfer characteristic curve **(Figure 14e)**. The drain-source current increased as the gate voltage decreased indicating the p-type nature of the device. Moreover, the prepared OFET devices share the saturation regime hole mobilities of 0.13 - 0.34 $cm^2 V^{-1} s^{-1}$, the on-off current ratios of > 10^6, and the threshold voltages between -16.5 and 1.52 V.[141]

Compared with traditional assay techniques, OFETs are a promising chemical sensor platform due to the advantages of label-free detection, fast response, biological compatibility, high portability, and user-friendliness.[199] For example, the graphene OFET (g-OFET) channel generates high-sensitive conductance changes during the interaction of molecules with graphene, due to the chemical doping effect concerning interfacial electrostatic induction or charge transfer varying the electric potential of graphene.[200,201] The sensitive detection of OFETs is determined by chemical gating modulation, relying on the charge quantity and/or the redox properties of the analyte molecules.[197] Compared with macromolecules including proteins and nucleic acids, most small molecules with few charges and weak redox properties result in minimal chemical gating modulation, which poses huge challenges for high-sensitive detection by OFETs.[200,201] In order to address the above-mentioned issues, Dacheng Wei's group[197] proposed a photo & chemical coupling gate effect for improving the detection sensitivity of small molecules by introducing additional photogate modulation. To obtain a photo-enhanced chemo-transistor, a layer of photoactive 2DCP (COFTP-py) was grown in situ on the graphene channels **(Figure 14f)**. Under light irradiation, photoelectrons generated *via* the COFTP-py are trapped at the interface of 2DCP and graphene, which further amplifies the electrical response. Due to the synergistic effect of photo-gate and chemical-gate, the COFTP-py/graphene chemo-transistors achieve enhanced sensitive detection of different small molecules with low chemical doping. For instance, the limit of detection (LoD) for methylglyoxal, a cellular metabolite implicated in conditions such as diabetes, cardiovascular disease, and hyperalgesia, is improved from ~ 10^{-16} M to ~ 10^{-19} M.[197]

In general, π-overlapping in ordered-packed molecular systems is considered to be one of the efficient charge transport modes.[24] Thus, the highly oriented 2DCP thin films provide unidirectional channels for improved charge migration along π-columns.[202] Dong Wang's group[192] synthesized the $COF_{TFPy\text{-}PPDA}$ film with high crystallinity and ordered π-arrays on single-layer graphene (SLG) *via* the condensation of 1,3,6,8-tetrakis(p-formyl phenyl)pyrene

(TFPy) and p-phenylenediamine (PPDA). The resulting film as the transport channel was further incorporated into a vertical organic field-effect transistor (VOFET), where the SLG serves as the source electrode and the deposited Au electrode as the drain electrode **(Figure 14g)**. Such graphene-based VFET architecture can combine the merit of graphene to achieve higher device performance, such as improved sheet resistance and regulated work function for carrier injection and current modulation.[203–205] As shown in **Figure 14h,** the prepared SLG/$COF_{TFPy\text{-}PPDA}$-VOFET displays an ambipolar charge carrier behavior under lower modulating voltages, which may be ascribed to work-function-tunable contact between SLG and $COF_{TFPy\text{-}PPDA}$ film and suitable injection barriers of charge carriers. The narrow band gap of $COF_{TFPy\text{-}PPDA}$ (1.61 eV) also facilitates charge carriers transport *via* lower the injection barrier. The resulting device achieves a high on/off ratio of 10^6 in the p-type and 10^5 in the n-type regime as well as the highest on-current density of 6.8 A cm^{-2} for hole transporting and 4.1 A cm^{-2} for electron delivering.[192]

4.2. Organic Electrochemical Transistors

The organic electrochemical transistors (OECTs) operate like a switch *via* gate voltage (input) that rules the drain current (output), similar to MOSFETs and OFETs.[206] OECTs are characterized by doping changes occurring over the entire volume of the channel, different from the thin interface regions of FETs, where the doping state is modulated by injected ions from electrolyte.[206] The coupling of ionic and electronic charges in the channel endows OECTs with superior transconductance, which enables effective regulation of drain current at low gate voltages, making OECTs efficient switches and powerful amplifiers.[207,208]

Typical organic semiconductor channels of OECTs are linear polymers with complex structures, like PEDOT: PSS, where the precise structure-function relationships and internal operating mechanisms can be elusive.[209] Semiconducting 2DCPs with well-defined molecular arrangements enable enhanced ionic and electronic transport as well as periodic skeletons allowing for precise and systematic designs, which presented a new avenue to study structure-performance relationships and thereby develop a novel class of channel materials. William R. Dichtel and Jonathan Rivnay's group[209] synthesized a semiconducting 2DCP thin film, TIIP, by imine condensation of N,N′-dibutyl-6,6′-diformylthienoisoindigo and 1,3,6,8-tetra(aminophenyl)pyrene, and then patterned the TIIP film at 10 μm resolution to construct the OECT (**Figure 15a**). Operating in an aqueous electrolyte, the resulting TIIP OECTs exhibit p-type (hole transport) operation (V_g, V_d < 0V) as well as clear linear and saturation regimes of transistor operation, as shown in the output and transfer curves in **Figure 15b-c**. The TIIP

OECTs share a peak transconductance (g_m) of 0.14 S cm^{-1}, a device-scale hole mobility of 0.05 cm^2 V^{-1} s^{-1} and a μC* figure of merit of 1.75 F cm^{-1} V^{-1} s^{-1}.[209] Mohamed Eddaoudi and Husam N. Alshareef's group[210] adopted 4,4′-azodianiline (Azo) and 1,3,5-triformylphloroglucinol (Tp) precursors to prepare azo (-N=N-) functionalized β-ketoenamine 2DCP (Tp-Azo) thin films, which were applied as the channel materials in OECT. The Tp-Azo based OECTs show a switching ratio of ~ 10^3 times, a low threshold voltage of 0.6 V, and a field-effect mobility of 0.53 cm^2 V^{-1} s^{-1}.

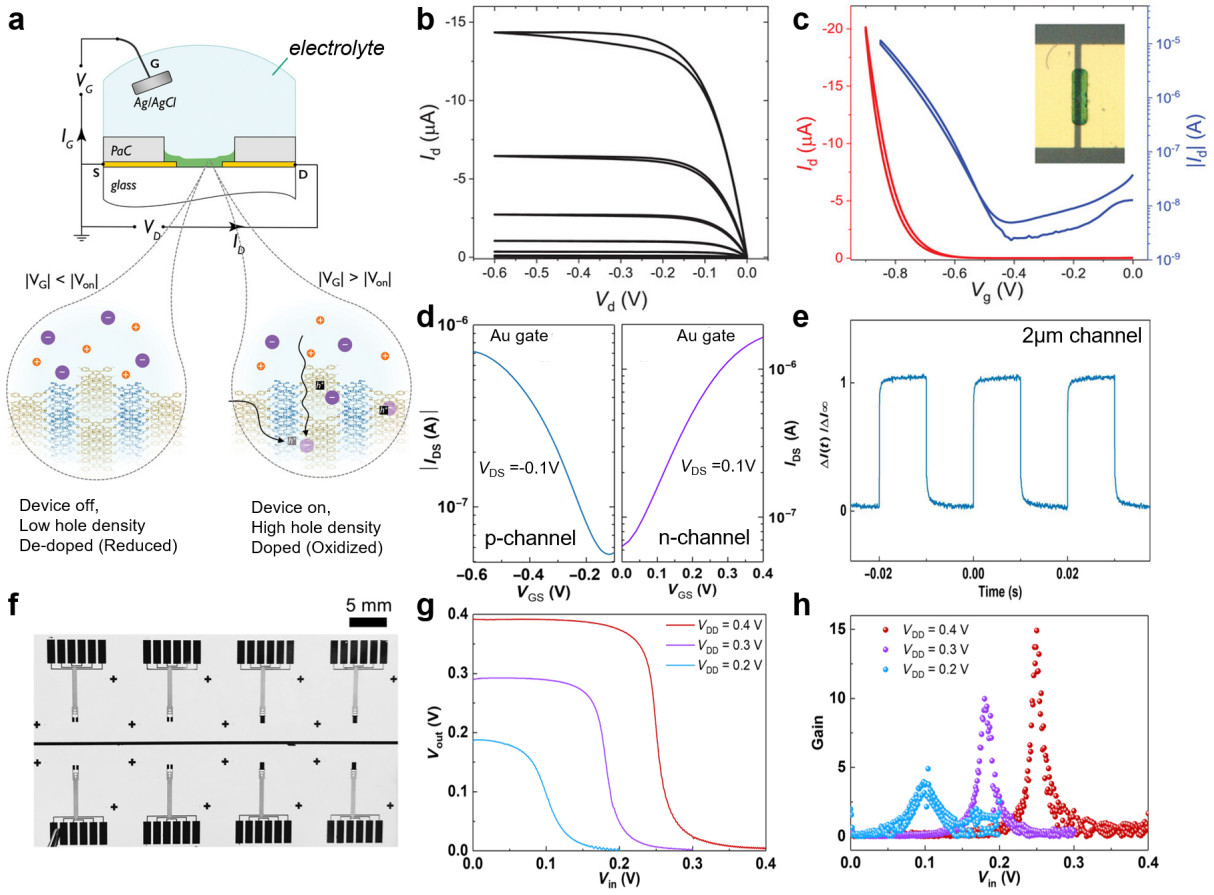

Figure 15. a) Schematic cross-section of the TIIP OFET and modulation of conductance state between de-doped and doped. b) The output curve of TIIP OECT (ΔV_g = 0.05 V, 0 V to − 0.8 V and V_d: 0 to −0.4 V at 0.02 V_d s^{-1}). c) The transfer curve of TIIP OECT (ΔV_g = 0.01 V, 0 V to −0.8 V at 0.02 V_g s^{-1} and V_d = −0.4 V). Inset: Optical microscopy image of the TIIP OECT.[209] Copyright 2022, Wiley-VCH. d) Transfer curves of the MOFECT in ambipolar operation. d) Transfer curves of the MOFECT in ambipolar operation. e) Transient response of the channel current of the MOFECT with a short channel (channel thickness: 50 nm). f) Photograph of MOFECT arrays (16 individual devices) on a large-area substrate. g) Voltage transfer characteristics of the complementary inverter at different working voltage V_{DD}. h)

Corresponding static gain ($\partial V_{out}/\partial V_{in}$) extracted from the voltage transfer curves. [211] Copyright 2023, Amer Assoc Advancement Science.

In addition, Feng Yan's group[211] prepared highly oriented 2DCP $Cu_3(HHTP)_2$ films based on a reproducible layer-by-layer growth method. The further obtained OECTs demonstrate a balanced ambipolar characteristic, wherein the conductivity of the $Cu_3(HHTP)_2$ channel can be modulated by cations or anions doping from the electrolyte (**Figure 15d**). Moreover, the vertical nanopores formed within the oriented $Cu_3(HHTP)_2$ films are favorable for ion transfer and diffusion, enabling the devices with a high volumetric capacitance C* of 67.8 F cm^{-3} and a fast response (10 μs) (**Figure 15e**).[211] In addition, owning to the convenient liquid-phase deposition preparation method, $Cu_3(HHTP)_2$-based transistor arrays have been manufactured in large areas (**Figure 15f**) and deploy in ultra-thin flexible circuits, including ambipolar inverters and complementary inverters. As presented by voltage transfer characteristics in **Figure 15g-h**, the resulting complementary inverter device exhibits an enhanced voltage gain from 5 to 15 V V^{-1}, when the working voltage V_{DD} increases from 0.2 to 0.4 V, demonstrating the great potential for low-voltage high-gain inverters. Furthermore, the high crystallinity and densely cross-linked nature of the $Cu_3(HHTP)_2$ films also efficiently restrict swelling, endowing devices with excellent operational stability, which is different from traditional OECTs based on linear polymers that require judicious control of swelling to balance efficient bulk ions doping and stable operation.[211]

4.3. Memristors

Memristors, envisioned by circuit theorist Leon Chua in 1971, exhibit variable but nonvolatile resistance states determined by the applied voltages or currents, which are considered to be the fourth basic circuit element in addition to resistance, capacitance, and inductance.[212] Moreover, memristors with simple structure, high speed, low power consumption, and compatibility with the complementary metal oxide semiconductor (CMOS) process, are promising basic devices for the realization of high-density storage as well as perceptual computing technologies.[213,214] In general, organic/polymer memristors are mainly divided into digital memristors and analog memristors. As resistive random-access memory, the former shares non-volatility, high density, fast speed, low power consumption, large ON/OFF ratio, high endurance, and long retention.[213] The latter operating like a logic component is capable of simulating fundamental synaptic functions of short-term/long-term plasticity, spike-timing dependent-plasticity, spike-rate dependent plasticity, and “learning experience” behaviors, which exhibits great potential

to construct artificial neural networks for neuromorphic computation.[213] 2DCP thin films are extremely suitable for manufacturing novel resistive memory devices in terms of their intrinsic flexibility, tunable electronic structures, well-defined pore channels, good uniformity, low density, and robust stability.[215] The 2DCP-based memristors typically have a metal-insulator-metal (MIM) device architecture that allows for resistive (conductive) switching between high-resistance states (HRS) and low-resistance states (LRS), displaying the characteristics of non-volatile memory.[215]

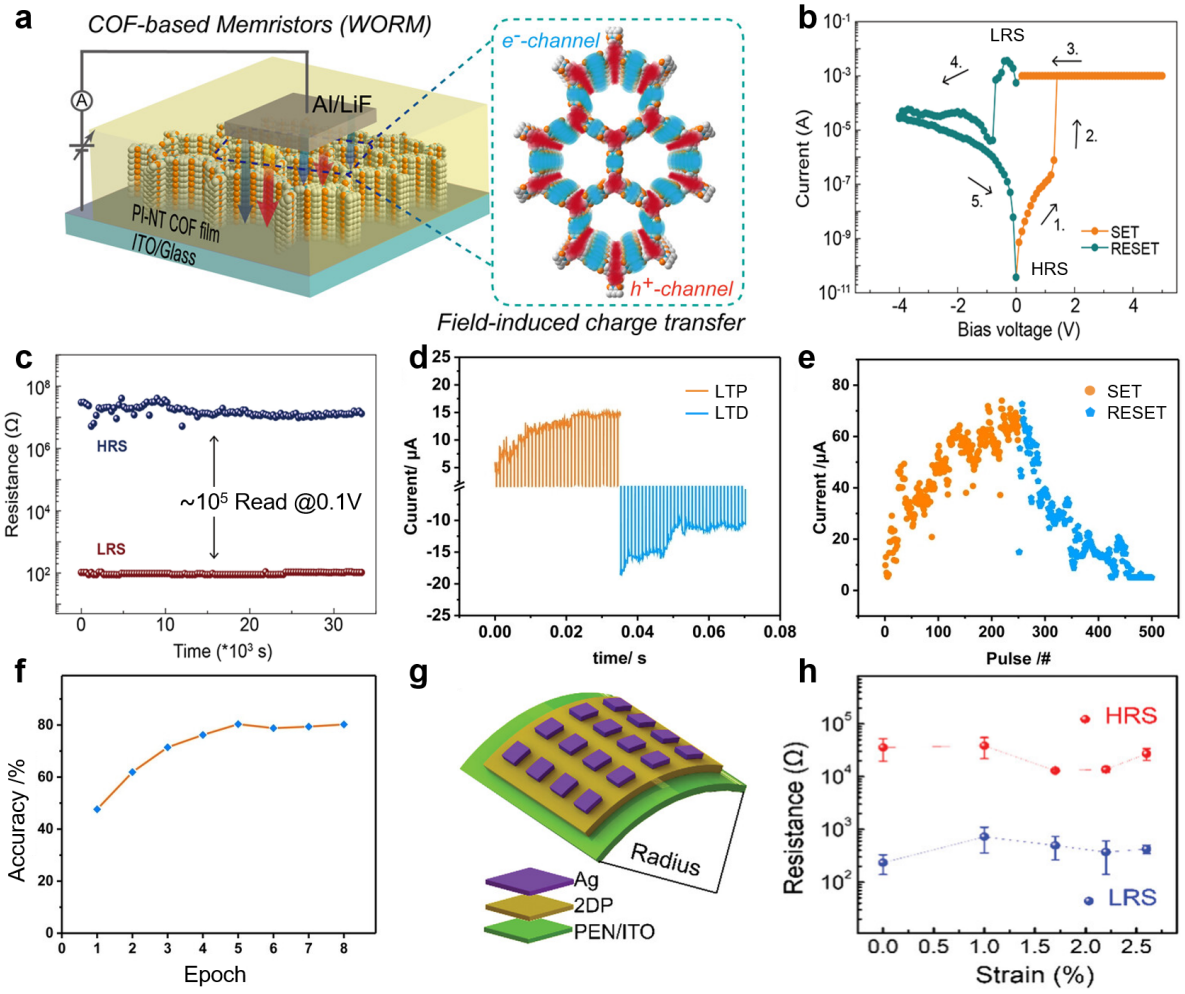

Figure 16. a) Schematic diagram of the resistive switching memory devices with the ITO/PI-NT COF film/LiF/Al configuration and the corresponding field-induced charge transfer mechanism.[216] Copyright 2020, American Chemical Society. b) Current-voltage curves of the COF-TT-BT (100 nm) memristor. SET progress (1-3): sweeps from 0 to 5 V and RESET progress (4-5): sweeps from 0 to - 4 V. c) Retention time of the COF-TT-BT (100 nm) memristor under reversible switching between "on" and "off" states at a constant operating voltage of 0.1 V.[217] Copyright 2021, Wiley-VCH. d) Long-term potentiation and depression behavior of the Al/COF-Azu/ITO device. e) Typical analog behavior of a memristor cell in the

array under identical pulse trains during SET and RESET processes. f) Recognition accuracy as a function of the training epochs.[167] Copyright 2022, Wiley-VCH. g) Scheme diagram of the flexible memory device arrays based on the SL-2DP$_{TAPB+TPOC}$ film. h) Distribution of HRS and LRS with constant bending rate and increasing strain (the circle represents the mean value and the error bar represents the standard deviation).[61] Copyright 2022, Wiley-VCH.

The D-A systems promote electric field-induced charge carrier separation and transfer, which contributes to endowing 2DCPs with intrinsic switching characteristics. Yi Liu and Dong Wang's group[216] reported a D-A 2DCP (PI-NT) thin film with high crystallinity, excellent orientation, tunable thickness, and low surface roughness, synthesized by electron-donor (triphenylamine unit) and acceptor (naphthalene diimide unit). As shown in **Figure 16a**, the PI-NT-based two-terminal sandwich-like device with depositing Al electrodes and LiF interlayer behaves the typically nonvolatile write-once-read-many-time (WORM) memory property for both the positive and negative scans with threshold voltages of + 2.30 and - 2.64 V, respectively. The device also exhibits a high ON/OFF current ratio (> 10^6 for the positive scan and 10^4-10^6 for the negative scan) with high stability and long-term retention time. The resistive switching behaviors could be attributed to a charge-transfer mechanism upon an external electric field, which are further improved *via* effective intramolecular charge transfer and stable charge separation states in the D-A architecture. In addition, Yu Gui's group[217] applied electron-deficient triazine and electron-rich thiophene to construct imine-linked 2DCP (COF-TT-BT) with D-A structure for high-performance and reliable rewritable memristors. The COF-TT-BT based memristors exhibit the bipolar I-V characteristics with a low driving voltage of 1.30 V (**Figure 16b**). Moreover, under the operating voltage of 0.1 V, the cycle period and retention time were 319 cycles and 3.3×10^4 s for COF-TT-BT-based memristors (**Figure 16c**). The superior performance and stability of COF-TT-BT-based memristor could be credited to the strong pull-push effect of D-A structure and high-quality films.

The D-A structure existed not only between linked building blocks but also within the single molecule. For instance, azulene (Azu) is a promising organic core with intrinsic redox activity owing to its intramolecular electron pull-push effect within the electron-withdrawing seven-membered and electron-rich five-membered sp^2 carbon rings, which is favorable for aromatic delocalization and charge transfer.[218–220] Yu Chen's group[167] performed a liquid-liquid interface polymerization strategy to prepare the Azu-based 2DCP thin film, COF-Azu, for high-performance memristors. The obtained Al/COF-Azu/ITO memristor shares typical non-volatile resistive switching properties with a low switch-on voltage of - 0.50 V and a long retention time

of 3×10^4 s. Moreover, the fabricated memristor shows a gradual increase (or decrease) in current over time under a pulse train with a pulse amplitude of 0.1 V (or, -0.1 V), a pulse width of 50 ms, and a pulse interval of 20 ms, which is quite similar to the long-term potentiation/plasticity (LTP) and depression (LTD) (**Figure 16d**).[167] When the same pulse trains are applied to the memristor cell in the array (pulse width: 20 ms), typical analog behaviors are observed during the SET and RESET processes, as presented in **Figure 16e**. Furthermore, a convolutional neural network related to the unique memristive properties was constructed for image recognition. After 8 epochs of training, the recognition accuracy of 80% is obtained (**Figure 16f**).[167]

2DCP thin films hold huge potential in memristors, however, the rigid skeleton readily results in the brittleness and the porous structure leads to the metal penetration of the top electrode, which impairs the enhancement of 2DCP-based memristor performance.[61] The covalent incorporation of long alkyl chains into the backbone is an important approach to address the above issues. Wenping Hu's group[61] adopted terephthalaldehyde with different length of alkoxy chains to synthesize ultrathin (single monomer thickness) 2DCPs ($2DP_{TAPB+TPOC}$) *via* the Langmuir-Blodgett technique. The research indicates that the longer alkoxy chains contribute to forming highly crystalline films and effectively blocking metal penetration during the thermal evaporation electrode deposition process. The resulting Ag/$2DP_{TAPB+TPOC}$/ITO devices exhibit a low variability ($\sigma Vset = 0.14$), high reliability (> 300 consecutive measurements), outstanding stability (> 10^5 s) and an ultra-low operating voltage (0.6 V). Moreover, the ultrathin memristor possesses distinguished bending endurance withstanding a bending strain of up to 2.6% without performance degradation (**Figure 16g-h**).[61]

4.4. Electrochromism

Electrochromism (EC) refers to the reversible spectrum and color change of materials in response to applied electric potential, which is caused by alteration in the redox states of the electroactive functionalities.[221,222] Ideal electrochromic materials feature high coloring efficiency, fast switch, and high contrast ratio over multiple cycles, which show great application potential in smart windows, optical displays, and molecular imaging.[223–225] According to the number of variable redox states, electrochromic materials can be divided into type I and type II, the former exhibits switching between two colored states, including colored and bleached states, and the latter can realize more than two redox states.[226] Apart from classical inorganic-based electrochromic materials such as WO_3,[227,228] considerable attention focuses increasingly on electroactive organic materials due to their high coloration efficiencies

and tunability. Recently, 2DCPs with tunable redox functionalities, highly ordered structures, and large specific surface areas are considered as promising electrochromic materials. The ordered micro- or mesopores channels in 2DCPs facilitate the transportation of electrolytes and inter-layer delocalization of electrons, which enables very fast and efficient electrochromic switching. Moreover, the 2DCPs also offer robust electrochemical stability and large π-conjugated backbones that facilitate charge transfer.[33]

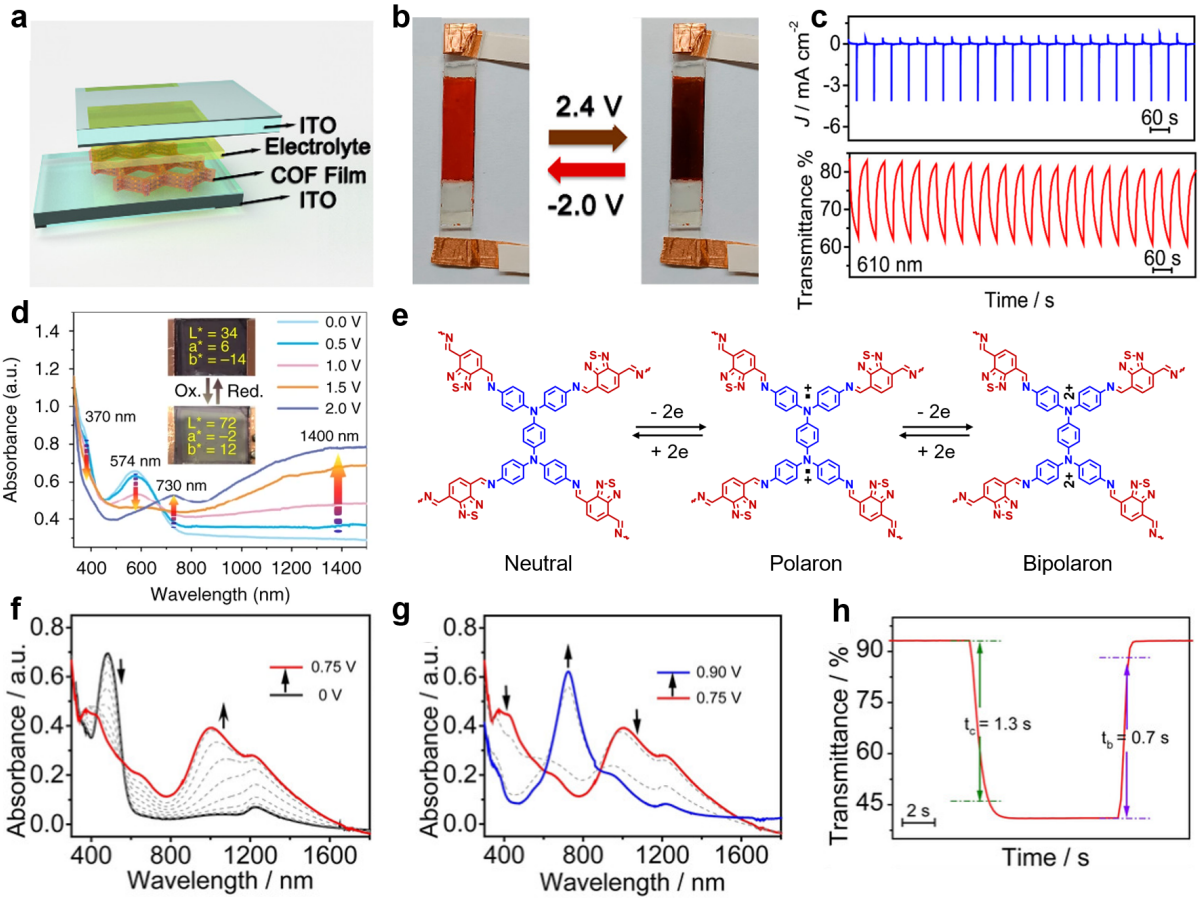

Figure 17. a) The architecture of $COF_{3PA\text{-}TT}$ EC devices. b) Color switching of the $COF_{3PA\text{-}TT}$ EC devices between -2 and +2.4 V. c) Current consumption and transmittance changes monitored at 610 nm during 15 cycles of EC switching of $COF_{3PA\text{-}TT}$ electrochromic devices.[229] Copyright 2019, American Chemical Society. d) Absorption spectra of EC-COF-1 film with different applied potential. e) Possible reversible electron transfer in neutral, polaron, and bi-polaron forms of EC-COF-1 under oxidative doping.[230] Copyright 2020, Nature Publishing Group. f, g) Absorption spectral changes of $COF_{TPDA\text{-}PDA}$ film recorded at different potentials. h) Response time (1.3 s for coloring and 0.7 s for bleaching) of $COF_{TPDA\text{-}PDA}$ film at 1050 nm.[231] Copyright 2021, Wiley-VCH.

The electrochromic properties of COF films were firstly studied *via* Wang Dong's group in 2019.[229] The well-oriented $COF_{3PA\text{-}TT}$ film was directly grown on the ITO surface through the liquid/solid interface solvothermal method, by imine condensation of tris(4-aminophenyl)amine (TAPA) and thieno[3,2-b]thiophene-2,5-dicarbaldehyde (TTDA). The electron-rich triphenylamine moieties as electroactive units easily realize reversible redox, which contributes to charge transfer and the electrochromic phenomenon. Furthermore, the fully conjugated bridge linker of thiophene is also beneficial to charge transport for improved conductivity of $COF_{3PA\text{-}TT}$ film. The $COF_{3PA\text{-}TT}$ based EC device was assembled as a sandwich structure, where the $COF_{3PA\text{-}TT}$ EC electrode was the working electrode, another blank ITO glass as the counter electrode, and $LiClO_4$-based polymer gel injected into the gap between the two electrodes was quasi-solid electrolyte (**Figure 17a**). This resulting device exhibits reversible color switching from deep red to dark brown under applied switching potential ranging from – 2 V to + 2.4 V and robust stability without performance degradation after 15 cycles of potential switching (**Figure 17b-c**). This work provides evidence for the huge potential of 2DCPs for electrochromic applications and promotes the exploration of 2DCPs as stimuli-responsive materials.[229]

For many EC products, such as smart windows, and display devices, dark-to-transmissive switches are highly desirable. However, realizing the dark state demands the materials with broadband absorption across the whole visible region, which remains a huge challenge.[222,232] Constructing 2DCPs with D-A structures is expected to achieve the desired valence and/or conduction band positions to tailor EC properties for the dark state.[233] Qichun Zhang's group[230] synthesized an extended delocalized π-electron layered dark purple D-A EC-COF-1 by covalently linking the donor of (p-aminophenyl)-p-benzenediamine (TPBD) with the acceptor benzothiadiazole. The EC-COF-1 film is further processed into the quasi-solid-state device with a sandwiched configuration. When the applied external potential gradually increases, the absorption bands at 370 and 574 nm proportionally decreases as well as a new absorption band arises in the near-infrared (NIR) region, which indicate the formation of radical cations (polarons) and further evolving into dications (bipolarons) at higher bias voltages (**Figure 17d-e**).[230] The D-A EC-COF-1 with two-band absorption (deep absorption, *i.e.,* blue-purple) in the visible region (neutral state) can transformed into transparent under an electric field, which is different from most EC materials with color changes from light (neutral state) to dark (oxidized state). Thus, the D-A design strategy shows huge potential for developing dark to transparent electrochromic switching materials due to reduced optical gap and tunable redox energy level.[230]

In addition to triphenylamine as the electrochromic active material, thienoisoindigo with excellent photoelectric activity is also an ideal organic unit. Thomas Bein's group[234] applied modified thienoisoindigo building blocks to develop a class of highly efficient, fast-switching, and stable electrochromic 2DCP thin films. The highly electron-deficient thienoisoindigo (TII) unit was combined with electron-rich thienothiophene (TT) or naphthalene (N) donors to construct donor-acceptor-donor (D-A-D) electronic configurations for maximizing the electrochromic response across the visible and NIR spectral regions. Such designs are conductive to obtain a narrower band gap with a wider absorption range as well as the effective charge transfer and π-π* transitions to render sensitive electrochromic response. The well-established pyrene as the tetradentate counterpart was also integrated into the framework for high crystalline and stability due to its strong electrostatic interactions enforcing slip-stacked arrangements. The resulting Py-ttTII COF-based device shows an electrochromic coloration efficiency of 858 $cm^2\ C^{-1}$ at 880 nm and retains >95% of its initial electrochromic response after 100 oxidation/reduction cycles, which also possesses fast response times below 0.4 s for the oxidation (coloration) and around 0.2 s for the reduction (bleaching). The building block design and D-A-D electronic structure are key factors in achieving such high-performance electrochromism, including high coloration efficiency and fast switching.[234]

Developing novel electrochromic materials with stable multiple-color states, fast response time, and long retention time is a major breakthrough and demand in the field of electrochromism. A Kagome 2DCP ($COF_{TPDA\text{-}PDA}$) film[231] was prepared by *N, N, N′,N′*-tetrakis(4-aminophenyl)-1,4-benzenediamine (TPDA) and terephthalaldehyde (PDA). Due to the introduction of TPDA with two adjacent triarylamines species, the $COF_{TPDA\text{-}PDA}$ film exhibits high absorption spectra changes in the NIR region as well as three reversible color states (plum, grey, and light blue) with the two-step oxidation (+ 0.75 V and + 0.90 V) (**Figure 17f-g**). The $COF_{TPDA\text{-}PDA}$ film-based device share a coloration efficiency of 320 $cm^2\ C^{-1}$ at 1050 nm and a sub-second response time (1.3 s for coloring and 0.7 s for bleaching at 1050 nm) (**Figure 17h**). The Extended π electron delocalization in the 2D plane and π-π interlayer stacking structure of $COF_{TPDA\text{-}PDA}$ facilitate the EC device with a long retention time over 2 h after releasing + 0.75 V applied potential, which indicates the excellent stability of $COF_{TPDA\text{-}PDA}$ in NIR electrochromism.[231] Moreover, the viologen-immobilized 2D polymer (V2DP) thin film, synthesized from Schiff-base polycondensation between 1,1′-bis(4-aminophenyl)-[4,4′-bipyridine]-1,1′-diium chloride and 2,4,6-trihydroxybenzene-1,3,5-tricarbaldehyde, exhibited three color states including its initial state (yellow), one-electron reduced state (violet), and oxidized state (yellow).[235] The high utilization of redox-active viologen moieties and effective Li^+ ion diffusion/transport

endow the prepared EC devices with a rapid switching speed (coloration, 2.8 s; bleaching, 1.2 s), and a high CE (989 cm^2 C^{-1}), and low energy consumption (21.1 μW cm^{-2}).[235]

4.5. Chemiresistor

Chemiresistors operate as resistive chemical sensors, which enable electrical resistance variation in response to changes in the surrounding chemical environment.[236] Chemiresistive materials interact with the analyte including humidity, reducing or oxidizing gases, based on the effect of hydrogen bonding, covalent bonding, or molecular recognition, altering the charge density and thus affecting the conductivity as measurable variations. Chemiresistive sensors offer the advantages of low cost, compact size, and real-time response, which are widely applied in rapid and sensitive gas detection.[236] The 2DCP thin films exhibit huge potential for developing high-performance chemiresistive sensors due to their tunable structure, large surface area, robust stability, and diversified functionalization.[237] Customizable skeletons enable the introduction of active functional groups or modified organic units, thereby achieving selective responses to specific gas molecules and concurrently optimizing the sensor performance. Moreover, the substantial surface area facilitates gas molecule adsorption and exposes abundant active sites for improving sensitivity. Furthermore, the robust stability widens the application in diverse demanding environments and service life.[238]

Human metabolism is rich in information, which can shed light on the internal health of the human body. Humidity, as a biological signal, exhibits great significance for early disease diagnosis, such as tachypnea, sleep apnea, and asthma.[242,243] However, ultra-sensitive quantitative detection of human metabolite moisture in real-time remains a huge challenge. Zhi Yang's group[239] reported the imine-linked 2DCP ($COF_{TAPB\text{-}DHTA}$) films synthesized by 1,3,5-tris(4-aminophenyl)benzene (TAPB) and 2,5-dihydroxyterephthaldehyde (DHTA) for constructing ultra-sensitive humidity sensors (**Figure 18a**). The TAPB unit as the electron-rich structure promotes charge exchange between water molecules while the DHTA unit features strong intramolecular O-H···N=C hydrogen bonding to safeguard the imine bond from potential nucleophilic attacks. The $COF_{TAPB\text{-}DHTA}$ film-based humidity sensor exhibits a 390-fold increase in a humidity range from 13 to 98% and a respiration frequency floating signal with a response/recovery time of 0.4/1 second (**Figure 18b**). Notably, the intrinsic sensing mechanism of hydrogen bonding caused reversible β-ketoenamine tautomerism of DHTA units, which results in intrinsic resistance variations with high sensitivity and fast response.[244] Moreover, the humidity sensor also shows outstanding humidity monitoring stability with a negligible change in the current output characteristic curve even after 12 cycles (**Figure 18c**).[239] The

adsorption and desorption of water molecules will induce a reversible deformation of borate-linked 2DCP layers, concomitantly establishing novel conductive pathways through π-π stacking, which affects the conductivity of the material to further reflect humidity information. Based on the intermolecular reconfiguration mechanism, Keqiang Chen's group[240] fabricated an efficient flexible humidity sensor with COF-5 film, which exhibited ultrahigh sensitivity, fast response, and bending tolerance. The COF-5 based sensor behaves a resistance change in 4 orders of magnitude with a remarkable linear relation between the log function of resistance and relative humidity (RH) in 11 % - 98 % RH range under 180° bending (**Figure 18d**). The sensor even shows a similar shape to the sensing response curve after being bent for 1500 cycles, indicating a superior endurance of the continuous bending.[240]

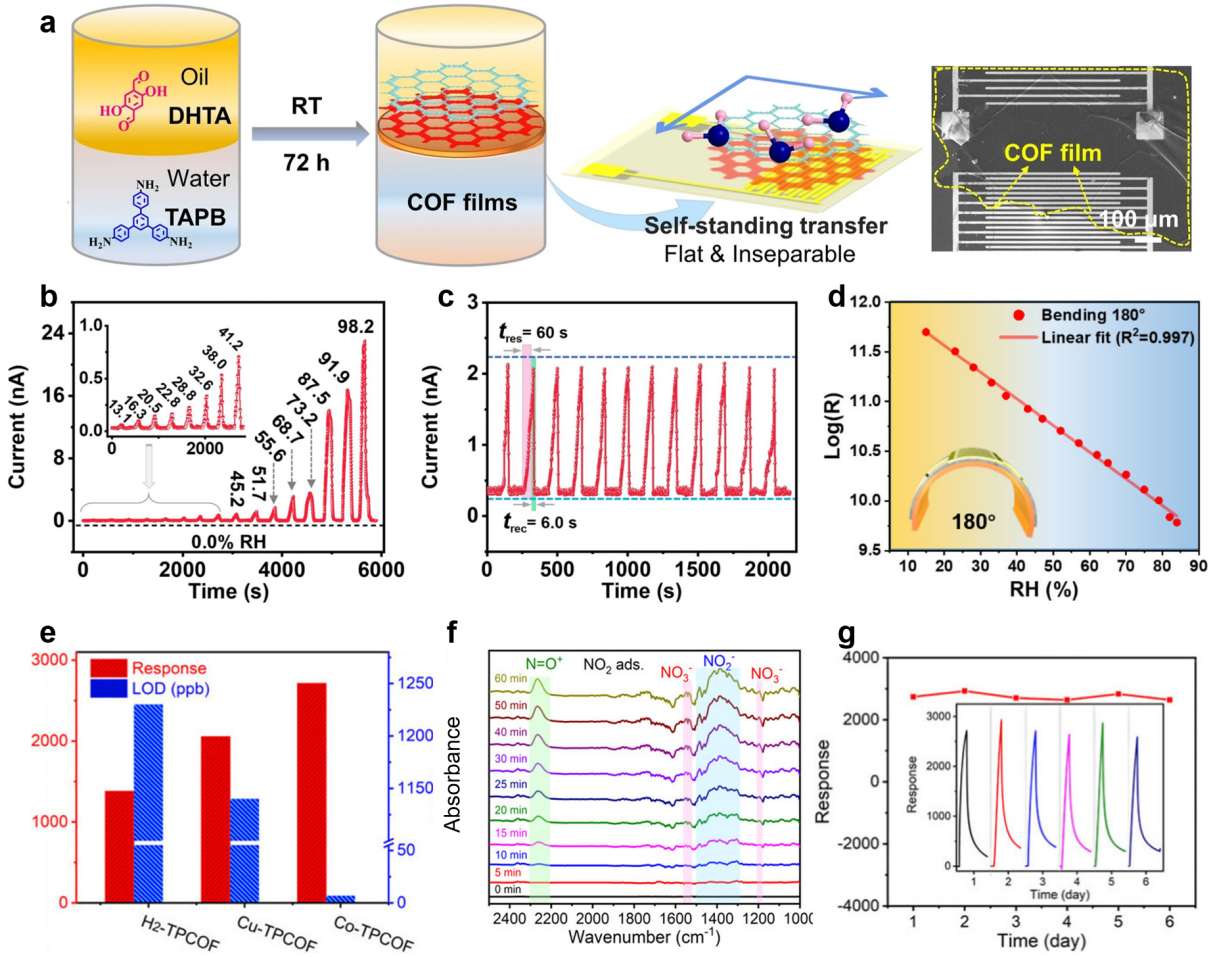

Figure 18. a) Schematic diagram of the fabrication process of the humidity sensor through transferring the $COF_{TAPB\text{-}DHTA}$-thin film synthesized at the liquid-liquid interface. b) Dynamic response characteristic curve in different humidity and c) response and recovery curves for $COF_{TAPB\text{-}DHTA}$-thin film-based humidity sensor.[239] Copyright 2023, Shanghai Jiao Tong Univ Press. d) Bending test of COF-5 humidity sensor at 180°.[240] Copyright 2023, Wiley-VCH. e)

The enhanced sensing performances of response and LoD column of porphyrin-based 2DCP (M-TPCOF, M = H_2, Cu and Co). f) In situ infrared spectra of Co-TPCOF during NO_2 adsorption. g) Gas detection stability measurements of Co-TPCOF to 100 ppm NO_2 up to 6 days.[241] Copyright 2022, Wiley-VCH.

Phthalocyanines and porphyrins with extended π-conjugated systems, excellent redox activity, functional versatility, and robust stability, display promising potential to detect a wide variety of gases, including volatile organic compounds, toxic gases, and environmental pollutants.[147] The predesigned phthalocyanine or porphyrin have modifiable sites for post-metallization to flexibly modulate sensing performance. For instance, the porphyrin-based 2DCP (Co-TPCOF) after metallization exhibits enhanced sensing performances toward NO_2, including ≈ 2 times higher sensitivity, ≈ 180 times lower LoD, ≈ 1.5 times faster response than pristine H_2-TPCOF (**Figure 18e**).[241] DFT calculations reveal that the adsorption energy of NO_2 effectively is improved from - 0.27 eV to - 1.52 eV after introducing metallic cobalt into the porphyrin part. Moreover, as demonstrated in FT-IR spectroscopy of the NO_2 adsorption on Co-TPCOF (**Figure 18f**), the gradually strengthened signals of 2500 to 1000 cm^{-1} indicate the formation of intermediate nitrite species, where the peak at 1398-1353 cm^{-1} is attributed to Co-NO_2 nitro compounds, which further reveals the cobalt operated as the NO_2 induction active site.[245] Moreover, the Co-TPCOF exhibits long-term stability with minor sensor performance changes up to 6 days (**Figure 18g**). In addition, the phthalocyanine nickel(II)-based 2DCP (COF-DC-8)[147] also exhibits superb responses to various volatile gases with parts-per-billion (ppb) LoD (for NH_3 = 70 ppb, for H_2S = 204 ppb, for NO = 5 ppb, and for NO_2 = 16 ppb based on 1.5 min exposure). Moreover, the metallophthalocyanine-based 2DCP (NiPc-CoTAA)[143] with cobalt(II) tetraaza[14]annulene linkages also shows outstanding selectivity for different volatile gases, which behaves positive responses towards NO_2 and NO and a negative response when exposed to the electron-donating NH_3 and H_2S atmosphere.

4.6. Photodetector

Photodetector is a class of photosensitive semiconductor device that can convert photoirradiation into an electrical signal, which shares broad application potential in many fields, including optical communication, spectroscopy, imaging, optoelectronics.[246] With the continuous growth of application scale and diversity, the demand for high-performance photodetectors in terms of faster speed, higher sensitivity, and wider wavelength range, is becoming prominent. Besides graphene and other 2D materials, such as transition metal

dichalcogenides, 2DCPs featuring expanded conjugation, tunable electronic structure, and wide light absorption range, have been widely applied as the active layer for optoelectronic applications.[247,248]

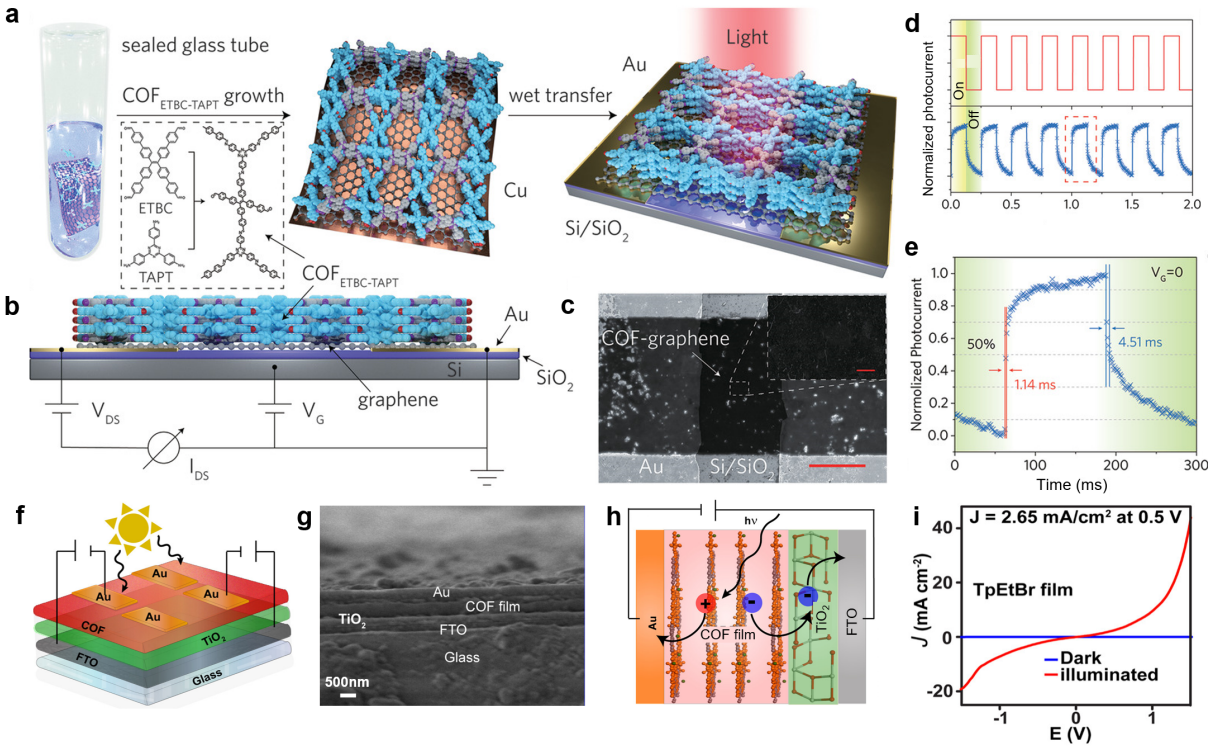

Figure 19. a) Schematic diagram of the preparation of $COF_{ETBC-TAPT}$-graphene photodetector, which was fabricated by assembling a $COF_{ETBC-TAPT}$-graphene heterostructure with Au electrodes on a Si/SiO_2 substrate. b) Side schematic view of the prepared $COF_{ETBC–TAPT}$-graphene photodetector with measurement setup. c) The SEM image of a fabricated device. Inset: The enlarged SEM image of the $COF_{ETBC-TAPT}$-graphene area. d) The photo-switching performance under alternating dark and light illumination (VG = 0, VDS = 1 V, λ = 473 nm). e) An enlarged view of the normalized photocurrent dynamics during one cycle of light modulation.[249] Copyright 2020, Wiley-VCH. f) Schematic representation of the photodetectors with a TiO_2/COF-film architecture. g) Cross-section SEM images of the TpEtBr COF thin film-based device. h) Schematic diagram of the mechanism of photocarrier generation in the COF thin film sandwiched between the Au and FTO electrodes. i) J-V curves of TpEtBr film are observed in the dark (blue) and under visible light illumination (red).[57] Copyright 2023 American Chemical Society.

Many 2DCPs are most sensitive to the blue and green spectral regions with appreciable quantum efficiency of the visible spectrum due to limited aromatic subunits.[166,250] Extension of the

absorption capabilities into the red and NIR spectral regions is highly desirable to widen the detection range. One effective approach is to combine electron-rich and deficient moieties for improving π electron delocalization to shift the absorption onset well into the NIR regime.[105] For instance, the incorporation of D-A type isoindigo- and thienoisoindigo-based building blocks generate the NIR-absorbing 2DCP (Py-tTll COF).[251] The Py-tTll COF further forms a heterojunction with the fullerene, as the photoactive component, to construct a ultraviolet (UV) to NIR responsive photodetector. The spectral response of the resulting photodetector is reversibly switchable between blue- and red-sensitive, and green- and NIR-responsive by changing the bias voltage, which could trigger potential applications in information technology or spectral imaging.[251] Recently, Yanqing Lu's group[249] designed a photosensitive 2DCP ($COF_{ETBC–TAPT}$) with highly ordered D-A topologies, which are in situ synthesized on graphene, ultimately forming the COF-graphene heterostructures (**Figure 19a**). The $COF_{ETBC–TAPT}$-graphene heterostructure was further employed to fabricate the photodetectors with Au electrodes on a Si/SiO_2 substrate (**Figure 19b-c**). The resulting photodetector exhibits stable on-off switching synchronized with illumination under a bias voltage of 1 V (**Figure 19d**) as well as a photoresponsivity of ≈ 3.2×10^7 A W^{-1} at 473 nm and a response time of ≈ 1.14 ms (**Figure 19e**). In addition to the heterojunction formed between COFs and fullerene or graphene, Rahul Banerjee's group[57] constructed a class of photodetectors with a TiO_2/COF-film architecture (**Figure 19f**). The COF thin film was deposited on the TiO_2-coated fluorine-doped tin oxide (FTO) surface, where FTO acts as a transparent bottom electrode. Subsequently, the Au thin layer was deposited on top of the COF thin film to serve as the top electrode (**Figure 19g**). After absorbing the visible range of photons, the COF layers are expected to generate excitons and free charge carriers, which can be extracted under applied bias. As shown in **Figure 19h**, the photogenerated free electrons will be collected at the FTO electrode (behaving as a cathode) due to the favorable alignment of the conduction band of TiO_2 and FTO with that of the COF thin film. Meanwhile, the photogenerated hole carriers migrate to the Au electrode (serving as an anode) since the work function of Au is comparable to the valance band energy of COF thin films. Four porous, crystalline, and partially orientated COF thin films (TpDPP, TpEtBt, TpTab, and TpTta) with different functional backbones including phenylphenanthridine, ionized phenylphenanthridine, triazine, and benzene nucleus are synthesized on TiO_2-coated FTO glass surfaces. Among all investigated COF thin films, the ionic TpEtBr COF exhibits the lowest band gap (2.26 eV) and longest excited-state lifetime (~8.52 ns), which are contribute to effective charge separation and migration. Accordingly, the photodetector device fabricated with the ionic TpEtBr COF thin film possesses a superior

photocurrent density (2.65 ± 0.24 mA cm^{-2}) and hole mobility (8.15 ± 0.64) $\times 10^{-3}$ cm^2 V^{-1} s^{-1} (**Figure 19i**).[57]

5. Conclusions and Outlooks

In this review, we present the key progress of 2DCPs regarding the interfacial synthesis methods, conductivity tuning strategies, and their applications in organic electronics fields. Firstly. we introduce the representative interfacial synthetic methods including solid-liquid, air-liquid, liquid-liquid, and vapor-solid interfaces, which laid the foundation of controllable synthesis of large area and highly ordered 2DCP thin films with enhanced electronic properties. Subsequently, the conductive mechanism of 2DCPs has been briefly summarized ranging from the effects of linkages and electroactive building blocks to the strategies for improving their conductivity. In addition, we emphasize that the 2DCPs with excellent electronic properties hold great potential in various organic thin-film electronics, including organic transistors, memristors, electrochromism, chemiresistors, and photodetectors. Despite many groundbreaking achievements in the fabrication and organic electronic functionalization of 2DCPs, some bottlenecks still limit their performance and practical applications.

In terms of synthesis, the interface-assisted polymerization methodology largely addressed the problems of large-area, thickness-controllable 2DCP thin films, but there are still significant challenges in controlling the morphology and structural order, such as obtaining high-quality single-crystal films.[37] Highly crystalline films with continuous uniform morphology allow for suppressing structure defects and grain boundaries are of great importance for high-performance devices. Furthermore, the preparation of well-ordered 2DCP thin films by interfacial polymerization is generally based on high-reversible reactions, such as Schiff base chemistry, but the resulting polar linkage (imine bonds) limits the conjugation expansion and carrier migration of the material.[42] The fully conjugated linkage, such as vinyl bonds, shows excellent π-electron delocalization for improved conductivity, but the corresponding linkage chemistry (e.g., Knoevenagel or aldol polycondensation) with poor reversibility and high reaction barrier hinders the construction of long-range ordered films.[41,252] Therefore, it is highly demanding to explore novel reaction systems including appropriate catalysts, rational-designed interface chemistry, and highly reactive building blocks to address the above issues. In addition, the interfacial synthesis mechanism for 2D polymerization ranging from nucleus growth, orientation, and structural defects, needs to be further studied via sophisticated instruments.

As for the structural design of 2DCP thin films, the intrinsic molecular design (*e.g.*, building block and linkage) and external components or architecture (*e.g.*, chemical doper and heterostructure) need to be considered. Usually, the 2DCP thin films suffer from modest charge transport in the skeleton, which precludes the fabrication of high-performance electronic devices. Apart from the effects of defects and grain boundaries, 2DCPs are often isolated as closed-shell organic species with limited charge carriers and weak electronic conductivities. Therefore, introducing building units and linkage containing abundant redox functional groups enables increasing the carrier density. The employment of large π conjugated and planar building blocks is beneficial to form periodic π columnar arrays, which serve as out-of-plane carrier transport paths. The alternating link electron-rich and deficient building blocks to form a D-A structure also facilitate in-plane carrier transport and improve the intrinsic electronic properties. Remarkably, the lattice topology fundamentally influences the electronic properties of 2DCPs. For example, the Kagome lattice could result in both Dirac cones and flat bands, potentially leading to some intriguing phenomena such as the anomalous Hall effect[180], surface superconductivity[181], or superfluid transport[182]. In addition, 2DCPs integrated with other materials allow for combining their advantages and overcoming the inherent defects. For example, constructing van der Waals heterojunctions with other 2D materials (h-BN, phosphorene, MXene, etc.) to improve carrier migration to meet practical applications and offer novel properties from several aspects like mechanical robustness and spin-orbit. Moreover, chemical doping with oxidants, acids, ionic liquids, linear conjugated polymer chains, etc. is a common approach to enhance electrical conductivity, which also contributes to unlocking the multifunction of 2DCPs.

Regarding the architecture of 2DCP thin film devices, appropriate structure design contributes to exploiting the anisotropic electron transport properties of the films. For instance, the performance of devices with horizontal structures is greatly influenced by their in-plane conductivity, due to the vertical orientation grown of 2DCPs on the substrate. By fabricating vertical thin-films devices, it is possible to develop high-performance devices with efficient carrier transport in the out-of-plane direction of 2DCPs. In addition, the introduction of ingenious structure designs, such as the air gap[253], to the device can effectively improve the device performance. Therefore, the uniform combination of efficient synthesis strategies, ingenious molecular structure design, and device architectures pave the way for high-performance 2DCP-based organic devices in many research and application fields.

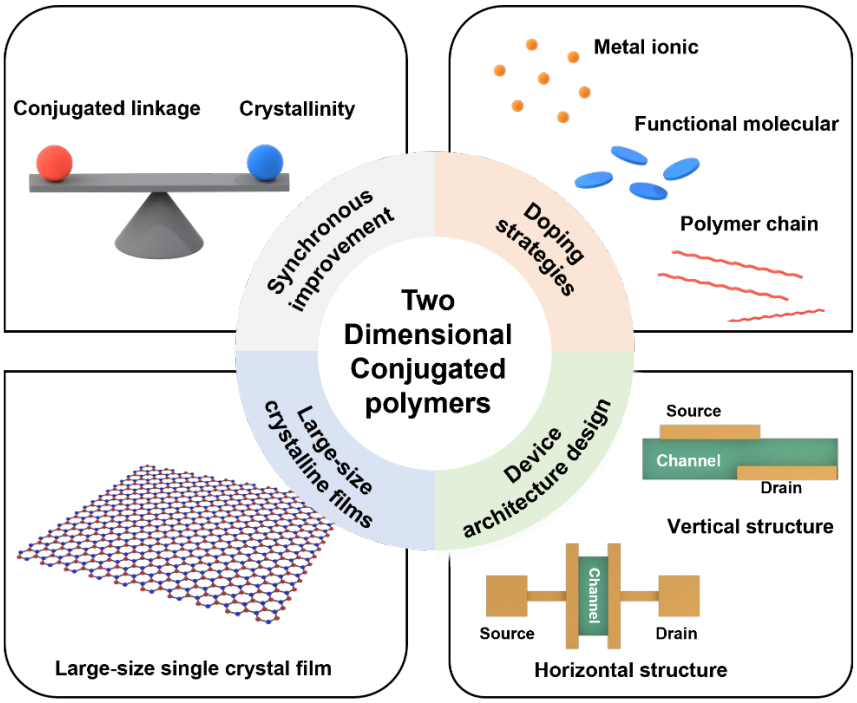

Figure 20. Plausible strategies to achieve high-performance 2DCP-based organic electronics.

Acknowledgements

This work was supported by the National Natural Science Foundation of China (Grant No. 52322316), the Zhejiang Provincial Natural Science Foundation of China (Grant No. LR21E030001), the Leading Innovative and Entrepreneur Team Introduction Program of Zhejiang (Grant No. 2021R01005), the Key Research and Development Program of Ningbo (Grant No. 2022ZDYF020023), and the Public Welfare Science and Technology Projects of Ningbo (Grant No. 2023S080).

Conflict of Interest

The authors declare no conflict of interest.

Received: ((will be filled in by the editorial staff))
Revised: ((will be filled in by the editorial staff))
Published online: ((will be filled in by the editorial staff))

References

[1] A. J. Heeger, *Rev. Mod. Phys.* **2001**, *73*, 681.
[2] N. K, C. Sekhar Rout, *RSC Adv.* **2021**, *11*, 5659.
[3] S. Wang, Q. Sun, O. Gröning, R. Widmer, C. A. Pignedoli, L. Cai, X. Yu, B. Yuan, C. Li, H. Ju, J. Zhu, P. Ruffieux, R. Fasel, W. Xu, *Nat. Chem.* **2019**, *11*, 924.

[4] C. K. Chiang, C. R. Fincher, Y. W. Park, A. J. Heeger, H. Shirakawa, E. J. Louis, S. C. Gau, A. G. MacDiarmid, *Phys. Rev. Lett.* **1977**, *39*, 1098.
[5] M. Xue, Y. Wang, X. Wang, X. Huang, J. Ji, *Adv. Mater.* **2015**, *27*, 5923.
[6] M. A. Darabi, A. Khosrozadeh, R. Mbeleck, Y. Liu, Q. Chang, J. Jiang, J. Cai, Q. Wang, G. Luo, M. Xing, *Adv. Mater.* **2017**, *29*, 1700533.
[7] B. Le Ouay, M. Boudot, T. Kitao, T. Yanagida, S. Kitagawa, T. Uemura, *J. Am. Chem. Soc.* **2016**, *138*, 10088.
[8] Y. Van De Burgt, E. Lubberman, E. J. Fuller, S. T. Keene, G. C. Faria, S. Agarwal, M. J. Marinella, A. Alec Talin, A. Salleo, *Nature Mater* **2017**, *16*, 414.
[9] L. Huang, Z. Wang, J. Chen, B. Wang, Y. Chen, W. Huang, L. Chi, T. J. Marks, A. Facchetti, *Adv. Mater.* **2021**, *33*, 2007041.
[10] T. Zhang, H. Qi, Z. Liao, Y. D. Horev, L. A. Panes-Ruiz, P. S. Petkov, Z. Zhang, R. Shivhare, P. Zhang, K. Liu, V. Bezugly, S. Liu, Z. Zheng, S. Mannsfeld, T. Heine, G. Cuniberti, H. Haick, E. Zschech, U. Kaiser, R. Dong, X. Feng, *Nat Commun* **2019**, *10*, 4225.
[11] K. Lee, S. Cho, S. Heum Park, A. J. Heeger, C.-W. Lee, S.-H. Lee, *Nature* **2006**, *441*, 65.
[12] N.-R. Chiou, C. Lu, J. Guan, L. J. Lee, A. J. Epstein, *Nat. Nanotechnol.* **2007**, *2*, 354.
[13] S. Fratini, M. Nikolka, A. Salleo, G. Schweicher, H. Sirringhaus, *Nat. Mater.* **2020**, *19*, 491.
[14] J. Y. Oh, S. Rondeau-Gagné, Y.-C. Chiu, A. Chortos, F. Lissel, G.-J. N. Wang, B. C. Schroeder, T. Kurosawa, J. Lopez, T. Katsumata, J. Xu, C. Zhu, X. Gu, W.-G. Bae, Y. Kim, L. Jin, J. W. Chung, J. B.-H. Tok, Z. Bao, *Nature* **2016**, *539*, 411.
[15] S. Wang, J. Xu, W. Wang, G.-J. N. Wang, R. Rastak, F. Molina-Lopez, J. W. Chung, S. Niu, V. R. Feig, J. Lopez, T. Lei, S.-K. Kwon, Y. Kim, A. M. Foudeh, A. Ehrlich, A. Gasperini, Y. Yun, B. Murmann, J. B.-H. Tok, Z. Bao, *Nature* **2018**, *555*, 83.
[16] H. He, J. Zhu, N. J. Tao, L. A. Nagahara, I. Amlani, R. Tsui, *J. Am. Chem. Soc.* **2001**, *123*, 7730.
[17] T. Xu, E. C. Walter, A. Agrawal, C. Bohn, J. Velmurugan, W. Zhu, H. J. Lezec, A. A. Talin, *Nat Commun* **2016**, *7*, 10479.
[18] M. Xue, F. Li, D. Chen, Z. Yang, X. Wang, J. Ji, *Adv. Mater.* **2016**, *28*, 8265.
[19] J. Janata, M. Josowicz, *Nat. Mater.* **2003**, *2*, 19.
[20] A. Khasbaatar, Z. Xu, J.-H. Lee, G. Campillo-Alvarado, C. Hwang, B. N. Onusaitis, Y. Diao, *Chem. Rev.* **2023**, *123*, 8395.
[21] G. Itskos, A. Othonos, T. Rauch, S. F. Tedde, O. Hayden, M. V. Kovalenko, W. Heiss, S. A. Choulis, *Adv. Energy Mater.* **2011**, *1*, 802.
[22] D. Yuan, W. Liu, X. Zhu, *Chem. Soc. Rev.* **2023**, *52*, 3842.
[23] K. Kang, S. Watanabe, K. Broch, A. Sepe, A. Brown, I. Nasrallah, M. Nikolka, Z. Fei, M. Heeney, D. Matsumoto, K. Marumoto, H. Tanaka, S. Kuroda, H. Sirringhaus, *Nat. Mater.* **2016**, *15*, 896.
[24] C. Wang, H. Dong, W. Hu, Y. Liu, D. Zhu, *Chem. Rev.* **2012**, *112*, 2208.
[25] H. Sirringhaus, P. J. Brown, R. H. Friend, M. M. Nielsen, K. Bechgaard, B. M. W. Langeveld-Voss, A. J. H. Spiering, R. a. J. Janssen, E. W. Meijer, P. Herwig, D. M. de Leeuw, *Nature* **1999**, *401*, 685.
[26] V. Coropceanu, J. Cornil, D. A. da Silva Filho, Y. Olivier, R. Silbey, J.-L. Brédas, *Chem. Rev.* **2007**, *107*, 926.
[27] M. Wang, S. Fu, P. Petkov, Y. Fu, Z. Zhang, Y. Liu, J. Ma, G. Chen, S. M. Gali, L. Gao, Y. Lu, S. Paasch, H. Zhong, H.-P. Steinrück, E. Cánovas, E. Brunner, D. Beljonne, M. Bonn, H. I. Wang, R. Dong, X. Feng, *Nat. Mater.* **2023**, *22*, 880.
[28] K. Geng, T. He, R. Liu, S. Dalapati, K. T. Tan, Z. Li, S. Tao, Y. Gong, Q. Jiang, D. Jiang, *Chem. Rev.* **2020**, *120*, 8814.

[29] G. Chakraborty, I.-H. Park, R. Medishetty, J. J. Vittal, *Chem. Rev.* **2021**, *121*, 3751.
[30] G. Galeotti, F. De Marchi, E. Hamzehpoor, O. MacLean, M. Rajeswara Rao, Y. Chen, L. V. Besteiro, D. Dettmann, L. Ferrari, F. Frezza, P. M. Sheverdyaeva, R. Liu, A. K. Kundu, P. Moras, M. Ebrahimi, M. C. Gallagher, F. Rosei, D. F. Perepichka, G. Contini, *Nat. Mater.* **2020**, *19*, 874.
[31] Y. Jing, T. Heine, *J. Am. Chem. Soc.* **2019**, *141*, 743.
[32] M. Souto, K. Strutyński, M. Melle-Franco, J. Rocha, *Chem. Eur. J.* **2020**, *26*, 10912.
[33] M. Sarkar, T. K. Dutta, A. Patra, *Chem Asian J* **2021**, *16*, 3055.
[34] C. Wang, Z. Zhang, Y. Zhu, C. Yang, J. Wu, W. Hu, *Adv. Mater.* **2022**, *34*, 2102290.
[35] A. M. Evans, M. J. Strauss, A. R. Corcos, Z. Hirani, W. Ji, L. S. Hamachi, X. Aguilar-Enriquez, A. D. Chavez, B. J. Smith, W. R. Dichtel, *Chem. Rev.* **2022**, *122*, 442.
[36] Y. Jin, Y. Hu, M. Ortiz, S. Huang, Y. Ge, W. Zhang, *Chem. Soc. Rev.* **2020**, *49*, 4637.
[37] R. Dong, T. Zhang, X. Feng, *Chem. Rev.* **2018**, *118*, 6189.
[38] H. Wang, Z. Zeng, P. Xu, L. Li, G. Zeng, R. Xiao, Z. Tang, D. Huang, L. Tang, C. Lai, D. Jiang, Y. Liu, H. Yi, L. Qin, S. Ye, X. Ren, W. Tang, *Chem. Soc. Rev.* **2019**, *48*, 488.
[39] J. Sakamoto, J. van Heijst, O. Lukin, A. D. Schlüter, *Angew. Chem. Int. Ed.* **2009**, *48*, 1030.
[40] R. Liu, K. T. Tan, Y. Gong, Y. Chen, Z. Li, S. Xie, T. He, Z. Lu, H. Yang, D. Jiang, *Chem. Soc. Rev.* **2021**, *50*, 120.
[41] S. Xu, M. Richter, X. Feng, *Acc. Mater. Res.* **2021**, *2*, 252.
[42] C. Qian, L. Feng, W. L. Teo, J. Liu, W. Zhou, D. Wang, Y. Zhao, *Nat Rev Chem* **2022**, *6*, 881.
[43] F. Yang, S. Cheng, X. Zhang, X. Ren, R. Li, H. Dong, W. Hu, *Adv. Mater.* **2018**, *30*, 1702415.
[44] Y. Yang, K. Börjesson, *Trends in Chemistry* **2022**, *4*, 60.
[45] D. Rodríguez-San-Miguel, C. Montoro, F. Zamora, *Chem. Soc. Rev.* **2020**, *49*, 2291.
[46] S. Wang, Q. Wang, P. Shao, Y. Han, X. Gao, L. Ma, S. Yuan, X. Ma, J. Zhou, X. Feng, B. Wang, *J. Am. Chem. Soc.* **2017**, *139*, 4258.
[47] S. Chandra, S. Kandambeth, B. P. Biswal, B. Lukose, S. M. Kunjir, M. Chaudhary, R. Babarao, T. Heine, R. Banerjee, *J. Am. Chem. Soc.* **2013**, *135*, 17853.
[48] L. Wang, C. Xu, W. Zhang, Q. Zhang, M. Zhao, C. Zeng, Q. Jiang, C. Gu, Y. Ma, *J. Am. Chem. Soc.* **2022**, *144*, 8961.
[49] H. Sahabudeen, H. Qi, B. A. Glatz, D. Tranca, R. Dong, Y. Hou, T. Zhang, C. Kuttner, T. Lehnert, G. Seifert, U. Kaiser, A. Fery, Z. Zheng, X. Feng, *Nat Commun* **2016**, *7*, 13461.
[50] K. Wang, H. Yang, Z. Liao, S. Li, M. Hambsch, G. Fu, S. C. B. Mannsfeld, Q. Sun, T. Zhang, *J. Am. Chem. Soc.* **2023**, *145*, 5203.
[51] A. Kumar Mahato, S. Bag, H. S. Sasmal, K. Dey, I. Giri, M. Linares-Moreau, C. Carbonell, P. Falcaro, E. B. Gowd, R. K. Vijayaraghavan, R. Banerjee, *J. Am. Chem. Soc.* **2021**, *143*, 20916.
[52] M. Wang, Y. Wang, J. Zhao, J. Zou, X. Liang, Z. Zhu, J. Zhu, H. Wang, Y. Wang, F. Pan, Z. Jiang, *Angew. Chem. Int. Ed.* **2023**, *62*, e202219084.
[53] N. A. Khan, R. Zhang, X. Wang, L. Cao, C. S. Azad, C. Fan, J. Yuan, M. Long, H. Wu, M. A. Olson, Z. Jiang, *Nat Commun* **2022**, *13*, 3169.
[54] T. Zhang, Y. Hou, V. Dzhagan, Z. Liao, G. Chai, M. Löffler, D. Olianas, A. Milani, S. Xu, M. Tommasini, D. R. T. Zahn, Z. Zheng, E. Zschech, R. Jordan, X. Feng, *Nat Commun* **2018**, *9*, 1140.
[55] Y. Yang, C. Schäfer, K. Börjesson, *Chem* **2022**, S2451929422002571.
[56] H. Yan, Z. Kou, S. Li, T. Zhang, *Small* **2023**, *19*, 2207972.

[57] S. Bag, H. S. Sasmal, S. P. Chaudhary, K. Dey, D. Blätte, R. Guntermann, Y. Zhang, M. Položij, A. Kuc, A. Shelke, R. K. Vijayaraghavan, T. G. Ajithkumar, S. Bhattacharyya, T. Heine, T. Bein, R. Banerjee, *J. Am. Chem. Soc.* **2023**, *145*, 1649.
[58] C. Huang, Y. Li, N. Wang, Y. Xue, Z. Zuo, H. Liu, Y. Li, *Chem. Rev.* **2018**, *118*, 7744.
[59] A. Braslau, M. Deutsch, P. S. Pershan, A. H. Weiss, J. Als-Nielsen, J. Bohr, *Phys. Rev. Lett.* **1985**, *54*, 114.
[60] J. T. Culp, J.-H. Park, D. Stratakis, M. W. Meisel, D. R. Talham, *J. Am. Chem. Soc.* **2002**, *124*, 10083.
[61] L. Liu, B. Geng, W. Ji, L. Wu, S. Lei, W. Hu, *Adv. Mater.* **2023**, *35*, 2208377.
[62] R. Dong, W. Liu, J. Hao, *Acc. Chem. Res.* **2012**, *45*, 504.
[63] R. Dong, J. Hao, *Chem. Rev.* **2010**, *110*, 4978.
[64] K. Liu, H. Qi, R. Dong, R. Shivhare, M. Addicoat, T. Zhang, H. Sahabudeen, T. Heine, S. Mannsfeld, U. Kaiser, Z. Zheng, X. Feng, *Nat. Chem.* **2019**, *11*, 994.
[65] L. Addadi, S. Raz, S. Weiner, *Adv. Mater.* **2003**, *15*, 959.
[66] M. J. Olszta, X. Cheng, S. S. Jee, R. Kumar, Y.-Y. Kim, M. J. Kaufman, E. P. Douglas, L. B. Gower, *Mater. Sci. Eng. R Rep.* **2007**, *58*, 77.
[67] P. Raffa, D. A. Z. Wever, F. Picchioni, A. A. Broekhuis, *Chem. Rev.* **2015**, *115*, 8504.
[68] Z. Ou, B. Liang, Z. Liang, F. Tan, X. Dong, L. Gong, P. Zhao, H. Wang, Y. Zou, Y. Xia, X. Chen, W. Liu, H. Qi, U. Kaiser, Z. Zheng, *J. Am. Chem. Soc.* **2022**, *144*, 3233.
[69] K. Dey, M. Pal, K. C. Rout, S. Kunjattu H, A. Das, R. Mukherjee, U. K. Kharul, R. Banerjee, *J. Am. Chem. Soc.* **2017**, *139*, 13083.
[70] H. S. Sasmal, A. Halder, S. Kunjattu H, K. Dey, A. Nadol, T. G. Ajithkumar, P. Ravindra Bedadur, R. Banerjee, *J. Am. Chem. Soc.* **2019**, *141*, 20371.
[71] A. Giri, G. Shreeraj, T. K. Dutta, A. Patra, *Angew. Chem. Int. Ed.* **2023**, *62*, e202219083.
[72] Y. Zhong, B. Cheng, C. Park, A. Ray, S. Brown, F. Mujid, J.-U. Lee, H. Zhou, J. Suh, K.-H. Lee, A. J. Mannix, K. Kang, S. J. Sibener, D. A. Muller, J. Park, *Science* **2019**, *366*, 1379.
[73] J. Yuan, X. You, N. A. Khan, R. Li, R. Zhang, J. Shen, L. Cao, M. Long, Y. Liu, Z. Xu, H. Wu, Z. Jiang, *Nat Commun* **2022**, *13*, 3826.
[74] R. Yang, S. Liu, Q. Sun, Q. Liao, K. Xi, B. Su, *J. Am. Chem. Soc.* **2022**, *144*, 11778.
[75] A. Kropf, *Nature* **1976**, *264*, 92.
[76] V. S. Padalkar, S. Seki, *Chem. Soc. Rev.* **2015**, *45*, 169.
[77] A. C. Sedgwick, L. Wu, H.-H. Han, S. D. Bull, X.-P. He, T. D. James, J. L. Sessler, B. Z. Tang, H. Tian, J. Yoon, *Chem. Soc. Rev.* **2018**, *47*, 8842.
[78] J. L. Segura, M. J. Mancheño, F. Zamora, *Chem. Soc. Rev.* **2016**, *45*, 5635.
[79] F. J. Claire, M. A. Solomos, J. Kim, G. Wang, M. A. Siegler, M. F. Crommie, T. J. Kempa, *Nat Commun* **2020**, *11*, 5524.
[80] K. B. Lausund, O. Nilsen, *Nat Commun* **2016**, *7*, 13578.
[81] I. Stassen, M. Styles, G. Grenci, H. V. Gorp, W. Vanderlinden, S. D. Feyter, P. Falcaro, D. D. Vos, P. Vereecken, R. Ameloot, *Nat. Mater.* **2016**, *15*, 304.
[82] N. A. Khan, R. Zhang, H. Wu, J. Shen, J. Yuan, C. Fan, L. Cao, M. A. Olson, Z. Jiang, *J. Am. Chem. Soc.* **2020**, *142*, 13450.
[83] M. Liu, Y. Liu, J. Dong, Y. Bai, W. Gao, S. Shang, X. Wang, J. Kuang, C. Du, Y. Zou, J. Chen, Y. Liu, *Nat Commun* **2022**, *13*, 1411.
[84] C. Yin, M. Liu, Z. Zhang, M. Wei, X. Shi, Y. Zhang, J. Wang, Y. Wang, *J. Am. Chem. Soc.* **2023**, *145*, 11431.
[85] L. Lafferentz, V. Eberhardt, C. Dri, C. Africh, G. Comelli, F. Esch, S. Hecht, L. Grill, *Nat. Chem.* **2012**, *4*, 215.
[86] A. M. Evans, A. Giri, V. K. Sangwan, S. Xun, M. Bartnof, C. G. Torres-Castanedo, H. B. Balch, M. S. Rahn, N. P. Bradshaw, E. Vitaku, D. W. Burke, H. Li, M. J. Bedzyk, F.

Wang, J.-L. Brédas, J. A. Malen, A. J. H. McGaughey, M. C. Hersam, W. R. Dichtel, P. E. Hopkins, *Nat. Mater.* **2021**, *20*, 1142.
[87] L. Grill, S. Hecht, *Nat Chem.* **2020**, *12*, 115.
[88] S.-W. Hla, L. Bartels, G. Meyer, K.-H. Rieder, *Phys. Rev. Lett.* **2000**, *85*, 2777.
[89] G. S. McCarty, P. S. Weiss, *J. Am. Chem. Soc.* **2004**, *126*, 16772.
[90] K. Koner, S. Das, S. Mohata, N. T. Duong, Y. Nishiyama, S. Kandambeth, S. Karak, C. M. Reddy, R. Banerjee, *J. Am. Chem. Soc.* **2022**, *144*, 16052.
[91] K. Dey, S. Bhunia, H. S. Sasmal, C. M. Reddy, R. Banerjee, *J. Am. Chem. Soc.* **2021**, *143*, 955.
[92] L. Ascherl, E. W. Evans, M. Hennemann, D. Di Nuzzo, A. G. Hufnagel, M. Beetz, R. H. Friend, T. Clark, T. Bein, F. Auras, *Nat Commun* **2018**, *9*, 3802.
[93] Z. Wang, Z. Zhang, H. Qi, A. Ortega-Guerrero, L. Wang, K. Xu, M. Wang, S. Park, F. Hennersdorf, A. Dianat, A. Croy, H. Komber, G. Cuniberti, J. J. Weigand, U. Kaiser, R. Dong, X. Feng, *Nat Synth* **2022**, *1*, 69.
[94] J. W. Colson, A. R. Woll, A. Mukherjee, M. P. Levendorf, E. L. Spitler, V. B. Shields, M. G. Spencer, J. Park, W. R. Dichtel, *Science* **2011**, *332*, 228.
[95] D. Dettmann, P. M. Sheverdyaeva, E. Hamzehpoor, S. Franchi, G. Galeotti, P. Moras, C. Ceccarelli, D. F. Perepichka, F. Rosei, G. Contini, *ACS Nano* **2024**, *18*, 849.
[96] R. Madueno, M. T. Räisänen, C. Silien, M. Buck, *Nature* **2008**, *454*, 618.
[97] J. A. Theobald, N. S. Oxtoby, M. A. Phillips, N. R. Champness, P. H. Beton, *Nature* **2003**, *424*, 1029.
[98] V. Müller, F. Shao, M. Baljozovic, M. Moradi, Y. Zhang, T. Jung, W. B. Thompson, B. T. King, R. Zenobi, A. D. Schlüter, *Angew. Chem. Int. Ed.* **2017**, *56*, 15262.
[99] D. J. Murray, D. D. Patterson, P. Payamyar, R. Bhola, W. Song, M. Lackinger, A. D. Schlüter, B. T. King, *J. Am. Chem. Soc.* **2015**, *137*, 3450.
[100] P. Payamyar, K. Kaja, C. Ruiz-Vargas, A. Stemmer, D. J. Murray, C. J. Johnson, B. T. King, F. Schiffmann, J. VandeVondele, A. Renn, S. Götzinger, P. Ceroni, A. Schütz, L.-T. Lee, Z. Zheng, J. Sakamoto, A. D. Schlüter, *Adv. Mater.* **2014**, *26*, 2052.
[101] M. Yu, R. Dong, X. Feng, *J. Am. Chem. Soc.* **2020**, *142*, 12903.
[102] M. Souto, D. F. Perepichka, *J. Mater. Chem. C* **2021**, *9*, 10668.
[103] L. Sun, M. G. Campbell, M. Dincă, *Angew. Chem. Int. Ed* **2016**, *55*, 3566.
[104] L. Lin, Q. Zhang, Y. Ni, L. Shang, X. Zhang, Z. Yan, Q. Zhao, J. Chen, *Chem* **2022**, *8*, 1822.
[105] J. Zhao, J. Ren, G. Zhang, Z. Zhao, S. Liu, W. Zhang, L. Chen, *Chem. Eur. J.* **2021**, *27*, 10781.
[106] P. Stallinga, *Advanced Materials* **2011**, *23*, 3356.
[107] A. M. Evans, K. A. Collins, S. Xun, T. G. Allen, S. Jhulki, I. Castano, H. L. Smith, M. J. Strauss, A. K. Oanta, L. Liu, L. Sun, O. G. Reid, G. Sini, D. Puggioni, J. M. Rondinelli, T. Rajh, N. C. Gianneschi, A. Kahn, D. E. Freedman, H. Li, S. Barlow, G. Rumbles, J.-L. Brédas, S. R. Marder, W. R. Dichtel, *Adv. Mater.* **2022**, *34*, 2101932.
[108] E. Jin, K. Geng, S. Fu, M. A. Addicoat, W. Zheng, S. Xie, J.-S. Hu, X. Hou, X. Wu, Q. Jiang, Q.-H. Xu, H. I. Wang, D. Jiang, *Angew. Chem. Int. Ed* **2022**, *61*, e202115020.
[109] G. Xing, W. Zheng, L. Gao, T. Zhang, X. Wu, S. Fu, X. Song, Z. Zhao, S. Osella, M. Martínez-Abadía, H. I. Wang, J. Cai, A. Mateo-Alonso, L. Chen, *J. Am. Chem. Soc.* **2022**, *144*, 5042.
[110] E. Jin, S. Fu, H. Hanayama, M. A. Addicoat, W. Wei, Q. Chen, R. Graf, K. Landfester, M. Bonn, K. A. I. Zhang, H. I. Wang, K. Müllen, A. Narita, *Angew. Chem. Int. Ed.* **2022**, *61*, e202114059.
[111] Y. Liu, S. Fu, D. L. Pastoetter, A. H. Khan, Y. Zhang, A. Dianat, S. Xu, Z. Liao, M. Richter, M. Yu, M. Položij, E. Brunner, G. Cuniberti, T. Heine, M. Bonn, H. I. Wang, X. Feng, *Angew. Chem. Int. Ed.* **2022**, *61*, e202209762.

[112] H. Sahabudeen, H. Qi, M. Ballabio, M. Položij, S. Olthof, R. Shivhare, Y. Jing, S. Park, K. Liu, T. Zhang, J. Ma, B. Rellinghaus, S. Mannsfeld, T. Heine, M. Bonn, E. Cánovas, Z. Zheng, U. Kaiser, R. Dong, X. Feng, *Angew. Chem. Int. Ed.* **2020**, *132*, 6084.
[113] S. Fu, E. Jin, H. Hanayama, W. Zheng, H. Zhang, L. Di Virgilio, M. A. Addicoat, M. Mezger, A. Narita, M. Bonn, K. Müllen, H. I. Wang, *J. Am. Chem. Soc.* **2022**, *144*, 7489.
[114] E. Jin, K. Geng, S. Fu, S. Yang, N. Kanlayakan, M. A. Addicoat, N. Kungwan, J. Geurs, H. Xu, M. Bonn, H. I. Wang, J. Smet, T. Kowalczyk, D. Jiang, *Chem* **2021**, *7*, 3309.
[115] M. Wang, M. Ballabio, M. Wang, H.-H. Lin, B. P. Biswal, X. Han, S. Paasch, E. Brunner, P. Liu, M. Chen, M. Bonn, T. Heine, S. Zhou, E. Cánovas, R. Dong, X. Feng, *J. Am. Chem. Soc.* **2019**, *141*, 16810.
[116] Y. Liu, H. Zhang, H. Yu, Z. Liao, S. Paasch, S. Xu, R. Zhao, E. Brunner, M. Bonn, H. I. Wang, T. Heine, M. Wang, Y. Mai, X. Feng, *Angew. Chem. Int. Ed* **2023**, *62*, e202305978.
[117] S. Wan, F. Gándara, A. Asano, H. Furukawa, A. Saeki, S. K. Dey, L. Liao, M. W. Ambrogio, Y. Y. Botros, X. Duan, S. Seki, J. F. Stoddart, O. M. Yaghi, *Chem. Mater.* **2011**, *23*, 4094.
[118] J. Guo, Y. Xu, S. Jin, L. Chen, T. Kaji, Y. Honsho, M. A. Addicoat, J. Kim, A. Saeki, H. Ihee, S. Seki, S. Irle, M. Hiramoto, J. Gao, D. Jiang, *Nat Commun* **2013**, *4*, 2736.
[119] X. Feng, L. Liu, Y. Honsho, A. Saeki, S. Seki, S. Irle, Y. Dong, A. Nagai, D. Jiang, *Angew. Chem. Int. Ed.* **2012**, *124*, 2672.
[120] X. Ding, J. Guo, X. Feng, Y. Honsho, J. Guo, S. Seki, P. Maitarad, A. Saeki, S. Nagase, D. Jiang, *Angew. Chem. Int. Ed* **2011**, *50*, 1289.
[121] S. Dalapati, M. Addicoat, S. Jin, T. Sakurai, J. Gao, H. Xu, S. Irle, S. Seki, D. Jiang, *Nat Commun* **2015**, *6*, 7786.
[122] S. Jin, T. Sakurai, T. Kowalczyk, S. Dalapati, F. Xu, H. Wei, X. Chen, J. Gao, S. Seki, S. Irle, D. Jiang, *Chem. Eur. J.* **2014**, *20*, 14608.
[123] X. Feng, L. Chen, Y. Honsho, O. Saengsawang, L. Liu, L. Wang, A. Saeki, S. Irle, S. Seki, Y. Dong, D. Jiang, *Adv. Mater.* **2012**, *24*, 3026.
[124] C. Li, Y. Wang, Y. Zou, X. Zhang, H. Dong, W. Hu, *Angew. Chem. Int. Ed.* **2020**, *132*, 9489.
[125] J. I. Feldblyum, C. H. McCreery, S. C. Andrews, T. Kurosawa, E. J. G. Santos, V. Duong, L. Fang, A. L. Ayzner, Z. Bao, *Chem. Commun.* **2015**, *51*, 13894.
[126] N. Tessler, Y. Preezant, N. Rappaport, Y. Roichman, *Adv. Mater.* **2009**, *21*, 2741.
[127] Q. Zhang, S. Dong, P. Shao, Y. Zhu, Z. Mu, D. Sheng, T. Zhang, X. Jiang, R. Shao, Z. Ren, J. Xie, X. Feng, B. Wang, *Science* **2022**, *378*, 181.
[128] H. Xu, S. Tao, D. Jiang, *Nat. Mater.* **2016**, *15*, 722.
[129] Z. Wang, Y. Yang, Z. Zhao, P. Zhang, Y. Zhang, J. Liu, S. Ma, P. Cheng, Y. Chen, Z. Zhang, *Nat Commun* **2021**, *12*, 1982.
[130] R. Sahoo, S. Mondal, S. C. Pal, D. Mukherjee, M. C. Das, *Adv. Energy Mater.* **2021**, *11*, 2102300.
[131] K. Lei, D. Wang, L. Ye, M. Kou, Y. Deng, Z. Ma, L. Wang, Y. Kong, *ChemSusChem* **2020**, *13*, 1725.
[132] E. Jin, M. Asada, Q. Xu, S. Dalapati, M. A. Addicoat, M. A. Brady, H. Xu, T. Nakamura, T. Heine, Q. Chen, D. Jiang, *Science* **2017**, *357*, 673.
[133] G. Fu, D. Yang, S. Xu, S. Li, Y. Zhao, H. Yang, D. Wu, P. S. Petkov, Z.-A. Lan, X. Wang, T. Zhang, *J. Am. Chem. Soc.* **2024**, *146*, 1318.
[134] W. K. Haug, E. M. Moscarello, E. R. Wolfson, P. L. McGrier, *Chem. Soc. Rev.* **2020**, *49*, 839.

[135] Y. Wang, W. Hao, H. Liu, R. Chen, Q. Pan, Z. Li, Y. Zhao, *Nat. Commun.* **2022**, *13*, 100.
[136] X. Zhuang, W. Zhao, F. Zhang, Y. Cao, F. Liu, S. Bi, X. Feng, *Polym. Chem.* **2016**, *7*, 4176.
[137] S. Li, R. Ma, S. Xu, T. Zheng, H. Wang, G. Fu, H. Yang, Y. Hou, Z. Liao, B. Wu, X. Feng, L.-Z. Wu, X.-B. Li, T. Zhang, *ACS Catal.* **2023**, *13*, 1089.
[138] S. Li, R. Ma, S. Xu, T. Zheng, G. Fu, Y. Wu, Z. Liao, Y. Kuang, Y. Hou, D. Wang, P. S. Petkov, K. Simeonova, X. Feng, L.-Z. Wu, X.-B. Li, T. Zhang, *J. Am. Chem. Soc.* **2022**, *144*, 13953.
[139] D. L. Pastoetter, S. Xu, M. Borrelli, M. Addicoat, B. P. Biswal, S. Paasch, A. Dianat, H. Thomas, R. Berger, S. Reineke, E. Brunner, G. Cuniberti, M. Richter, X. Feng, *Angew. Chem. Int. Ed.* **2020**, *59*, 23620.
[140] R. Zhou, Y. Huang, Z. Li, S. Kang, X. Wang, S. Liu, *Energy Stor. Mater.* **2021**, *40*, 124.
[141] Y. Yue, H. Li, H. Chen, N. Huang, *J. Am. Chem. Soc.* **2022**, *144*, 2873.
[142] J.-D. Yi, D.-H. Si, R. Xie, Q. Yin, M.-D. Zhang, Q. Wu, G.-L. Chai, Y.-B. Huang, R. Cao, *Angew. Chem. Int. Ed.* **2021**, *60*, 17108.
[143] Y. Yue, P. Cai, X. Xu, H. Li, H. Chen, H.-C. Zhou, N. Huang, *Angew. Chem. Int. Ed.* **2021**, *60*, 10806.
[144] A. Mahmood, J.-Y. Hu, B. Xiao, A. Tang, X. Wang, E. Zhou, *J. Mater. Chem. A* **2018**, *6*, 16769.
[145] M. Urbani, G. de la Torre, M. K. Nazeeruddin, T. Torres, *Chem. Soc. Rev.* **2019**, *48*, 2738.
[146] Y. Matano, *Chem. Rev.* **2017**, *117*, 3138.
[147] Z. Meng, R. M. Stolz, K. A. Mirica, *J. Am. Chem. Soc.* **2019**, *141*, 11929.
[148] X. Ding, X. Feng, A. Saeki, S. Seki, A. Nagai, D. Jiang, *Chem. Commun.* **2012**, *48*, 8952.
[149] S. Thomas, H. Li, J.-L. Bredas, *Adv. Mater.* **2019**, *31*, 1900355.
[150] V. Lakshmi, C.-H. Liu, M. Rajeswara Rao, Y. Chen, Y. Fang, A. Dadvand, E. Hamzehpoor, Y. Sakai-Otsuka, R. S. Stein, D. F. Perepichka, *J. Am. Chem. Soc.* **2020**, *142*, 2155.
[151] D. W. Burke, R. R. Dasari, V. K. Sangwan, A. K. Oanta, Z. Hirani, C. E. Pelkowski, Y. Tang, R. Li, D. C. Ralph, M. C. Hersam, S. Barlow, S. R. Marder, W. R. Dichtel, *J. Am. Chem. Soc.* **2023**, *145*, 11969.
[152] H. Ding, Y. Li, H. Hu, Y. Sun, J. Wang, C. Wang, C. Wang, G. Zhang, B. Wang, W. Xu, D. Zhang, *Chem. Eur. J.* **2014**, *20*, 14614.
[153] S.-L. Cai, Y.-B. Zhang, A. B. Pun, B. He, J. Yang, F. M. Toma, I. D. Sharp, O. M. Yaghi, J. Fan, S.-R. Zheng, W.-G. Zhang, Y. Liu, *Chem. Sci.* **2014**, *5*, 4693.
[154] A. Mähringer, A. C. Jakowetz, J. M. Rotter, B. J. Bohn, J. K. Stolarczyk, J. Feldmann, T. Bein, D. D. Medina, *ACS Nano* **2019**, *13*, 6711.
[155] J.-H. Dou, M. Q. Arguilla, Y. Luo, J. Li, W. Zhang, L. Sun, J. L. Mancuso, L. Yang, T. Chen, L. R. Parent, G. Skorupskii, N. J. Libretto, C. Sun, M. C. Yang, P. V. Dip, E. J. Brignole, J. T. Miller, J. Kong, C. H. Hendon, J. Sun, M. Dincă, *Nat. Mater.* **2021**, *20*, 222.
[156] S. Wei, F. Zhang, W. Zhang, P. Qiang, K. Yu, X. Fu, D. Wu, S. Bi, F. Zhang, *J. Am. Chem. Soc.* **2019**, *141*, 14272.
[157] X. Ding, L. Chen, Y. Honsho, X. Feng, O. Saengsawang, J. Guo, A. Saeki, S. Seki, S. Irle, S. Nagase, V. Parasuk, D. Jiang, *J. Am. Chem. Soc.* **2011**, *133*, 14510.
[158] C. Qin, X. Wu, L. Tang, X. Chen, M. Li, Y. Mou, B. Su, S. Wang, C. Feng, J. Liu, X. Yuan, Y. Zhao, H. Wang, *Nat Commun* **2023**, *14*, 5238.

[159] Y. Qian, Y. Han, X. Zhang, G. Yang, G. Zhang, H.-L. Jiang, *Nat. Commun.* **2023**, *14*, 3083.
[160] Z. Li, T. Deng, S. Ma, Z. Zhang, G. Wu, J. Wang, Q. Li, H. Xia, S.-W. Yang, X. Liu, *J. Am. Chem. Soc.* **2023**, *145*, 8364.
[161] S. Jin, X. Ding, X. Feng, M. Supur, K. Furukawa, S. Takahashi, M. Addicoat, M. E. El-Khouly, T. Nakamura, S. Irle, S. Fukuzumi, A. Nagai, D. Jiang, *Angew. Chem. Int. Ed.* **2013**, *125*, 2071.
[162] S. Xu, H. Sun, M. Addicoat, B. P. Biswal, F. He, S. Park, S. Paasch, T. Zhang, W. Sheng, E. Brunner, Y. Hou, M. Richter, X. Feng, *Adv. Mater.* **2021**, *33*, 2006274.
[163] L. Chen, K. Furukawa, J. Gao, A. Nagai, T. Nakamura, Y. Dong, D. Jiang, *J. Am. Chem. Soc.* **2014**, *136*, 9806.
[164] A. M. Rice, E. A. Dolgopolova, B. J. Yarbrough, G. A. Leith, C. R. Martin, K. S. Stephenson, R. A. Heugh, A. J. Brandt, D. A. Chen, S. G. Karakalos, M. D. Smith, K. B. Hatzell, P. J. Pellechia, S. Garashchuk, N. B. Shustova, *Angew. Chem. Int. Ed.* **2018**, *57*, 11310.
[165] G. A. Leith, A. M. Rice, B. J. Yarbrough, A. A. Berseneva, R. T. Ly, C. N. Buck III, D. Chusov, A. J. Brandt, D. A. Chen, B. W. Lamm, M. Stefik, K. S. Stephenson, M. D. Smith, A. K. Vannucci, P. J. Pellechia, S. Garashchuk, N. B. Shustova, *Angew. Chem. Int. Ed.* **2020**, *59*, 6000.
[166] M. Dogru, M. Handloser, F. Auras, T. Kunz, D. Medina, A. Hartschuh, P. Knochel, T. Bein, *Angew. Chem. Int. Ed.* **2013**, *52*, 2920.
[167] Z. Zhao, M. E. El-Khouly, Q. Che, F. Sun, B. Zhang, H. He, Y. Chen, *Angew. Chem. Int. Ed.* **2023**, *62*, e202217249.
[168] B. Feng, X. Chen, P. Yan, S. Huang, C. Lu, H. Ji, J. Zhu, Z. Yang, K. Cao, X. Zhuang, *J. Am. Chem. Soc.* **2023**, *145*, 26871.
[169] Y. Zhao, S. Li, G. Fu, H. Yang, S. Li, D. Wu, T. Zhang, *ACS Cent. Sci.* **2024**, DOI 10.1021/acscentsci.3c01195.
[170] K. Liu, J. Li, H. Qi, M. Hambsch, J. Rawle, A. R. Vázquez, A. S. Nia, A. Pashkin, H. Schneider, M. Polozij, T. Heine, M. Helm, S. C. B. Mannsfeld, U. Kaiser, R. Dong, X. Feng, *Angew. Chem. Int. Ed.* **2021**, *60*, 13859.
[171] C. Wang, L. Cusin, C. Ma, E. Unsal, H. Wang, V. G. Consolaro, V. Montes-García, B. Han, S. Vitale, A. Dianat, A. Croy, H. Zhang, R. Gutierrez, G. Cuniberti, Z. Liu, L. Chi, A. Ciesielski, P. Samorì, *Adv. Mater.* **2024**, *36*, 2305882.
[172] A. Das, S. Ghosh, *Angew. Chem. Int. Ed.* **2014**, *53*, 2038.
[173] B. Dereka, A. Rosspeintner, M. Krzeszewski, D. T. Gryko, E. Vauthey, *Angew. Chem. Int. Ed.* **2016**, *55*, 15624.
[174] A. C. Jakowetz, M. L. Böhm, J. Zhang, A. Sadhanala, S. Huettner, A. A. Bakulin, A. Rao, R. H. Friend, *J. Am. Chem. Soc.* **2016**, *138*, 11672.
[175] H. Tan, W. Xu, Y. Sheng, C. S. Lau, Y. Fan, Q. Chen, M. Tweedie, X. Wang, Y. Zhou, J. H. Warner, *Adv. Mater.* **2017**, *29*, 1702917.
[176] H. Li, P. Shao, S. Chen, G. Li, X. Feng, X. Chen, H.-J. Zhang, J. Lin, Y.-B. Jiang, *J. Am. Chem. Soc.* **2020**, *142*, 3712.
[177] M. A. Springer, T.-J. Liu, A. Kuc, T. Heine, *Chem. Soc. Rev.* **2020**, *49*, 2007.
[178] Y. Jing, T. Heine, *Nat. Mater.* **2020**, *19*, 823.
[179] K. S. Novoselov, A. K. Geim, S. V. Morozov, D. Jiang, M. I. Katsnelson, I. V. Grigorieva, S. V. Dubonos, A. A. Firsov, *Nature* **2005**, *438*, 197.
[180] A. Zhao, S.-Q. Shen, *Phys. Rev. B* **2012**, *85*, 085209.
[181] N. B. Kopnin, T. T. Heikkilä, G. E. Volovik, *Phys. Rev. B* **2011**, *83*, 220503.
[182] A. Julku, S. Peotta, T. I. Vanhala, D.-H. Kim, P. Törmä, *Phys. Rev. Lett.* **2016**, *117*, 045303.

[183] J. M. Rotter, R. Guntermann, M. Auth, A. Mähringer, A. Sperlich, V. Dyakonov, D. D. Medina, T. Bein, *Chem. Sci.* **2020**, *11*, 12843.
[184] M. Wang, M. Wang, H.-H. Lin, M. Ballabio, H. Zhong, M. Bonn, S. Zhou, T. Heine, E. Cánovas, R. Dong, X. Feng, *J. Am. Chem. Soc.* **2020**, *142*, 21622.
[185] Q. Zhang, M. Dai, H. Shao, Z. Tian, Y. Lin, L. Chen, X. C. Zeng, *ACS Appl. Mater. Interfaces* **2018**, *10*, 43595.
[186] Y. Zhu, P. Shao, L. Hu, C. Sun, J. Li, X. Feng, B. Wang, *J. Am. Chem. Soc.* **2021**, *143*, 7897.
[187] S. Cai, B. Sun, X. Li, Y. Yan, A. Navarro, A. Garzón-Ruiz, H. Mao, R. Chatterjee, J. Yano, C. Zhu, J. A. Reimer, S. Zheng, J. Fan, W. Zhang, Y. Liu, *ACS Appl. Mater. Interfaces* **2020**, *12*, 19054.
[188] L. Wang, C. Zeng, H. Xu, P. Yin, D. Chen, J. Deng, M. Li, N. Zheng, C. Gu, Y. Ma, *Chem. Sci.* **2019**, *10*, 1023.
[189] M. Chhowalla, H. S. Shin, G. Eda, L.-J. Li, K. P. Loh, H. Zhang, *Nat. Chem.* **2013**, *5*, 263.
[190] A. Prasoon, H. Yang, M. Hambsch, N. N. Nguyen, S. Chung, A. Müller, Z. Wang, T. Lan, P. Fontaine, T. D. Kühne, K. Cho, A. S. Nia, S. C. B. Mannsfeld, R. Dong, X. Feng, *Commun Chem* **2023**, *6*, 1.
[191] S. Ghosh, Y. Tsutsui, T. Kawaguchi, W. Matsuda, S. Nagano, K. Suzuki, H. Kaji, S. Seki, *Chem. Mater.* **2022**, *34*, 736.
[192] B. Sun, C.-H. Zhu, Y. Liu, C. Wang, L.-J. Wan, D. Wang, *Chem. Mater.* **2017**, *29*, 4367.
[193] C. R. DeBlase, K. Hernández-Burgos, K. E. Silberstein, G. G. Rodríguez-Calero, R. P. Bisbey, H. D. Abruña, W. R. Dichtel, *ACS Nano* **2015**, *9*, 3178.
[194] J. Song, H. Liu, Z. Zhao, P. Lin, F. Yan, *Adv. Mater.* **2023**, *n/a*, 2300034.
[195] C. Dai, Y. Liu, D. Wei, *Chem. Rev.* **2022**, *122*, 10319.
[196] S. Das, A. Sebastian, E. Pop, C. J. McClellan, A. D. Franklin, T. Grasser, T. Knobloch, Y. Illarionov, A. V. Penumatcha, J. Appenzeller, Z. Chen, W. Zhu, I. Asselberghs, L.-J. Li, U. E. Avci, N. Bhat, T. D. Anthopoulos, R. Singh, *Nat Electron* **2021**, *4*, 786.
[197] Q. Wang, Z. Ai, Q. Guo, X. Wang, C. Dai, H. Wang, J. Sun, Y. Tang, D. Jiang, X. Pei, R. Chen, J. Gou, L. Yu, J. Ding, A. T. S. Wee, Y. Liu, D. Wei, *J. Am. Chem. Soc.* **2023**, *145*, 10035.
[198] M. E. Belowich, J. F. Stoddart, *Chem. Soc. Rev.* **2012**, *41*, 2003.
[199] A. Zhang, C. M. Lieber, *Chem. Rev.* **2016**, *116*, 215.
[200] X. Xu, B. J. Bowen, R. E. A. Gwyther, M. Freeley, B. Grigorenko, A. V. Nemukhin, J. Eklöf-Österberg, K. Moth-Poulsen, D. D. Jones, M. Palma, *Angew. Chem. Int. Ed.* **2021**, *60*, 20184.
[201] J. Chen, H. Pu, M. C. Hersam, P. Westerhoff, *Adv. Mater.* **2022**, *34*, 2106975.
[202] S. Jin, M. Supur, M. Addicoat, K. Furukawa, L. Chen, T. Nakamura, S. Fukuzumi, S. Irle, D. Jiang, *J. Am. Chem. Soc.* **2015**, *137*, 7817.
[203] Y.-J. Yu, Y. Zhao, S. Ryu, L. E. Brus, K. S. Kim, P. Kim, *Nano Lett.* **2009**, *9*, 3430.
[204] M. G. Lemaitre, E. P. Donoghue, M. A. McCarthy, B. Liu, S. Tongay, B. Gila, P. Kumar, R. K. Singh, B. R. Appleton, A. G. Rinzler, *ACS Nano* **2012**, *6*, 9095.
[205] C.-J. Shih, R. Pfattner, Y.-C. Chiu, N. Liu, T. Lei, D. Kong, Y. Kim, H.-H. Chou, W.-G. Bae, Z. Bao, *Nano Lett.* **2015**, *15*, 7587.
[206] J. Rivnay, S. Inal, A. Salleo, R. M. Owens, M. Berggren, G. G. Malliaras, *Nat Rev Mater* **2018**, *3*, 1.
[207] D. Khodagholy, J. Rivnay, M. Sessolo, M. Gurfinkel, P. Leleux, L. H. Jimison, E. Stavrinidou, T. Herve, S. Sanaur, R. M. Owens, G. G. Malliaras, *Nat Commun* **2013**, *4*, 2133.

[208] J. Rivnay, P. Leleux, M. Sessolo, D. Khodagholy, T. Hervé, M. Fiocchi, G. G. Malliaras, *Adv. Mater.* **2013**, *25*, 7010.
[209] R. B. Rashid, A. M. Evans, L. A. Hall, R. R. Dasari, E. K. Roesner, S. R. Marder, D. M. D'Allesandro, W. R. Dichtel, J. Rivnay, *Adv. Mater.* **2022**, *34*, 2110703.
[210] M. K. Hota, S. Chandra, Y. Lei, X. Xu, M. N. Hedhili, A.-H. Emwas, O. Shekhah, M. Eddaoudi, H. N. Alshareef, *Adv. Funct. Mater.* **2022**, *32*, 2201120.
[211] J. Song, H. Liu, Z. Zhao, X. Guo, C. Liu, S. Griggs, A. Marks, Y. Zhu, H. K. Law, I. McCulloch, F. Yan, *Sci. Adv.* **2023**, *9*, eadd9627.
[212] L. Chua, *IEEE Trans Circuits Syst* **1971**, *18*, 507.
[213] Y. Chen, G. Liu, C. Wang, W. Zhang, R.-W. Li, L. Wang, *Mater. Horizons* **2014**, *1*, 489.
[214] Y. Chen, B. Zhang, G. Liu, X. Zhuang, E.-T. Kang, *Chem. Soc. Rev.* **2012**, *41*, 4688.
[215] K. Zhou, Z. Jia, Y. Zhou, G. Ding, X.-Q. Ma, W. Niu, S.-T. Han, J. Zhao, Y. Zhou, *J. Phys. Chem. Lett.* **2023**, *14*, 7173.
[216] B. Sun, X. Li, T. Feng, S. Cai, T. Chen, C. Zhu, J. Zhang, D. Wang, Y. Liu, *ACS Appl. Mater. Interfaces* **2020**, *12*, 51837.
[217] C. Li, D. Li, W. Zhang, H. Li, G. Yu, *Angew. Chem. Int. Ed.* **2021**, *60*, 27135.
[218] H. Xin, B. Hou, X. Gao, *Acc. Chem. Res.* **2021**, *54*, 1737.
[219] F. Schwarz, M. Koch, G. Kastlunger, H. Berke, R. Stadler, K. Venkatesan, E. Lörtscher, *Angew. Chem. Int. Ed.* **2016**, *55*, 11781.
[220] J. Huang, S. Huang, Y. Zhao, B. Feng, K. Jiang, S. Sun, C. Ke, E. Kymakis, X. Zhuang, *Small Methods* **2020**, *4*, 2000628.
[221] R. J. Mortimer, *Chem. Soc. Rev.* **1997**, *26*, 147.
[222] P. M. Beaujuge, J. R. Reynolds, *Chem. Rev.* **2010**, *110*, 268.
[223] B.-B. Cui, Y.-W. Zhong, J. Yao, *J. Am. Chem. Soc.* **2015**, *137*, 4058.
[224] P. Remón, M. Bälter, S. Li, J. Andréasson, U. Pischel, *J. Am. Chem. Soc.* **2011**, *133*, 20742.
[225] B. Błasiak, C. H. Londergan, L. J. Webb, M. Cho, *Acc. Chem. Res.* **2017**, *50*, 968.
[226] R. J. Mortimer, *Electrochim. Acta.* **1999**, *44*, 2971.
[227] R.-T. Wen, C. G. Granqvist, G. A. Niklasson, *Nat. Mater.* **2015**, *14*, 996.
[228] S. Cong, F. Geng, Z. Zhao, *Adv. Mater.* **2016**, *28*, 10518.
[229] Q. Hao, Z.-J. Li, C. Lu, B. Sun, Y.-W. Zhong, L.-J. Wan, D. Wang, *J. Am. Chem. Soc.* **2019**, *141*, 19831.
[230] F. Yu, W. Liu, S.-W. Ke, M. Kurmoo, J.-L. Zuo, Q. Zhang, *Nat Commun* **2020**, *11*, 5534.
[231] Q. Hao, Z.-J. Li, B. Bai, X. Zhang, Y.-W. Zhong, L.-J. Wan, D. Wang, *Angew. Chem. Int. Ed.* **2021**, *60*, 12498.
[232] P. M. Beaujuge, C. M. Amb, J. R. Reynolds, *Acc. Chem. Res.* **2010**, *43*, 1396.
[233] P. M. Beaujuge, S. Ellinger, J. R. Reynolds, *Nat. Mater.* **2008**, *7*, 795.
[234] D. Bessinger, K. Muggli, M. Beetz, F. Auras, T. Bein, *J. Am. Chem. Soc.* **2021**, *143*, 7351.
[235] Z. Wang, X. Jia, P. Zhang, Y. Liu, H. Qi, P. Zhang, U. Kaiser, S. Reineke, R. Dong, X. Feng, *Adv. Mater.* **2022**, *34*, 2106073.
[236] W.-T. Koo, J.-S. Jang, I.-D. Kim, *Chem* **2019**, *5*, 1938.
[237] Z. Meng, K. A. Mirica, *Chem. Soc. Rev.* **2021**, *50*, 13498.
[238] K. Xu, N. Huang, *Chem. Res. Chin. Univ.* **2022**, *38*, 339.
[239] X. Chen, L. Kong, J. A.-A. Mehrez, C. Fan, W. Quan, Y. Zhang, M. Zeng, J. Yang, N. Hu, Y. Su, H. Wei, Z. Yang, *Nano-Micro Lett.* **2023**, *15*, 149.
[240] A. Mei, W. Chen, Z. Yang, M. Zhou, W. Jin, S. Yang, K. Chen, Y. Liu, *Angew. Chem. Int. Ed.* **2023**, *62*, e202301440.

[241] M. Liu, Y.-J. Chen, X. Huang, L.-Z. Dong, M. Lu, C. Guo, D. Yuan, Y. Chen, G. Xu, S.-L. Li, Y.-Q. Lan, *Angew. Chem. Int. Ed.* **2022**, *61*, e202115308.
[242] L. Lu, C. Jiang, G. Hu, J. Liu, B. Yang, *Adv. Mater.* **2021**, *33*, 2100218.
[243] H. Tai, S. Wang, Z. Duan, Y. Jiang, *Sens. Actuators B Chem.* **2020**, *318*, 128104.
[244] S. Jhulki, A. M. Evans, X.-L. Hao, M. W. Cooper, C. H. Feriante, J. Leisen, H. Li, D. Lam, M. C. Hersam, S. Barlow, J.-L. Brédas, W. R. Dichtel, S. R. Marder, *J. Am. Chem. Soc.* **2020**, *142*, 783.
[245] G. Gao, J.-W. Shi, Z. Fan, C. Gao, C. Niu, *Chem. Eng. J.* **2017**, *325*, 91.
[246] F. H. L. Koppens, T. Mueller, P. Avouris, A. C. Ferrari, M. S. Vitiello, M. Polini, *Nat. Nanotechnol.* **2014**, *9*, 780.
[247] W. Wang, W. Zhao, H. Xu, S. Liu, W. Huang, Q. Zhao, *Coord Chem Rev* **2021**, *429*, 213616.
[248] J. Han, F. Wang, S. Han, W. Deng, X. Du, H. Yu, J. Gou, Q. J. Wang, J. Wang, *Adv. Funct. Mater.* **2022**, *32*, 2205150.
[249] Y. Xiong, Q. Liao, Z. Huang, X. Huang, C. Ke, H. Zhu, C. Dong, H. Wang, K. Xi, P. Zhan, F. Xu, Y. Lu, *Adv. Mater.* **2020**, *32*, 1907242.
[250] M. Calik, F. Auras, L. M. Salonen, K. Bader, I. Grill, M. Handloser, D. D. Medina, M. Dogru, F. Löbermann, D. Trauner, A. Hartschuh, T. Bein, *J. Am. Chem. Soc.* **2014**, *136*, 17802.
[251] D. Bessinger, L. Ascherl, F. Auras, T. Bein, *J. Am. Chem. Soc.* **2017**, *139*, 12035.
[252] T. He, K. Geng, D. Jiang, *Trends in Chemistry* **2021**, *3*, 431.
[253] D. Fan, W. Li, H. Qiu, Y. Xu, S. Gao, L. Liu, T. Li, F. Huang, Y. Mao, W. Zhou, W. Meng, M. Liu, X. Tu, P. Wang, Z. Yu, Y. Shi, X. Wang, *Nat Electron* **2023**, 1.

Biographies

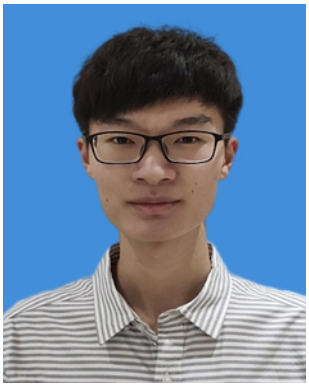

Guang-en Fu received his B.S. degree from the Shandong University of Science and Technology in 2020 and then received his M.S. degree from the Ningbo Institute of Materials Technology and Engineering, Chinese Academy of Sciences, in 2023. His research interests mainly focus on the controllable synthesis of two-dimensional polymer thin films toward organic electronic devices.

Haoyong Yang received his B.S. degree in materials from Xiangtan University in 2019. After graduation, he moved to Ningbo Institute of Materials Technology and Engineering, Chinese Academy of Sciences, to pursue his Ph.D. His current work focuses on the interfacial synthesis of two dimensions polymers and their promising applications in organic electronic.

Wenkai Zhao received his B.S. degree in Polymer Materials and Engineering from Henan University of Technology in 2022. He is currently a M.S. candidate under the supervision of Prof. Tao Zhang at Ningbo Institute of Materials Technology, Chinese Academy of Sciences. His research work mainly focuses on the synthesis and application of sp^2-carbon-conjugated covalent organic frameworks.

Paolo Samorì received his PhD degree in Chemistry from the Humboldt University of Berlin (Prof. J. P. Rabe). Currently, he is a distinguished professor at the University of Strasbourg and

emeritus director of the Institut de Science et d'Ingénierie Supramoléculaires. His research interests comprise nanochemistry, supramolecular sciences, materials chemistry with a specific focus on graphene and other 2D materials, as well as functional organic/polymeric and hybrid nanomaterials for applications in optoelectronics, energy, and sensing.

Tao Zhang received his B.S. degree in chemistry from Sichuan University in 2008, and his Ph.D. degree from Dresden University of Technology in 2015. Currently, he is a professor at the Ningbo Institute of Materials Technology and Engineering, Chinese Academy of Science, and the head of the research group of interface functional polymer materials. His research is focused on the design and synthesis of two-dimensional conjugated polymers as well as their applications in organic electronic devices.